2014

The DapE-Encoded N-Succinyl-L,L-Diaminopimelic Acid Desuccinylase (DapE) from Haemophilus Influenzae as a Prospective Target for the Development of Novel Antibiotics

Anna Starus
Loyola University Chicago

LOYOLA UNIVERSITY CHICAGO

THE DAPE-ENCODED N-SUCCINYL-L,L-DIAMINOPIMELIC ACID DESUCCINYLASE (DAPE) FROM *HAEMOPHILUS INFLUENZAE* AS A PROSPECTIVE TARGET FOR THE DEVELOPMENT OF NOVEL ANTIBIOTICS

A DISSERTATION SUBMITTED TO

THE FACULTY OF THE GRADUATE SCHOOL

IN CANDIDACY FOR THE DEGREE OF

DOCTOR OF PHILOSOPHY

PROGRAM IN CHEMISTRY

BY

ANNA STARUS

CHICAGO, IL

DECEMBER 2014

ACKNOWLEDGMENTS

I would like to acknowledge all the people who made the completion of this dissertation possible. First and foremost, I would like to thank my graduate advisor, Dr. Richard C. Holz, for the opportunity to work with him. You are a wonderful mentor who has offered me a great support, guidance, and encouragement.

I would also like to thank the members of my dissertation committee Dr. Ken Olsen, Dr. Daniel Becker and Dr. Dali Liu for all their guidance, fruitful discussions and ideas for the project. Other faculty members who have assisted me greatly at Loyola University Chicago include Dr. Miguel Ballicora who have provided me with his vast knowledge and helped with data analysis.

I would like to give special thanks to Dr. Danuta Gillner who thought me a lot of what I know, always supported me and served as a great friend. I would also like to thank my collaborators at the Argonne National Laboratory Dr. Boguslaw P. Nocek and Dr. Robert Jedrzejczak for the opportunity to work and learn from them as well as their friendship. I would also like to thank Dr. Bennett, Dr. Larrabee, Dr. Scott and Dr. Ye whom I have formed great collaboration which resulted in great publications. I am also grateful for the support and friendship of Salette Martinez and Natalie Gumataotao.

I would also like to thank Loyola University Chicago for providing the funds which allowed me to complete my research. Arthur J. Schmidt Dissertation Fellowship

for the 2012-2013 school years allowed me to solely focus on final experiments and the writing process.

I would like to thank my fiancé for his infinite support during the challenging times. Finally, I would like to express my thanks to my father, brother and most importantly my mother, without whom I would not be the person that I am today. Her wisdom and strength is my inspiration.

To my mother for all her love, encouragement and continuous support.

TABLE OF CONTENTS

LIST OF TABLES

LIST OF FIGURES

LIST OF ABBREVIATIONS

2xYT	2 x yeast extract tryptone
Å	Angstrom
α	Alpha helices
β	Beta sheets
Δ	Difference
°C	Degree Celsius
DMSO	Dimethyl sulfoxide
equiv.	Equivalent
ε	Extinction coeffiecient
Abs	Absorbance
AAP	Aminopeptidase from Aeromonas proteolytica
CPG2	Carbocypeptidase G2 from Pseudomonas sp. Strain RS-16
J	Coupling constant
Co2+	Cobalt ion
eV	Electron volt
EDTA	Ethylenediaminetetraacetic acid
fs	Femtosecond
G	Gauss
Hz	Hertz
GHz	Gigahertz

h	Hours
K	Kelvin
kDa	Kilodaltons
L	Liter
LB	Luria-Bertani
B	Magnetic field
mW	Megawatt
Ni-NTA	Nickel-nitrilotriacetic acid
PPi	Phosphate buffer
PEG	Polyethylene glycol
KOH	Potassium hydroxide
M	Transition dipole moments
UV – Vis	Ultraviolet visible spectrophotometry
PDB `	Protein data bank
g	Relative centrifugal force
I/σ	Resolution, signal-to-noise ratio
s	Seconds
NaCl	Sodium chloride
NaOH	Sodium hydroxide
T	Tesla
TEV	Tobacco Etch Virus
TCEP	Tri(2-carboxyethyl)phosphine
T	Truncated
v/v	Volume per volume

λmax	Wavelength of maximum absorbance
w/v	Weight per volume
WT	Wild-type
D	Zero-field splitting parameter
Zn^{2+}	Zinc ion
ZBG	Zinc-binding group
HEPES	2-[4-(2-hydroxyethyl)piperazin-1-yl]ethanesulfonic acid
BIS-TRIS	2-[Bis(2-hydroxyethyl)amino]-2-(hydroxymethyl)propane-1,3-diol

ABSTRACT

The rapid emergence of bacteria that are resistant to today's antibiotics makes them more and more ineffective. Consequently, the need for a novel class of antibacterial agents is rapidly increasing. The importance of this project is emphasized by the emergence of several pathogenic bacterial strains that are resistant to all currently available antibiotics on the market today. One way to approach this problem is to develop drugs that target essential bacterial biosynthetic pathways. Based on bacterial genetic information, the meso-diaminopimelate (mDAP)/lysine biosynthetic pathway offers several potential anti-bacterial targets that have not been yet explored. One of these, the *dapE*-encoded N-succinyl-L,L-diaminopimelic acid desuccinylase (DapE) catalyzes the hydrolysis of N-succinyl-L,L-diaminopimelate to L,L-diaminopimelate and succinate. Since there are no similar pathways in mammals, inhibitors that target one or more of the enzymes in the mDAP/lysine biosynthetic pathway will likely exhibit selective toxicity against only bacteria.

It has been shown experimentally that deletion of the gene encoding for DapE is lethal to *Helicobacter pylori* and *Mycobacterium smegmatis*. Therefore, DapEs are crucial for bacterial cell growth and proliferation, making them potential targets for a new class of antibiotics. Rational design of inhibitors for DapE relies on understanding the active site structure and catalytic mechanism. Therefore, the DapE enzymes from *Haemophilus influenzae* and *Neisseria meningitidis* were characterized biochemically and

crystallographically. In addition, residues situated within the active site were mutated and the mutated enzymes were characterized *via* kinetic and crystallographic methods in order to gain insight into substrate binding. In order to examine the role of the catalytic domain of DapE truncated enzymes from *Vibrio cholera* and *H. influenzae* were engineered by deleting their dimerization domains. And finally, a reliable and reproducible spectrophotometric assay for DapE enzymes that is conducive to high-throughput screening was developed.

CHAPTER ONE

INTRODUCTION

Infectious diseases continue to be a serious threat to public health around the world. Most importantly, the rapid emergence of resistant bacteria makes today's antibiotic's more and more ineffective, consequently increasing the need for a novel class of antibacterial agents.[1] The Center for Disease Control and Prevention (CDC) recently reported the emergence of several strains of *Staphylococcus aureus* that are resistant to even the most powerful antibiotics of last resort, such as vancomycin. These data emphasize the fact that no drug can prevent a simple staph infection from becoming deadly.[2] Just 12 years ago, vancomycin failed only ~0.3% of the time in treating infections caused by *Enterococcus faecalis*, however this number increased 26-fold in just four years.[3] Various other strains of common bacterial species capable of causing fatal illnesses (*E. faecalis*, *Mycobacterium tuberculosis*, *Escherichia coli* O157:H7, and *Pseudomonas aeruginosa*) are already resistant to all existing drugs including vancomycin and even to the newest antibiotic linezolid, which was first used in 1990.[4,5] A summary of the commonly used antibiotics, their modes of action, and resistance mechanisms is shown in Table 1.[6]

In the past, *Streptococcus pneumoniae* had been susceptible to penicillin, however a new drug-resistant strain (DRSP) has recently emerged that is no longer vulnerable to penicillin-type antibiotics.[4] Recurrently, this type of resistance originates in clinical

Table 1. Antibiotics in clinical use and modes of resistance.

Antibiotic class	Example(s)	Target	Mode(s) of resistance
β-Lactams	Penicillins (ampicillin), cephalosporins (cephamycin), penems (meropenem), monobactams (aztreonam)	Peptidoglycan biosynthesis	Hydrolysis, efflux, altered target
Aminoglycosides	Gentamicin, streptomycin, spectinomycin	Translation	Phosphorylation, acetylation, nucleotidylation, efflux, altered target
Glycopeptides	Vancomycin, teicoplanin	Peptidoglycan biosynthesis	Reprogramming peptidoglycan biosynthesis
Tetracyclines	Minocycline, tigecycline	Translation	Monooxygenation, efflux, altered target
Macrolides	Erythromycin, azithromicin	Translation	Hydrolysis, glycosylation, phosphorylation, efflux, altered target
Lincosamides	Clindamycin	Translation	Nucleotidylation, efflux, altered target
Streptogramins	Synercid	Translation	C-O lyase (type B streptogramins), acetylation (type A streptogramins),
Oxazolidinones	Linezolid	Translation	Efflux, altered target
Phenicols	Chloramphenicol	Translation	Acetylation, efflux, altered target
Quinolones	Ciprofloxacin	DNA replication	Acetylation, efflux, altered target
Pyrimidines	Trimethoprim	C1 metabolism	Efflux, altered target
Sulfonamides	Sulfamethoxazole	C1 metabolism	Efflux, altered target
Rifamycins	Rifampin	Transcription	ADP-ribosylation, efflux, altered target
Lipopeptides	Daptomycin	Cell membrane	Altered target
Cationic peptides	Colistin	Cell membrane	Altered target, efflux

environments where pathogenic and commensal bacteria are challenged with high concentrations of antibiotics.[7] Historically it has been shown that within hospital settings, resistanat pathogens often emerge within a few years after a new antibiotic is introduced (Figure 1).[6] Pathogens that currently cause the majority of hospital infections

Figure 1. Antibiotic resistance evolution showing the rapid development of resistance for several classes of antibiotics. The bars mark the time from the introduction of an antibiotic to the clinic until the first clinical case of resistance to that antibiotic was reported.[8, 9, 10, 11]

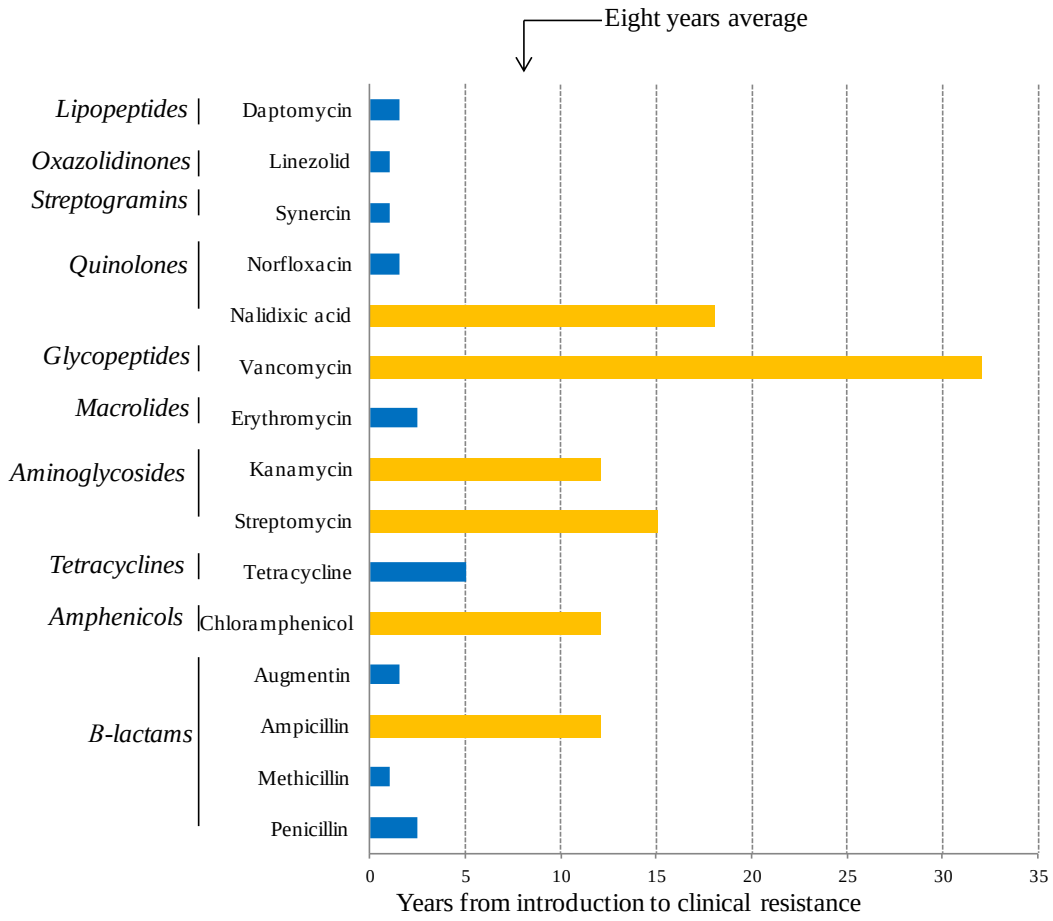

and urgently require new drug candidates are: ***E****nterococcus faecium*, ***S****taphylococcus aureus*, ***K****lebsiella pneumonia*, ***A****cinetobacter baumanii*, ***P****seudomonas aeruginosa*, and ***E****nterobacter* species ("ESKAPE" pathogens).[12] Recently, Gram-negative

Enterobacteriaceae, a bacterium that is resistant to carbapanem due to the New Delhi metallo-β-lactamase-1 (NDM-1), made headlines as a major global health problem. In a recent paper published by Kumarasami *et al*.,[13] fourtyfour isolates were identified with NDM-1 in India, Pakistan, and the UK. NDM-1 was mostly found among *Escherichia coli* and *Klabsiella pneumonia*, which were highly resistant to all antibiotics except tigecycline and colistin.[13]

The newest report from the CDC indicates that the number of estimated annual illnesses and deaths caused by antibiotic resistance are 2,049,442 and 23,000, respectively. The CDC has ranked antibiotic-resistant organisms based on seven criteria: health impact, economic impact, rate of infection, ten-year projected rate of infection, ease of spread, antibiotic availability, and prevention barriers. Number one in the CDC's most urgent category is *Clostridium difficile*, which causes 250,000 hospitalizations, at least 14,000 deaths and $1 billion in healthcare costs each year. The other two organisms are carbapenem-resistant *Enterobacteriaceae* (CRE) and drug-resistant *Neisseria gonorrhoeae*. In March 2013, the CDC called CRE a "nightmare bacteria" being even more dangerous than methicillin-resistant *Staphylococcus aureus* (MRSA). Among all of the bacterial resistance problems, gram-negative pathogens such as *Enterobacteriaceae*, *Pseudomonas aeruginosa*, and *Acinetobacter* are particularly dangerous due to becoming resistant to nearly all antibiotics.[14]

Unfortunately, this pattern of resistance will persist as bacteria continue to develop ways to survive. Resistance to antibiotics can be caused by four general mechanisms: (a) inactivation or modification of the antibiotic; (b) alteration in the target site of the antibiotic that reduces its binding capacity; (c) modification of metabolic

pathways to circumvent the antibiotic effect; and (d) reduced intracellular antibiotic accumulation by decreasing permeability and/or increasing active efflux of the antibiotic.[15] Bacteria can develop resistance to antibiotics by mutating existing genes (point mutations, deletions, inversions, insertions, etc.) or by acquiring new genes from other strains or species (horizontal gene transfer).[16]

Despite the critical need for new antibiotics to treat drug-resistant infections the number of new antibiotics approved by the Food and Drug Administration (FDA) has declined 75 % over the last 24 years with only five new antibiotics approved in the last few years and only three novel classes of antibiotics introduced within the last 40 years (Figure 2).[17] In a way, the antibiotic industry has been a victim of its own success. After penicillin and other major antibiotics were discovered it was believed that the battle with infectious diseases was conquered. Life expectancy increased and the number of deaths caused by infectious diseases fell tremendously. Consequently, both grant funding and research programs lead by pharmaceutical giants declined significantly.[18] Many major pharmaceutical and biotech companies left the antibiotic research field. For example, since 1999, 10 of the 15 largest companies have significantly reduced or eliminated their antibiotic research programs.[19] One major reason why pharmaceutical companies are not pursuing antibacterial research is simply due to low profit margins. Antibiotics are short course therapies as opposed to billion dollar blockbuster drugs that typically treat chronic diseases, such as high cholesterol. Moreover, the increased restrictions on the use of antibiotics and more stringent regulatory requirements make antibiotic research even less attractive.[20] In addition, natural compounds such as penicillin have been very successful

throughout the years and have provided the basic structures from which scientists have made many analogues. Although this rout has been successful and potent compounds

Figure 2. Number of approved antibiotics between 1935 and 2007.

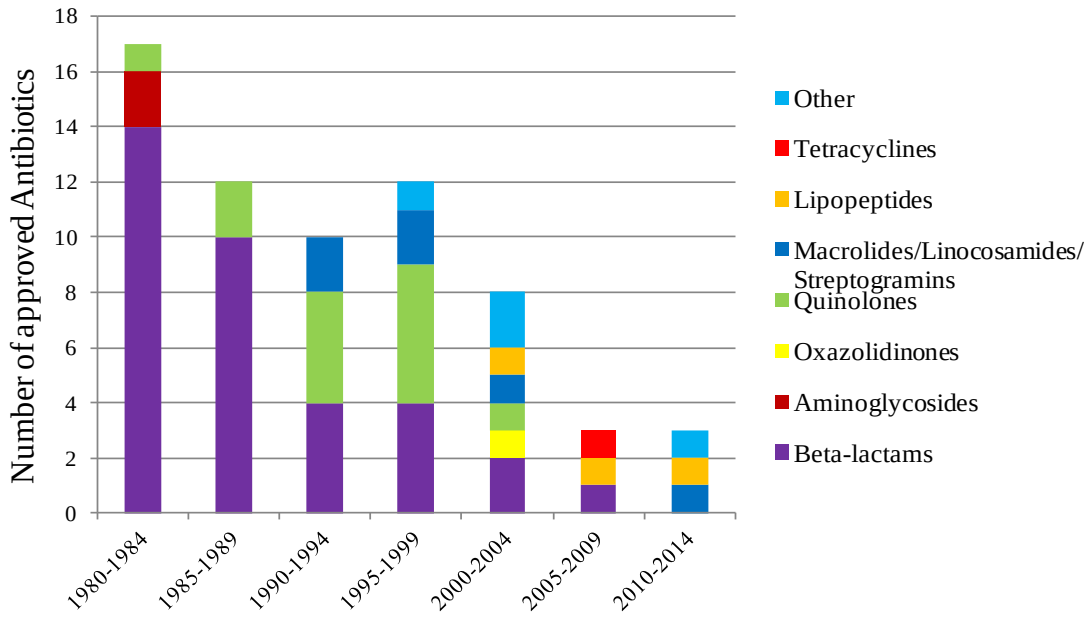

such as amoxicillin have been discovered, no new classes of antibiotics have been discovered and the number of modifications that can be introduced to a compound is limited.[20]

Fortunately, congress together with other organizations finally recognized the urgent need to encourage new antibiotic development. Policymakers are now offering pharmaceutical companies patent extensions and tax breaks, in order to revive the interest in antibiotic research. In November 2010, the Infectious Diseases Society of America (IDSA) addressed the threat of antimicrobial resistance by insisting U.S. and European Union leaders join forces in developing new antibiotics. To accomplish this goal, IDSA

launched a new collaboration titled "10 x `20" initiative. The goal of this collaboration is to create a joint venture that will develop 10 novel antibiotics by 2020.[21] Governments together with other nongovernmental organizations have made significant efforts to increase the interest in antibiotic research. In the US, the federal Interagency Task Force on Antimicrobial Resistance updated its "Public Health Action Plan to Combat Antimicrobial Resistance" document in 2011.[22] On June 12, 2012 Europe's largest public-private partnership between the European Commission and European Federation of Pharmaceutical Industries and Associations (EFPIA) held a seminar devoted to the clinical development aspects "Combating Antimicrobial Resistance – New Drugs 4 Bad Bugs" (ND4BB). The Innovative Medicines Initiative was set up in 2008 to support collaborative research between industrial and academic experts to reduce drug discovery bottlenecks and boost pharmaceutical innovation within Europe.[23] On June 26, 2012, the U.S. Senate passed the FDA Safety and Innovation Act (FDASIA) which reauthorizes the Prescription Drug User Fee Act (PDUFA) for the fifth time. The bill was mainly designed to speed up reviews of novel drugs for infectious diseases as well as improve communication between manufacturers and the FDA to prevent drug shortages. The "Generating Antibiotic Incentives Now" act, which is a part of the PDUFA, was designed to provide pharmaceutical and biotechnology companies with incentives to develop new antibiotics for the treatment of life-threatening infectious diseases caused by drug resistant pathogens. These pathogens primarily consists of resistant gram positive pathogens, including methicillin-resistant *Staphylococcus aureus* (MRSA), vancomycin resistant *Staphylococcus* and *enterococcus*, multi-drug resistant gram negative bacteria, including *Acinetobacter, Klebsiella, Pseudomonas* and *E. coli* species, multi-drug

resistant tuberculosis, and *Clostridium difficile*.[24] Moreover, it is extremely optimistic to see both public and private organizations encouraging research and development by combination of various incentives.

The area of genomics has influenced the discovery of novel antimicrobial agents tremendously. It provided the ability to sequence entire bacterial genomes and identify essential genes that upon deletion result in inhibition of cell growth. The main principle lies in the fact that targets should not be shared with a human host and only be present in the bacteria that are responsible for the disease. Libraries of compounds can now be screened to find molecules that inhibit the enzymatic function of the target. Those molecules can further be screened for antibacterial activity such as the ability to successfully penetrate the cell membrane.[25] As a result of these advances in genomics, the meso-diaminopimelate (mDAP)/lysine biosynthetic pathway was validated as a viable source of several potential antibacterial enzyme targets that have yet to be explored (Figure 3).[26] The initial steps in the pathway involve the four step conversion of aspartic acid to L-tetrahydrodipicolinate. This compound can either be directly converted to meso-DAP by the dehydrogenase pathway, acetylase pathway or the succinylase pathway. Ultimately, all of these pathways lead to meso-DAP formation. However, the succinylase pathway is the primary biosynthetic pathway in most Gram-negative and Gram-positive bacteria for the synthesis of meso-DAP.[27] The dehydrogenase pathway is a high energy transformation and is limited to only few *Bacillus* species.[27] The acetylase pathway is also limited to only few *Bacillus* species.[28]

Figure 3. Biosynthetic pathways of *meso*-diaminopimelic acid and lysine in bacteria.

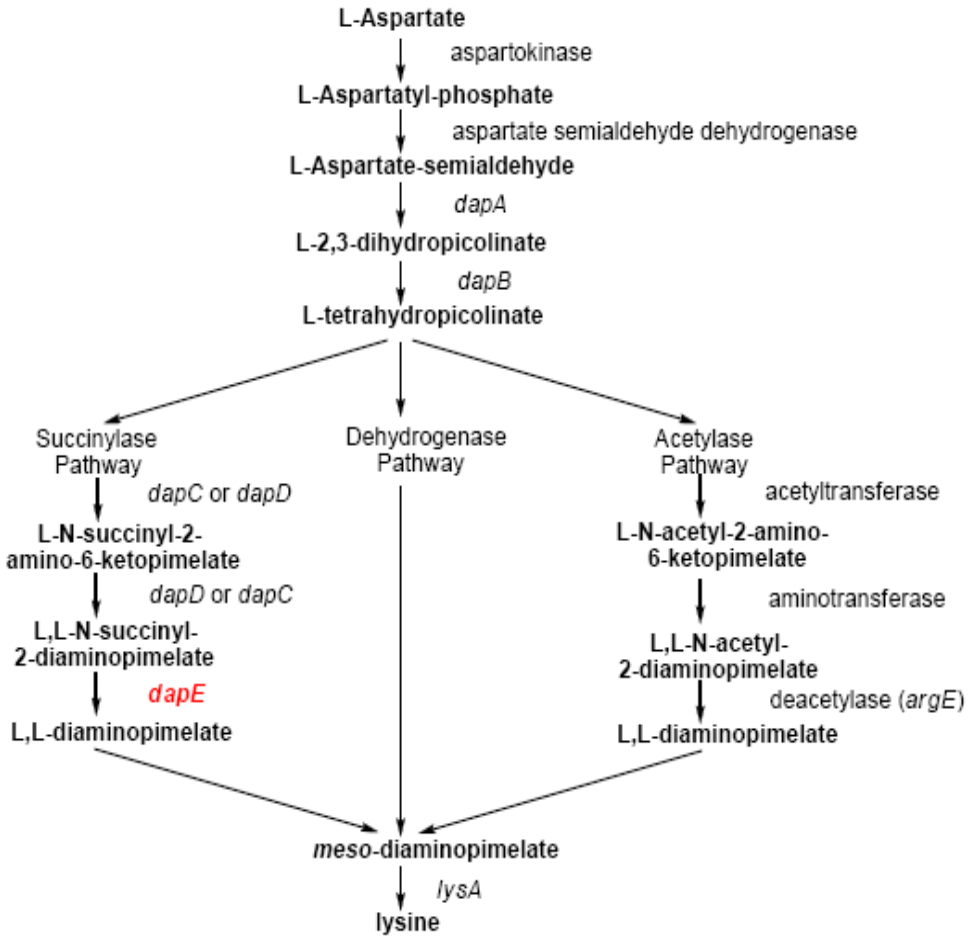

The dapE-encoded N-succinyl-L,L diaminopimelic acid desuccinylase (DapE) is a member of this meso-diaminopim elate (meso-DAP)/lysine biosynthetic pathway.[27, 20, 23] Lysine, which is one of the products of the pathway, is an essential component in the production of the peptidoglycan layer of Gram-positive bacterial cell walls.[20] A second product and an immediate precursor of lysine is the amino acid mDAP, which is used in the peptidoglycan cell wall of Gram-negative bacteria, providing a link between polysaccharide strands.[29,2] Since there are no similar pathways in mammals, inhibitors of DapE are hypothesized to provide selective toxicity against bacteria and show little or no

toxicity towards humans. It has been shown experimentally that deletion of the gene encoding for DapE is lethal to *Helicobacter pylori* and *Mycobacterium smegmatis*. Even in lysine-supplemented medium *H. pylori* was unable to grow. Therefore, DapEs are crucial for bacterial cell growth and proliferation.[30, 31]

DapEs catalyze the hydrolysis of *N*-succinyl-L,L-diaminopimelic acid (SDAP), forming L,L-diaminopimelic acid and succinate (Figure 4).[29] DapE is an ideal enzyme to

Figure 4. Reaction catalyzed by DapE.

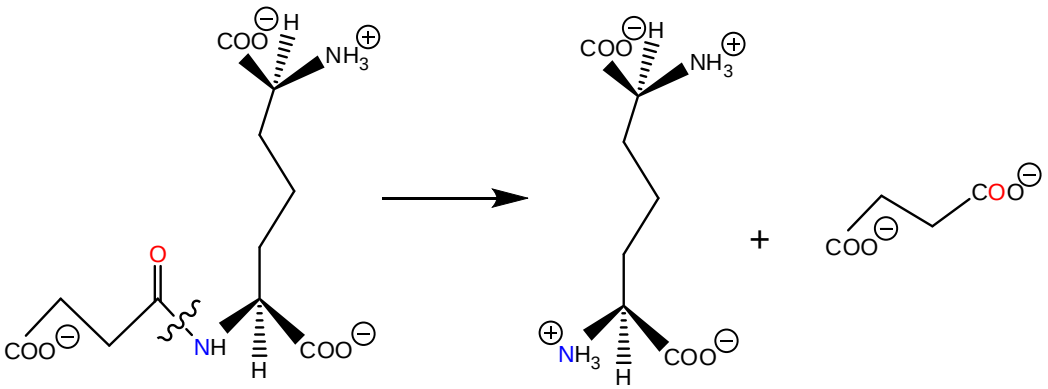

N-succinyl-L,L-diaminopimelic acid (SDAP) **L,L-diaminopimelic acid** **Succinic acid**

study in the mDAP/lysine biosynthetic pathway because it is highly soluble, readily available in large amounts, and is capable of being genetically manipulated. Biochemical studies revealed that the DapEs from *E. coli* and *H. influenzae* are small (approximately 42 kDa) dimeric enzymes that require two Zn(II) ions per mole of polypeptide for full enzymatic activity.[32] As-purified, DapE contains only one tightly bound Zn(II) ion and exhibits approximately 80% of its total activity. DapE can be substituted with Co(II) providing an enzyme that is twice as active as the native Zn(II) enzyme.[33] It has also

been shown by Broder and Miller that DapE can act as a Mn^{2+}-activated Asp-specific dipeptidase, by investigating the promiscuity of DapE upon substitution of the active site zinc ions with different metals. Their study indicated that the metal content of DapE's active site regulates its role as an aspartate peptidase, which catalytically cleaves the amide bonds of small dipeptide molecules with the general formula of Asp-X, particularly Asp-Ser, Asp-Gly, Asp-Lue and Asp-Cys with exception of Asp-Pro. This is possible due to the fact that the second metal binding site has a lower affinity for metal ions as compared to the first metal biding site. Therefore, the authors propose that the form of DapE that is active as a peptidase contains Zn^{2+} in the tight binding site and Mn^{2+} in the low-affinity site.[34] Homology studies show that alignment of the gene sequences of DapE with the aminopeptidase from *Aeromonas proteolytica* (AAP) and the carboxypeptidase from *Pseudomonas* sp strains-RS-16 (CPG_2) indicate that all of the amino acids that function as metal ligands are highly conserved.[29,35]

Crystal Structure of DapE

One major limitation in understanding the catalytic mechanism and the design and synthesis of inhibitors was the lack of an X-ray crystal structure of DapE enzyme. The only crystal structure of DapE published until 2010 was an apo form of DapE from *N. meningitidis*.[36] Even though the crystal structure contributed key structural data, the lack of active site metal ions made it difficult to determine the spatial arrangement of catalytically relevant residues that reside within the active site. This hurdle was overcome when Nocek, Gilner *et al*.[37] reported the X-ray crystal structure of both the mono- and dinuclear zinc DapE enzymes from *H. influenzae* and *N. menigtididis*. The

architecture of the active site and the core of the catalytic domain of DapEs could now be analyzed in more detail to gain insight on substrate binding and mechanism.

The X-ray crystal structures of the mono and dinuclear Zn(II)-forms of the DapE from *H. influenzae* were solved at 2.0 and 2.3 Å resolution, respectively. These structures closely resemble the DapE structure from *N. meningitidis* and as previously published the enzyme is organized as a dimer with each monomer divided into two domains: a larger catalytic domain, which forms a 3-layer (αβα) sandwich and a smaller ferrodoxin-like domain that forms the dimer interface (Figure 5). The core of the catalytic domain, which houses the active site supplies ligands for the zinc ions and consists of an eight-stranded twisted β-sheets that are sandwiched between seven α-helices. The domains are connected via a small hinge region that allows movements of the dimerization domain in reference to the catalytic domain. The shape of the DapE homodimer resembles twisted rotary style telephone receiver with the catalytic domain located on the outside edge and separated by ~47 Å. The active site cleft is located in the center of the catalytic domain and is constituted by residues from five loops. [37]

Obtaining the monozinc form of the DapE enzyme allowed confirmation of previously published kinetic and spectroscopic results, which showed that DapE maintains activity with only one metal ion in the active site. It also allowed confirmation of the assignment of the first metal binding site. In the active site of [Zn_(DapE)], Zn1 resides in a distorted tetrahedral geometry coordinated by the carboxylate oxygens of D100 and of E163 as well as one nitrogen atom of H67 (Figure 6). The second coordination site is filled by an oxygen atom provided from a water molecule.

Figure 5. Ribbon drawing of dinuclear DapE from *H. influenzae.*

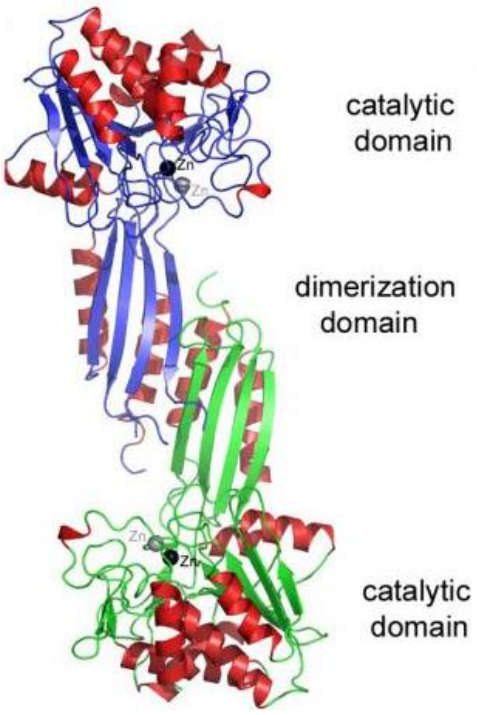

In [ZnZn(DapE)], the active site contains two Zn(II) ions at a distance of 3.36 Å apart (Figure 7). Each of the Zn(II) ions adopt a distorted tetrahedral geometry and are coordinated by one imidazole group (H67 for Zn1 and H349 for Zn2) and one carboxylate group (E163 for Zn1 and E135 for Zn2). Both Zn(II) ions are bridged by an additional carboxylate groups of D100 on one side and water/hydroxide on the opposite side, forming a (μ-aquo)(μ-carboxylato)dizinc(II) core with one terminal carboxylate and one histidine residue at each metal site. These structures confirm previous data suggesting that H67 and H349 are active site ligands.[32, 38] The structure also confirmed that the position of glutamate E134 indicates its important role in the catalysis, functioning as a general acid/base, previously reported by Davis *et al*.[38]

Figure 6. Active site of [Zn_(DapE)] from *H. influenzae.*

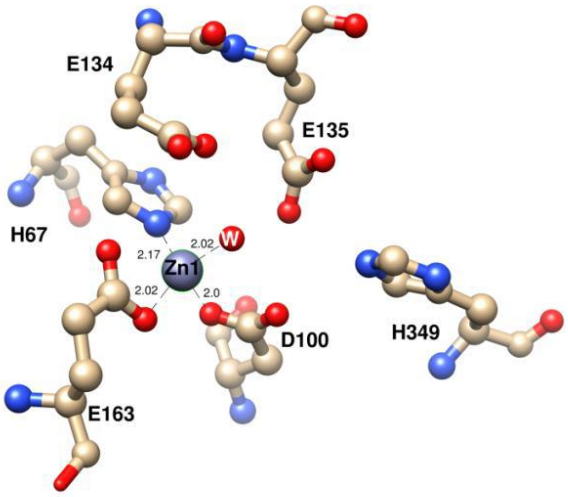

Figure 7. Active site of [ZnZn(DapE)] from *H. influenzae*.

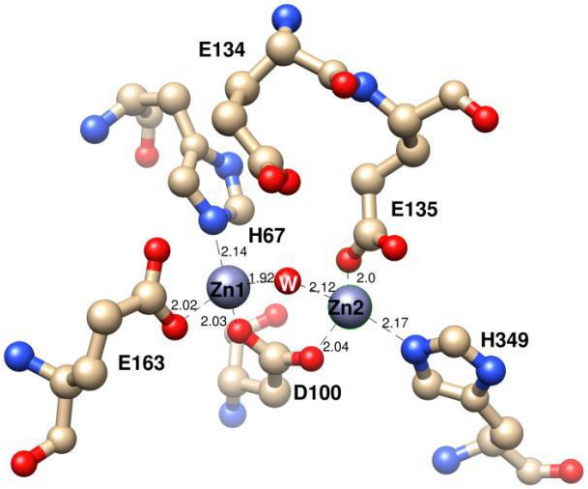

Analysis of the molecular surface of DapE together with its X-ray crystal structures, revealed a negatively charged cavity that extends along the catalytic domain. (Figure 8). It is postulated that the substrate binds in an extended conformation, lining

Figure 8. Surface rendering of [ZnZn(DapE)] showing the charge distribution and depicting the smile-shaped active site cavity. Blue: positive charge; Red: negative charge.

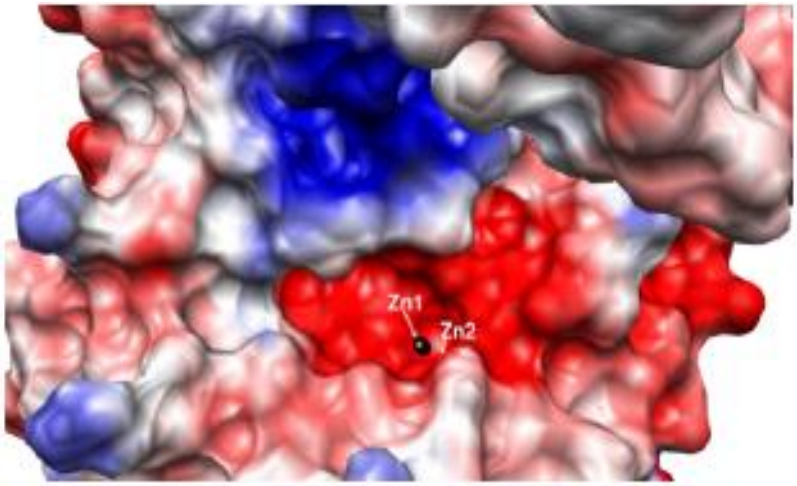

up along the grove with the peptide bond positioned over the active site metals. Substrate binding is further stabilized by interactions between substrate carboxylic groups with positively charged amino acid side chains. The potential positive charged residues that could possibly play this role are K175, K178, and N345 at one end and R258, R329, and K139 at the opposite end (Figure 9). The side chain of K135 is ~6 Å away from the center of the active site, which allows for an interaction of amino group of lysine with the carboxylate group of substrate and thus, be involved in recognition and stabilization of substrate at the active site. On the opposite side, the carboxyl group of L,L- SDAP could be stabilized by an interaction with R258 and R329. T325, which is centrally positioned

Figure 9. Side chains potentially involved in binding and substrate stabilization.

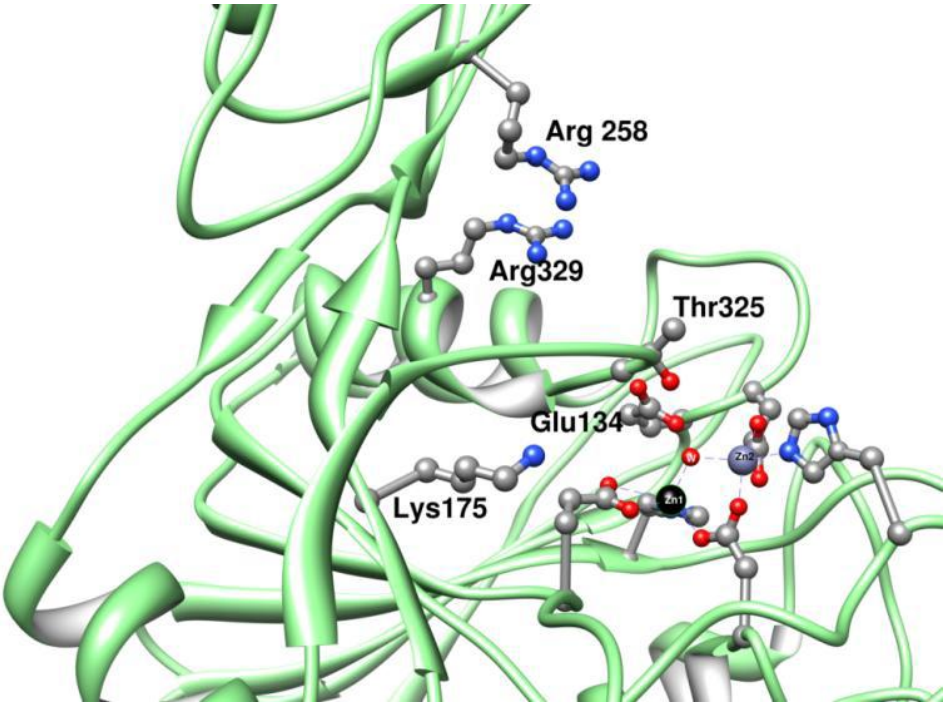

on a loop overhanging the active site, is also in hydrogen bond distance (3.11 Å) of the carboxyl group of the L,L- SDAP moiety.

The architecture of the active site and the core of the catalytic domain of *Hi*DapE are strikingly similar to AAP and CPG2, even though they catalyze markedly different hydrolytic reactions.[39,40] These structures provide an important starting point for mechanistic studies as well as the design of novel inhibitors for DapE enzymes.

Proposed Mechanism of DapE

Based on the X-ray crystal structure, previously reported kinetic and spectroscopic studies of DapE and the recently published mechanisms of AAP[41, 41b] a refined catalytic mechanism for DapE was proposed (Figure 10).[37] After recognition of the L,L-SDAP the peptide carbonyl oxygen of L,L-SDAP coordinates to Zn1, expanding

its coordination number from four to five and activating towards nucleophilic attack. Once the zinc-bound hydroxide is formed, it can attack the activated carbonyl carbon of the substrate, forming an η-1-μ-transition-state complex.[33] E134 provides a proton to the penultimate amino nitrogen of SDAP, which facilitates product release. Once the products are released, a water molecule bridging the two metal ions is replaced. In the absence of a second metal ion, H349 is in position to assist in orienting the substrate properly in the active site through the formation of a hydrogen bond with a carboxylate side chain of the substrate, thereby stabilizing the transition-state intermediate. In the presence of a dinuclear site the second metal ion likely coordinates either the peptide carbonyl oxygen in a bridging fashion or a carboxylate side chain of the substrate.

Figure 10. Proposed mechanism of DapE (a) monozinc DapE and (b) dizinc DapE.

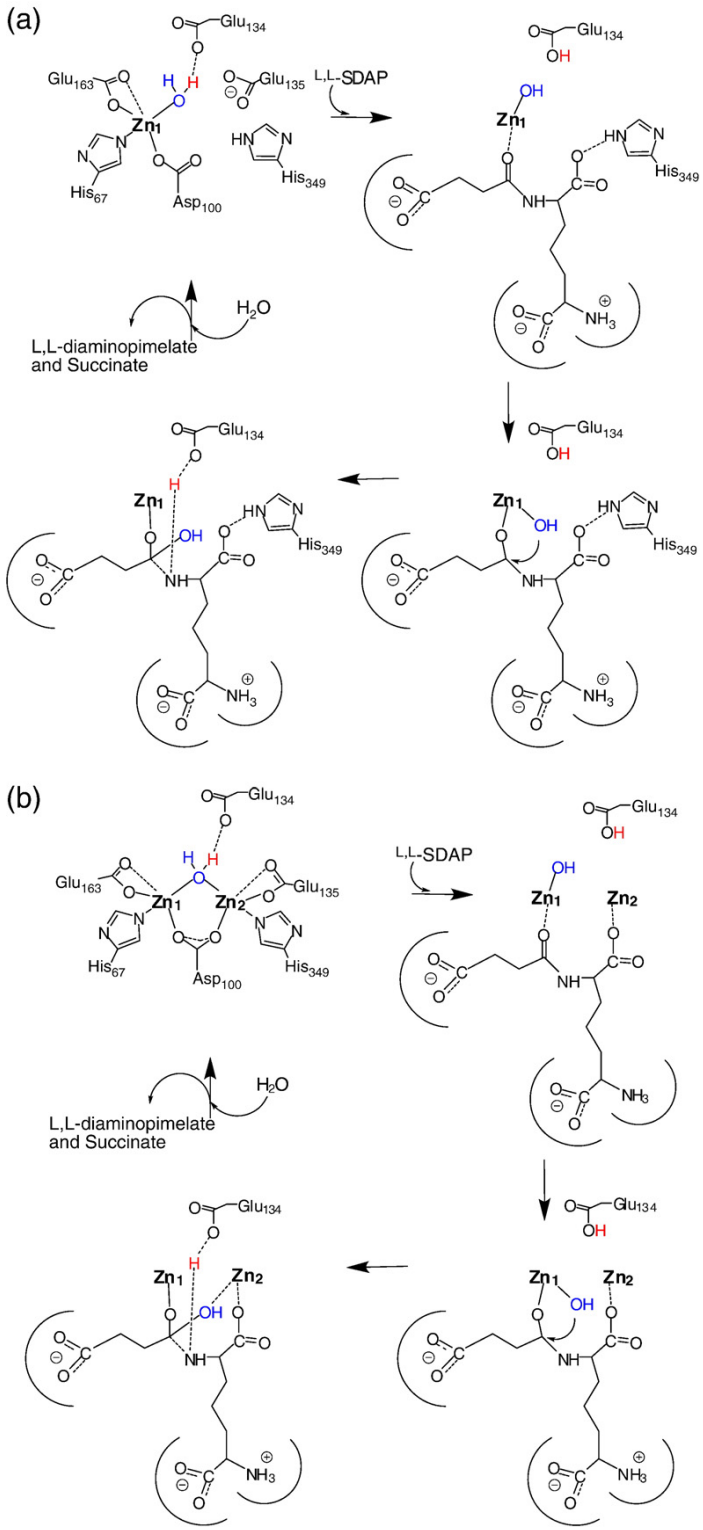

Potential Inhibitors of DapE

Several compounds containing zinc-binding groups (ZBG's) including thiols, carboxylic acids, boronic acids, phosphonates and hydroxamates have been screened delivering a number of micromolar inhibitors of DapE from *H. influenzae.* Thus far, the most potent inhibitors include L-captopril (IC_{50} = 3.3 μM, K_i = 1.8 μM), L-penicillamine (IC_{50} = 13.7 μM , K_i = 4.6 μM), 2-thiopheneboronic acid (TPhB) (IC_{50} = 92 μM, K_i = 67 μM) and phenyl boronic acid (PhB) (IC_{50} = 107 μM, K_i = 56.9 μM).[42] Particularly interesting is the fact that DapE is stereoselective with respect to recognition of inhibitors. D-penicillamine and D-captopril are weaker inhibitors than the corresponding L-isoform. Since crystallization attempts for DapE from *H. influenzae* in the presence of L-captopril, L-penicillamine, 2-thiopheneboronic acid or phenyl boronic acid have been unsuccessful, an orthologous crystallization approach has been undertaken as homologous proteins have different propensities for crystallization. While the amino-acid sequences of homologues indicate a similar fold, there may be subtle differences so crystallization can occur under alternative conditions providing inhibited structures.[43] By pursuing this goal the chances of obtaining structures with inhibitors bound to the active site will increase. The other advantage of this approach is that a broader spectrum of DapE targets can be analyzed, which will provide additional structural insight to understand the mechanism of the DapE enzyme family. Ultimately we were able solve crystal structures of mono and di-zinc forms of DapE from *N. meningitidis* utilizing this approach, which will provide insight for the rational design of highly-selective inhibitors of DapE.

Conclusion

The importance of this project is accentuated by the increasing rate of antibiotic resistant bacteria, which has escalade to become a worldwide crisis. The research presented in this dissertation provides insight into substrate-binding as well as the mechanism of DapE, which has been identified as a potential antimicrobial target. Moreover, the information elucidated from the experimental data shine light onto the binding of inhibitors and provides important information required for the design of inhibitors of DapE enzymes. Rational design of inhibitors relies on understanding the active site structure and catalytic mechanism. Therefore, the DapE enzymes from *H. influenzae* and *N. meningitidis* were characterized biochemically and crystallographically. In addition, residues situated within the active site were mutated and characterized via kinetic and crystallographic methods to gain insight into substrate binding. In order to examine the role of the catalytic domain of DapE truncated enzymes from *Vibrio cholera* and *H. influenzae* were engineered by deleting their dimerization domains. Moreover, inhibition of DapE with L-captopril was investigated using several spectroscopic as well as crystallographic techniques, which produced the first inhibited structure of DapE. More importantly, the research has identified a viable assay for High Throughput Screening of Inhibitors, which allows for testing of a large number of inhibitors in a short period of time. This approach has allowed five new potential inhibitor of DapE to be identified, that can be used as synthons for future design of potent inhibitors. This work has provided information that could benefit the healthcare and the general wellbeing of society given that multidrug resistant bacteria pose a serious and increasing threat to human health.

CHAPTER TWO

THE ROLE OF THE DIMERIZATION DOMAIN AND THE ACTIVE SITE LOOP IN DAPE ENZYMES

Introduction

Emerging antibiotic resistance has been recognized as a world-wide health issue since the introduction of penicillin more than 80 years ago.[4, 44] Most importantly, the rapid emergence of resistant bacteria makes today's antibiotics more and more ineffective, consequently increasing the need for a novel class of antibacterial agents.[45] Currently available antibiotics target only a limited number of microbial pathways and employ two major strategies: (i) inhibition of cell wall remodeling and (ii) inhibition of protein synthesis.[46] As a result, only two new classes of antibacterial drugs have reached the market since 1962.[47, 48, 49] The Center for Disease Control and Prevention (CDC) recently reported the emergence of several strains of *Staphylococcus aureus* that are resistant to even the most powerful antibiotic of last resort, vancomycin. These cases emphasize the fact that no drug can prevent a simple staph infection from becoming deadly.[50] According to the Infectious Diseases Society of America (IDSA), a minimum of ten new systemic antibacterial drugs need to enter the market by the year 2020 in order to maintain proper control of infectious diseases. Therefore development of new classes of inhibitors that target essential metabolic pathways and unique enzymes is critical in order to maintain control of infectious diseases.[21, 51]

The lysine biosynthetic pathway offers several enzymes that could serve as potential drug targets. [52, 53, 54] Two products of this pathway, lysine and *meso*-diaminopimelate (*m*DAP), are essential for protein and peptidoglycan cell wall synthesis in Gram-negative and most Gram-positive bacteria. Many bacteria, plants and algae synthesize lysine and *meso*-diaminopimelic acid (mDAP) from succinic acid.[27-28, 53] In contrast, *lysine is* not synthesized in humans but it is an essential amino acid, therefore it must be ingested. It has been shown that deletion of the *dapE* gene in the mDAP/lysine biosynthetic pathway that encodes the *N*-succinyl-L,L-diaminopimelic acid desuccinylase (DapE) is lethal in *Helicobacter pylori* and *Mycobacterium smegmatis*.[55] DapE hydrolyzes *N*-succinyl-L,L-diaminopimelic acid to L,L-diaminopimelic acid and succinate.[53] DapE is a part of a biosynthetic pathway that is the major source of lysine in bacteria, and is essential for cell growth and proliferation. Since there are no similar biosynthetic pathways in mammals, inhibitors that target DapEs are hypothesized to exhibit selective toxicity against bacteria and have little or no effect on humans.[27] DapE coding genes have been identified in all pathogenic Gram-negative bacteria, and the enzyme has been purified and characterized from several sources.[55a, 55b, 56, 57, 58, 59] Of particular interest are DapEs from the "ESKAPE" pathogens, which are responsible for an increasing number of the antibiotic resistant nosocomial infections in the United States.[60] Alignment of the DapE gene from *Haemophilus influenzae* (*Hi*DapE) with the gene sequences of DapEs from "ESKAPE" pathogens reveals at least 49% identity.[61]

All the DapE enzymes characterized to date belong to the M20 family of dinuclear Zn(II)-dependent metalloproteases. Structural studies of M20 metalloproteases

showed that these enzymes exist as dimers comprised of catalytic and dimerization domains or monomers having a single catalytic domain.[62] Structural studies on *Hi*DapE revealed that the enzyme belongs to the former group composed of a larger thioredoxin-like 3-layer (αβα) sandwich domain that carries out catalysis and a smaller ferrodoxin-like domain providing the dimer interface. The core of the catalytic domain consists of an eight-stranded twisted β-sheet that is sandwiched between seven α-helices and houses the active site. The active site is constituted by residues from five loops, contains two zinc ions, and is exposed to the solvent.[63]

The architecture of the active site of *Hi*DapE and the core of the catalytic domain are strikingly similar to the aminopeptidase from *Aeromonas proteolytica* (AAP) and the carboxypeptidase from *Pseudomonas sp* strain-RS-16 (CPG2) [64], even though they catalyze markedly different hydrolytic reactions. One explanation for this similarity is the highly flexible design of their active sites, which are constructed by five loops. This design preserves the dinuclear catalytic core and at the same time allows for evolution of specificity for a new substrate without the need for major modifications to the overall structure. The flexibility of the active site is especially relevant from the perspective of understanding substrate recognition and binding which is directly related to inhibitor design. In order to examine the role of the catalytic domain of DapE enzymes and the role of the active site loops, we have engineered the *Hi*DapE and the DapE from *Vibrio cholerae* (*Vc*DapE) by deleting their dimerization domains. This truncation leads to protein constructs that have only the catalytic domain, are monomeric in solution, and closely resemble AAP. Kinetic characterization of the truncated DapEs (*Vc*DapE^{T} and

*Hi*DapE^{T}) shows that the activity of catalytic domain is not detectable under standard assay conditions. X-ray crystallographic data and molecular dynamic simulations along with site-directed mutagenesis studies provide insight into the role of the dimerization domain and emphasize the importance of the active site loops in catalysis.

Materials and Methods

Gene cloning and protein expression—The coding genes of full-length *Vc*DapE and *Hi*DapE that were cloned in vector pMCSG7 were amplified by PCR from *V. cholerae* O1 biovar El Tor str. N16961 (ATCC) and from *H. influenzae strain (ATCC) respectively* with *KOD* DNA polymerase using conditions and reagents according to the standard protocol described previously.[65] The truncated version of *Hi*DapE^{T} (residues 181-294 deleted) and *Vc*DapE^{T} (residues 181-295 deleted) were designed based on the full-length *Hi*DapE structure and were cloned using the same procedure. These deletion proteins were reengineered in such a way that the C-terminal domain was truncated at the connector region between the dimerization and the catalytic domains and replaced with a GG linker. The deletion of the region coding for the dimerization domain was achieved *via* PCR of pMCSG7-*Vc*DapE and pMCSG7-*Hi*DapE according to the previously described protocol.[66] The following primers were used: *Vc*DapE^{T} 181-295; 5'TGGCGGTGGCTTCCTGACCGATACGGGCGA3'and 5'GGAAGCCACCGCCACGACGGCCATTTTTCACC3', *Hi*DapE^{T} 181-294;5'CGGCGGTGGCTTTTTAACAAAACCAGGTAAATTATTAGATTCGATAACC 3' and 5'AAAAAGCCACC GCCGCGGCGACCATTTTTGAC3'. This process generated expression clones of fusion proteins that have the N-terminal His_6-tag followed

by a TEV protease recognition site (ENLYFQ↓S) followed by the DapE catalytic domain. All proteins were expressed in an *E. coli* BL21(DE3)-derivative that harbors the pMAGIC plasmid encoding one rare *E. coli* Arg tRNA (covering codons AGG/AGA). The transformed BL21(DE3) cells were grown at 37 °C in LB medium and protein expression was induced with 1 mM isopropyl-β-d-thiogalactoside (IPTG). The cells were then incubated and shaken vigorously at 18 °C overnight. The harvested cells were re-suspended in lysis buffer (500 mM NaCl, 5% (v/v) glycerol, 50 mM HEPES, pH 8.0, 10 mM imidazole, 10 mM 2-mercaptoethanol) and stored at −80 °C.

Purification of VcDapE, VcDapE^T and HiDapE^T—The *Vc*DapE, *Vc*DapE^T and *Hi*DapE^T proteins were purified according to the standard Ni-NTA affinity chromatography protocol described previously.[65] The 6-His tag was removed by treating each enzyme with TEV protease for 16 h at 4 °C in 50 mM HEPES, pH 7.5. Cleaved protein was separated from TEV using Ni-NTA affinity chromatography. After Ni-NTA column chromatography, *Vc*DapE^T and *Hi*DapE^T were further purified by size-exclusion chromatography on a HiLoad 16/600 Superdex 200 Prep Grade (GE Healthcare) using standard crystallization buffer (250 mM NaCl, 20 mM HEPES pH 7.5, and 1 mM TCEP) and concentrated to 25 mg/ml. The full-length *Vc*DapE protein was purified according to the same procedure however the size-exclusion chromatography step revealed formation of "soluble aggregates". Therefore, the buffer conditions were altered such that the salt concentration was increased to 800 mM NaCl and glycerol (10%) was added, allowing for purification of a small quantity of soluble protein.

Determination of Molecular Weight of VcDapE, VcDapE^T and HiDapE^T —The molecular weight (MW) of *Hi*DapE, *Hi*DapE^T and *Vc*DapE^T proteins in solution at concentration of 5 mg/ml was evaluated by size-exclusion chromatography (SEC) on a HiLoad 16/600 Superdex 200 Prep Grade column (GE Healthcare) in the crystallization buffer. The column was calibrated with aprotinin (6.5 kDa), ribonuclease A (13.7 kDa), carbonic anhydrase (29 kDa), ovalbumin (43 kDa), conalbumin (75 kDa), aldolase (158 kDa), ferritin (440 kDa), and thyroglobulin (669 kDa) as standards. The calibration curve of K_{av} *versus* log MW was prepared by using the equation $K_{av}=V_e–V_o/V_t–V_o$, where V_e=elution volume for the protein, V_o = column void volume, andV_t=total bed volume (Figure 11).

Figure 11. Analysis of the oligomeric state by size exclusion chromatograpy. Chromatogram showing elution of three DapE proteins (WT-*Hi*DapE (blue), *Hi*DapE^T (red), *Vc*DapE^T(green)) from the calibrated column. The inset shows the calibration curve obtained by plotting K_{av} *versus* logMW forthe following standard proteins: Aprotinin (6.5 kDa, I), ribonuclease A (13.7 kDa, II), carbonic anhydrase (29 kDa, III) ovalbumin (43 kDa, IV), conalbumin (75 kDa, V), aldolase (158 kDa, VI), ferritin (440 kDa, VII), and thyroglobulin (669 kDa, VIII).

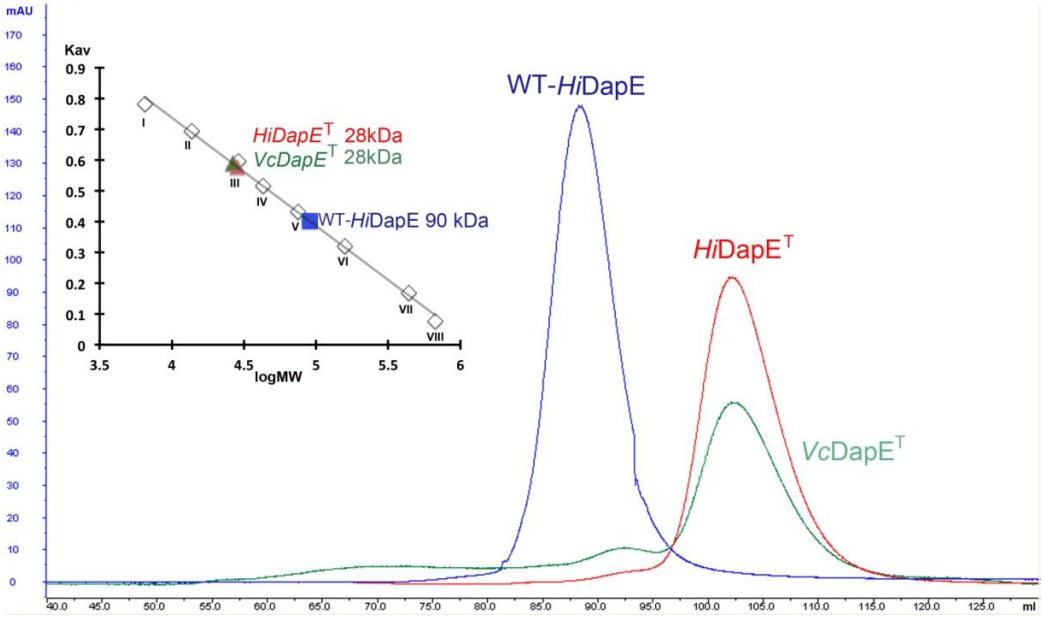

Kinetic characterization of VcDapE, VcDapE^T, and *HiDapE^T*—Recombinant WT-*Vc*DapE, *Vc*DapE^T, and *Hi*DapE^T were characterized biochemically by monitoring amide bond cleavage of L,L-SDAP at 225 nm (ε = 698 M^{-1} cm^{-1}). The assay was performed in triplicate in 50 mM phosphate buffer, pH 7.5, in the presence of two equivalents of Zn(II). Enzyme activities were expressed as units/mg where one unit is defined as the amount of enzyme that releases 1 µmol of L,L-SDAP at 25 °C in 1 min. K_m and k_{cat} values were obtained by fitting initial rates data to the Michaelis-Menten equation using Origin software.[59, 67] Catalytic activities were determined with an error of ± 10%.

Protein crystallization—The sitting-drop vapor-diffusion method was used to obtain crystals of *Vc*DapE^T and *Hi*DapE^T at 16 °C using a Mosquito liquid handling robot with 96 well plates. Crystals of both the apo- and dinuclear Zn(II)-loaded forms of *Vc*DapE^T were obtained using 400 nl of a precipitant solution (20% (v/v) 1,4-butanediol, 0.1 M sodium acetate pH 4.5) and 400 nl of a 19 mg/ml solution of *Vc*DapE^T in crystallization buffer within 14 days. In order to grow the crystals of dinuclear Zn(II)-loaded forms of *Vc*DapE^T 1mM $ZnCl_2$ solution was added to the protein solution.

Crystals of *Hi*DapE^T were obtained using 400 nl of a precipitant solution (0.2 M ammonium acetate, 0.1 M BIS-TRIS pH 5.5, 25% (w/v) polyethylene glycol 3350) and 400 nl of a 15 mg/ml solution of *Hi*DapE^T within two weeks. The asymmetric unit contains two monomeric molecules of the *Hi*DapE^T. For cryoprotection, all crystals were transferred to, the mother liquid containing 25% mixture of glycerol and ethylene glycol.

Data collection and structure determination—Prior to data collection, the X-ray florescence spectrum was recorded for *Vc*DapE^T, *Hi*DapE^T and apo-*Vc*DapE^T crystals,

which identified the presence of Zn ions in the protein crystals of *Vc*DapE^T and *Hi*DapE^T. Data collection was carried out on the 19-ID beam line of the Structural Biology Center at the Advanced Photon Source according to procedures described previously.[63] Data were collected at a wavelength of 0.98 Å from the single crystals and were processed using HKL3000. Crystallographic parameters are summarized in Table 2. Initially data for both *Vc*DapE^T were processed, scaled and structures were refined in the space group $P3_212$. Even though models refined to low R-factor (R_{cryst}/R_{free}= ~16/18%), the spurious density features were observed in the electron density maps. Re-examination of the data and twinning test performed using Xtriage in Phenix [68] indicated a perfect twinning with the twinning operator parallel to two-fold axis making it pseudo $P3_212$. Therefore data were rescaled in the space group $P3_2$. The structures of *Vc*DapE^T and *Hi*DapE^T were determined by molecular replacement using the catalytic domain of *Hi*DapE (PDB ID 3IC1) as a search model.[63] Molecular replacement searches were completed using MOLREP of the CCP4 suite.[69] The initial models were rebuilt manually and refined using programs REFMAC 5.5 [70] and Phenix.[68] The final models were refined against all reflections except for 5% randomly selected reflections, which were used for monitoring R_{free}. The final rounds of refinement were carried out using TLS refinement with 5 TLS groups. The final refinement statistics for all structures are presented in Table 2. Analysis and validation of the structures were performed with the aid of MOLPROBITY and COOT validation tools. Figures were prepared using program Pymol.

Table 2. Data and Refinement Statistics for *Vc*DapE^T-apo, *Vc*DapE^T-ZnZn and *Hi*DapE^T-ZnZn.

Data collection statistics	*Vc*DapE^T-apo	*Vc*DapE^T-ZnZn	*Hi*DapE^T-ZnZn
Space group	$P3_2$	$P3_2$	$P2_1$
Unit cell (Å)	a = 49.6, b =49.6, c = 232.6	a = 49.9, b =49.9, c = 231.8	a = 61.7, b = 44.7, c = 92.5, □ = 92.9^o
Resolution (Å)	37.6-1.65	40-1.65	30-1.84
Wavelength (Å)	0.98 Å	0.98	0.98
Number of observed reflections	523779	299329	99336
Number of unique reflections	77006	70716	42453
Redundancy [b]	6.8 (3.8)	4.2(1.8)	2.3(2.2)
R_{merge} [a,b] (%) R_{rim} [a,b] (%) R_{pim} [a,b] (%)	5.9 (50.1) 6.4 (56.7) 2.4 (25.8)	5.1 (26.0) 5.8 (35.5) 2.6 (23.1)	9.2 (55.7) 10.5(82.6) 6.5(51.0)
Completeness[b] (%)	99.6 (93.8)	91.3 (49.2)	96.5 (97.8)
I/σ	40 (2.3)	23.2 (2.1)	9.5 (2.1)
Phasing			
phasing method	**MR**	**MR**	**MR**
Refinement statistics			
R_{cryst} (%)	13.81	14.32	19.7
R_{free} (%)	17.13	16.59	24.9
protein residues	532	513	505
zinc ion/acetate/butanediol/ glycerol/ethanediol/	-/1/6/2/4	2/-/6/3/3	4/-/-/-/-
solvent	541	541	284
Rmsd from target values			
bond lengths (Å)	0.020	0.020	0.021
bond angles (deg)	2.11	1.43	2.03
Average *B* factors (Å^2)			
protein	14.78	14.77	27.7
Zn	-	13.93	26.1
H_2O	28.10	24.19	38.7
PDB ID	4ONW	4OP4	4H2K
Ramachandran (%)[c] M.F./A.A.	97.5/2.5	97.3/2.7	96.8/3.0

[a] $R_{merge} = \Sigma_{hkl}\Sigma_i|Ii_(hkl_) - I_{hkl}|/\Sigma_{hkl}\Sigma_i I_{i(hkl)}$, where $Ii_(hkl_)$ is the *i*th observation of reflection *hkl*, and $\langle I_{hkl}\rangle$ is the weighted average intensity for all observations *i* of reflection *hkl*.
$R_{rim} = \Sigma_{hkl}(N/(N-1)^{1/2})\Sigma_i|Ii_(hkl_) - \overline{Ihkl}|/\Sigma_{hkl}\Sigma_i I_{i(hkl)}$, and $R_{pim} = \Sigma_{hkl}(1/(N-1)^{1/2})\Sigma_i|Ii_(hkl_) - \overline{Ihkl}|/\Sigma_{hkl}\Sigma_i I_{i(hkl)}$.
[b] Numbers in parentheses are values for the highest-resolution bin.
[c] As defined by MOLPROBITY (M.F. –the most favored/ A.A additionally allowed)

Protein Data Bank accession code—The atomic coordinates and structure factor file for the structure of the catalytic domain of apo-*Vc*DapE^{T}, ZnZn-*Vc*DapE^{T} and ZnZn-*Hi*DapE^{T} have been deposited in the RCSB Protein Bank with accession code 4ONW, 4OP4 and 4H2K, respectively.

Molecular modeling and dynamics simulations—The structure of the catalytic domain of *Vc*DapE^{T} is well ordered and excellent electron density is observed for protein main-chain, side-chains, metal, phosphate ions, and water molecules. Using the VMD molecular graphics program [71], the protein model with its hydrogen atoms was created and placed in a water-box containing 7826 TIP3 water molecules [72], 13 sodium, and 2 chloride ions to neutralize the charge and provide counter ions. The charges on the histidine residues were determined by inspection of their local environments. The energy of this initial structure was minimized with 3,000 steps of conjugated gradient minimization using the CHARMM27 force field [73] and the NAMD molecular dynamics (MD) program.[74] The structure was relaxed by gradually heating it from 10 to 310 K in steps of 10 K with 1,000 steps of molecular dynamics at each temperature. Periodic boundary conditions were used. The cutoffs for non-bonding (van der Waals and electrostatic) interactions were 12 Å. The switch distance was 10 and 1.0 Å using a 1–4 scaling factor. The time step was 2 fs. These conditions were used for all of the molecular dynamics simulations. After 10,000 steps of pressure and temperature equilibration using a Langevin piston, the system was subjected to 30,000 steps of molecular dynamics. This process constitutes equilibration of the structure. The structures for *Hi*DapE^{T} and *Hi*DapE were also equilibrated in the same manner. Since

these X-ray structure models had a few loops missing due to the poor electron density maps, the missing regions were modeled using the modeling tools found in Swiss PDB Viewer.[75] The complete *Vc*DapE structure was produced through homology modeling, using *Hi*DapE as a template through the automated mode of the Swiss Model service.[76] The two chains of *Vc*DapE were produced separately from each other, combined using VMD, and equilibrated in the manner previously described. The X-ray structure for AAP (PDB ID 1RTQ) [64b] was used as a standard for comparison as AAP and dinuclear Zn(II)-loaded *Vc*DapE^T and *Hi*DapE^T are characterized by similar active sites and sequence lengths. For each of these five structures, 5 ns of simulation data were accumulated. The rmsd per residue values were calculated for MD production runs of the four structures using the VMD molecular graphics program.[71] These calculations were used to determine structural changes between each of the five structures. MOLMOLplots [77] were also generated for each structure to give a visual depiction of the structural changes, especially for areas of large movement. For these diagrams 171 equally spaced snapshots over a 5 ns simulation were used for each of the five proteins. Three of the simulations (ZnZn(*Vc*DapE^T), *Hi*DapE^T and *Hi*DapE) were run for 10 ns, but there were no significant differences in the flexibilities of these when the second 5 ns were compared with the first 5 ns. All of the MOLMOL plots (Fig 13 and 14) used only the first 5 ns of data so that they are directly comparable.

Loop V Site Directed Mutagenesis—The site-directed mutants T325A, T325S and T325C of WT-*Hi*DapE were prepared using the Quick Change Site-Directed Mutagenesis Kit (Stratagene) following the procedure outlined by Stratagene using the following

primers, T325A: 5'-ACAGGTGGCGGCGCGTCAGACGGTC-3', 5'-GACCGTCTGACGCGCCGCCACCTGT-3', T325S: 5'-ACAGGTGGCGGCTCGTCAGACGGTC-3', 5'-GACCGTCTGACGAGCCGCCACCTGT-3', T325C: 5'-GCTGAAACAGGTGGCGGCTGCTCAGACGGTCGTTTTATT-3', 5'-AATAAAACGACCGTCTGAGCAGCCGCCACCTGTTTCAGC-3'. Polymerase Chain Reaction (PCR) was performed using 70 ng of a dsDNA template. PCR was performed at 95 °C for 30 seconds followed by 16 cycles of (95 °C for 30 seconds, 55 °C for 1 minute, 68 °C for 5 minutes) and final extension at 68 °C for 6 minutes. Reaction products were transformed into BL21(DE3)/magic *E. coli* competent cells (Invitrogen) and grown on Luria-Bertani agarose plates containing ampicillin (100 μg mL^{-1}) and kanamycin (25 μg mL^{-1}). A single colony of each mutant was grown in 5 mL Luria-Bertani medium containing ampicillin (100 μg mL^{-1}) and kanamycin (25 μg mL^{-1}). Plasmids were isolated using the QIAprep-Spin Miniprep Kit (QIAGEN). The plasmid DNA was sent to the DNA sequencing facility (University of Chicago Cancer Research Center DNA Sequencing Facility, Chicago IL) to confirm the mutations. Glycerol stocks were prepared and stored at -80 °C until further needed. Purification of *Hi*DapE T325A, T325C and T325S mutant enzymes and kinetic characterization was conducted as described above.

Circular Dichroism (CD) Spectroscopy— The secondary structure of WT DapE and T325 mutants were measured using Olis DSM 20 circular dichrometer. Data was collected at room temperature with constant nitrogen flow every 1 nm, in the wavelength

range of 190 - 260 nm. All samples were measured in a cylindrical quartz cuvette with a 1 mm pathlength in 10 mM phosphate buffer pH 7.0. Three repetitive scans were averaged, smoothed and background-subtracted for each measurement. Millidegree values obtained were converted to molar ellipticity ($deg \cdot cm^2 \cdot dmol^{-1}$) by using the equation: Molar ellipticity = $m_oM/10 \times L \times C$, where m_o is millidegrees, M is molecular weight (g/mol), L is path length of cuvette (cm) and C is concentration (g/L). CD data from 190 to 260 nm were also analyzed to estimate the secondary structure composition of Wild type and the mutants using the CDSSTR program in Dichroweb.[78]

Results

Kinetic characterization of wild type and truncated DapE—Kinetic data were obtained for recombinant *Vc*DapE, *Hi*DapE, *Vc*DapE^T, and *Hi*DapE^T by monitoring amide bond cleavage of L,L-SDAP at 225 nm. The k_{cat} value obtained for WT-*Vc*DapE was 80 ± 10 s^{-1} with a corresponding K_m value of 1.2 ± 0.2 mM while the k_{cat} value obtained for *Hi*DapE was 114 ± 10 s^{-1} with a K_m value of 0.8 ± 0.1 mM, which is in good agreement with previous studies.[67b] Surprisingly, no detectable activity was observed for *Hi*DapE^T or *Vc*DapE^T under the standard assay conditions.

*Structure of the catalytic domain of Hi*DapE^T—Deletion of the dimerization domain led to a monomeric structure for *Hi*DapE^T. The monomeric nature of *Hi*DapE^T in solution was corroborated by size exclusion chromatography (SEC) The SEC analysis confirmed a weight (MW) of 28.4 kDa (the theoretical mass of a monomer is 28.9 kDa, while the wild-type dimer's theoretical mass is 82.6 kDa) (Figure 11). The structure of *Hi*DapE^T was determined and refined at 1.84 Å resolution and the final model shows two

independent monomers in the asymmetric unit. The structure of the catalytic domain is virtually identical to the catalytic domain of full-length *Hi*DapE (PDB ID 3IC1) (Figure 12A, B, & C).[63] Both structures overlay closely with rmsd for Cα atoms of 0.65 Å over 254 residues. Two zinc atoms were found in the active site and reside in the same position as in dimeric structure of WT-*Hi*DapE separated by 3.40 Å. Superimposition of the active site regions shows nearly identical conformations of main chain and side chains with rmsd as low as 0.15 Å for the metal ions and side chains of residues involved in their coordination (Figure 12C). Therefore the structure of the catalytic core of the enzyme is extremely well preserved. Larger differences within the active site area are observed in two regions containing solvent exposed loops. Region I (residues 176-187) has been engineered to replace what was originally the connector/hinge region formed by two loops linking the catalytic domain with the dimerizaton domain (Figure 12C, Region I). This region is highly flexible and is disordered in the crystal structure of *Hi*DapE^{T} (with no electron density observed for residues 182-187). Region II (residues 209-224), which corresponds to a loop overhanging the active site metal ions (loop V, *vide infra*) adopts a different conformation in comparison to that observed in the *Hi*DapE structure (rmsd of 1.5 Å between the structures). Two residues within loop V (Gly21 and Gly212) are disordered in the structure of *Hi*DapE^{T} (Figure 12C).

Figure 12. X-ray Crystal Structures of WT-*Hi*DapE and *Hi*DapE^{T}. (A) Dimer architecture based on the structure of WT-*Hi*DapE. (B) Close-up view of the catalytic domain of WT-*Hi*DapE. Ribbon diagram showing the active site formed by six loops (LI-LVI); five of them coordinate the Zn ions (LI-IV & VI). (C) Superimposition of the structure of WT-*Hi*DapE (black) over *Hi*DapE^{T} (magenta). Active site Zn(II) ions are shown as black and magenta spheres for WT-*Hi*DapE and *Hi*DapE^{T}, respectively. Regions where differences are most prominent are labeled Region I (yellow) and Region II (orange). Yellow and magenta circles highlight two disordered loop regions in the *Hi*DapE^{T} structure. The red dots marked disordered loop that contains conserved His residue.

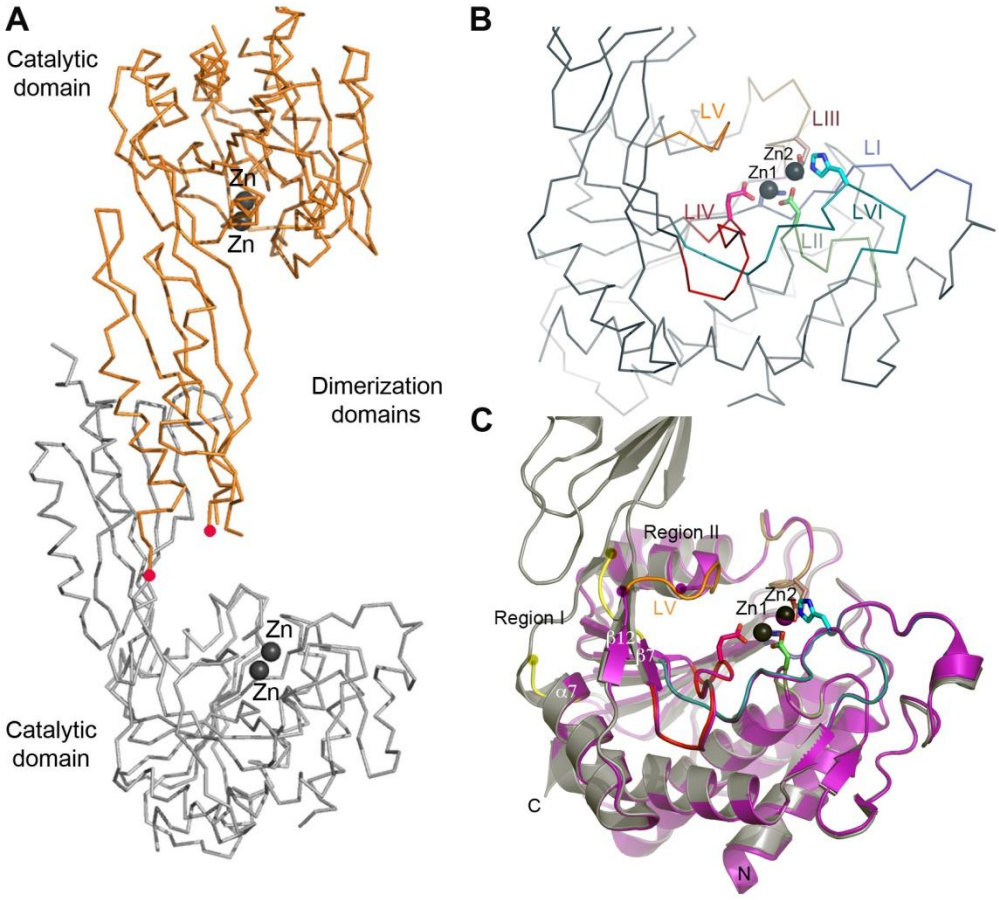

*Structure of the catalytic domain of Vc*DapE^T—The monomeric state of *Vc*DapE^T was confirmed by SEC (the estimated MW of 28.7 kDa). Two *Vc*DapE^T structures were determined, the apo- and the dinuclear Zn(II)-loaded form. The final models for both apo- and Zn(II)-loaded *Vc*DapE^T included two molecules of the catalytic domain in the asymmetric unit. The two *V. cholerae* structures are virtually identical and superimpose with the average rmsd of 0.25 Å for 265 equivalent Cα atoms suggesting that binding of Zn(II) does not induce any major structural changes (Figure 13A). The structures of the catalytic domains of both apo- and Zn(II)-loaded *Vc*DapE^T closely resemble that of the catalytic domain of active WT-*Hi*DapE (PDB ID 3IC1). Superimposition of the Zn(II)-loaded *Vc*DapE^T structure and Zn(II)-loaded *Hi*DapE^T shows that they also overlay closely with (the average rmsd of 0.81 Å for 248 equivalent Cα atoms, Z-score 17, sequence similarity 59%) (Figure 3B). Likewise, the structure of Zn(II)-loaded *Vc*DapE^T is almost identical to that of the catalytic domain of the full-length *Hi*DapE with rmsd of 1.15 Å. The similarity between these structures is especially apparent within the active site region of Zn(II)-loaded *Vc*DapE^T as the active site structure differs by only ~0.45 Å rmsd with the active site of *Hi*DapE^T and ~0.4 Å with the WT-*Hi*DapE (Figure 13A and B). Similarly to *Hi*DapE^T, the most flexible regions of the protein are Region I and Region II. Region I corresponds to the engineered loop (the connector) where the deleted dimerization domain is replaced with two glycines. Region II (residues 210-224) forms a loop overhanging the active site metal ions, which includes residues 211-213 that form part of loop V (*vide infra*) (Figure 13B).

*The active sites of Hi*DapE^T *and Vc*DapE^T—The sequence identity of *Hi*DapE and *Vc*DapE is high (59%), and the residues comprising the active site are fully conserved. The active site of DapE is located in the center of the catalytic domain above the centrally located parallel strands of the β-sheet and is formed by six loops [loop I (*H. influenzae* notation, residues 68-75), loop II (residues 95-102), loop III (residues 132-141), loop IV (residues 162-174), loop V (residues 322-328 in *Hi*DapE) and loop VI (residues 341-355)] (Figure 12B). With the exception of loop V that does not interact with the zinc ions, the remaining loops contribute the conserved residues that coordinate the metal ions (Figures 12B, 12C & 13B). Interestingly, loops I-IV and VI are in virtually identical orientations in both *Vc*DapE^T and *Hi*DapE^T and overlay very well with the corresponding loops in the WT-*Hi*DapE. A change is observed in loop V which in *Vc*DapE^T adopts a confirmation that is significantly different from the one observed for WT-*Hi*DapE (Figures 12A & 13B) (in *Hi*DapE^T this loop is disordered). The active site of Zn(II)-loaded *Vc*DapE^T contains a (μ-oxygen)(μ-carboxylato)dizinc(II) core with one terminal carboxylate and one histidine residue at each metal site ([ZnZn(*Vc*DapE^T)]), that is identical to the active site observed for WT-*Hi*DapE.[63] The main difference between the active sites in the two Zn(II)-loaded *H. influenzae* structures (WT-*Hi*DapE and *Hi*DapE^T) and [ZnZn(*Vc*DapE^T)] is the presence of additional electron density in chain A, which is overlapping with the bridging water/hydroxide molecule observed in chain B and WT-*Hi*DapE. The $2F_o$-F_c and F_o-F_c electron density maps were quite clear and indicate that a small molecule (most likely ethylene glycol or a partially disordered glycerol molecule) (Figure 3C) displaces the bridging water/hydroxide molecule in the [ZnZn(*Hi*DapE)] and [ZnZn(*Hi*DapE^T)]

structures. Both of these compounds were present in the cryoprotectant solution. Based on the best fit, an ethylene glycol molecule was modeled in the active site resulting in distorted tetrahedral coordination geometry for Zn1, which is bound by the carboxylate

Figure 13. X-ray Crystal Structures of *Vc*DapE^T. (A) Superimposition of apo-*Vc*DapE^T (blue) over [ZnZn(*Vc*DapE^T)] (cyan), showing the identical nature of the catalytic domains. Zinc atoms for *Vc*DapE^T are shown as black spheres. (B) Comparison of [ZnZn(*Vc*DapE^T)] (cyan) and [ZnZn(*Hi*DapE^T)] (magenta). Regions I (yellow) and II (orange) identify the areas where the most significant differences between the two structures exist. Six loops (LI-LVI) forming the active site are labeled. Zinc atoms for *Vc*DapE^T are shown as black spheres while the residues coordinating the metal ions are shown as lines. (C) Close-up view of the active site environment of the [ZnZn(*Vc*DapE^T)] with the $2F_o-F_c$ electron density map (with the Zn ions and ethylene glycol molecules omitted from the calculation). (D) Close-up view of residues from loops I-IV and VI interacting with the Zn(II) ions in the structure of [ZnZn(*Vc*DapE^T)]. (E) The 2Fo-Fc (blue, 1 σ) and Fo-Fc electron-density maps (red and green at -3σ and 3σ) of the LV loop region in *Vc*DapE^T.

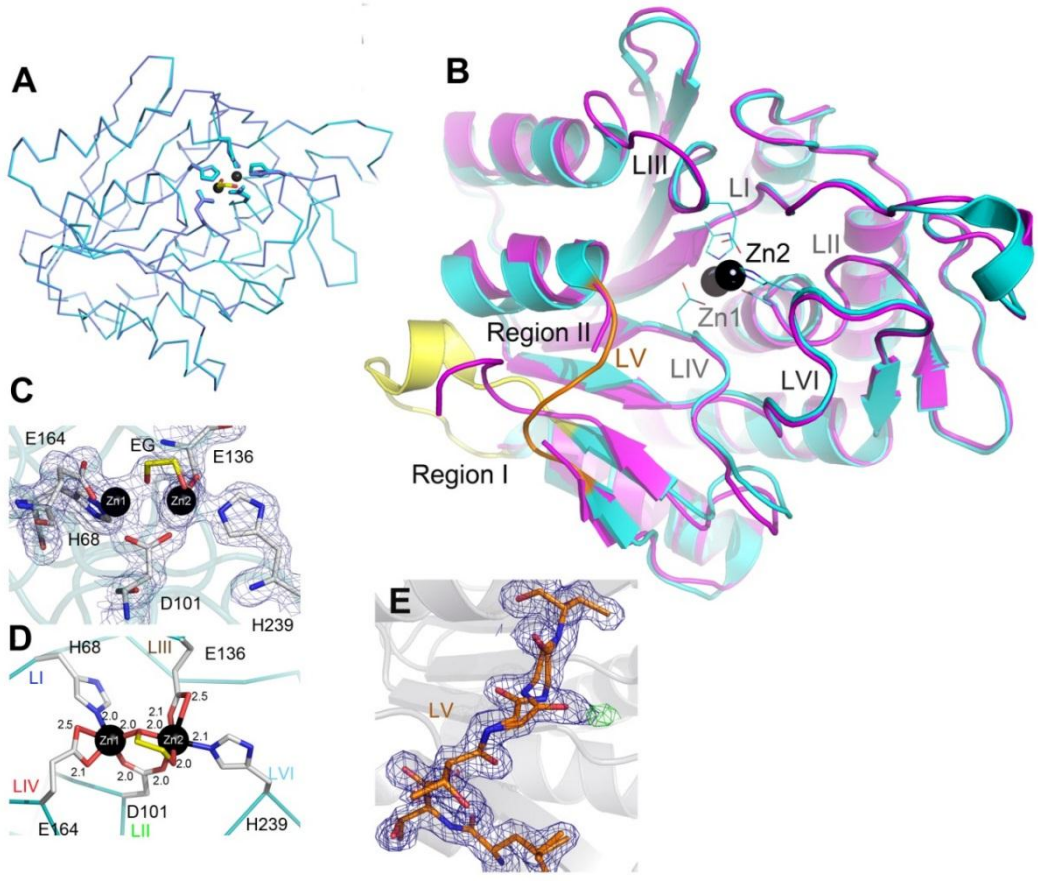

oxygen atoms OD1 of D101 and OE1 of E164 as well as a nitrogen atom NE2 of H68. Zn2 adopts a distorted trigonal bipyramidal geometry and is coordinated by the bridging O2 oxygen atom from ethylene glycol, a nitrogen atom NE2 of H239, two oxygen atoms, OD2 from D101 and OE2 from E136, and the O1 oxygen atom of ethylene glycol (Figure 3D). The Zn1-Zn2 distance is 3.39 Å.

Molecular Modeling and Dynamics—MD calculations were performed for five proteins: *Vc*DapE^{T}, *Hi*DapE^{T}, WT-*Vc*DapE, WT-*Hi*DapE and AAP. After equilibration, the rmsd values for the main-chain atoms of [ZnZn(*Vc*DapE^{T})] and [ZnZn(*Hi*DapE^{T})] were compared with the original X-ray structures and only small changes were observed. Similarly, small changes were seen after equilibration of *Vc*DapE and *Hi*DapE as well as AAP, which is monomeric and contains a single catalytic domain. Since only the two truncated proteins were catalytically inactive, particular attention was given to how these proteins differed from the other three. Figure 4 shows the results of the 5 ns molecular dynamics simulations of the truncated proteins and comparisons to their crystallographic temperature factors. The thickness of the line indicates the flexibility of the structure at a given point during simulation (Figure 14A and B). The portions of [ZnZn(*Vc*DapE^{T})] that have the greatest flexibility are the created dimerization domain loop which was excised and the active site loop V (Figure 13). This is consistent with the crystallographic atomic displacement parameters indicating that the most dynamic portions includes residues 177-187 and loop V (Figure 14C). Compared to the other three structures, the two truncated proteins have greater flexibility in both of these loops (Figure 14) than the catalytically active domains (Figure 15).

Mutation of the Loop V Residue T325—Since both X-ray crystallographic and MD simulations suggested that loop V flexibility increases in *Vc*DapE^{T} and *Hi*DapE^{T}, it was hypothesized that this loop plays an important role in constituting the active site and possibly substrate recognition and/or transition-state stabilization. Since T325 in *Hi*DapE is centrally positioned in loop V directly above the dinuclear Zn(II) site (Figure 16), the site-directed mutants T325A, T325S and T325C were prepared and purified. The k_{cat} value obtained for T325A using L,L-SDAP as the substrate was 4 ± 0.5 s^{-1} with a corresponding K_m value of 2.1 ± 0.2 mM while the k_{cat} value obtained for T325S was 2.9 ± 0.3 s^{-1} with a K_m value of 3.0 ± 0.3 mM. Interestingly, when T325 was replaced by cysteine, no enzyme activity was observed under standard assay conditions. CD spectra obtained for each mutant enzyme plus WT-*Hi*DapE, indicate that there is no significant structural change in the mutant enzymes compared to WT-*Hi*DapE (Figure 17, Table 3). These data confirm that T325 and hence the position of loop V is important for the active site organization and catalysis.

Figure 14. Diagrams showing regions of flexibility in truncated DapE proteins**.** (A) MOLMOL diagram of [ZnZn(*Vc*DapE^{T})] molecular dynamics. (B) MOLMOL diagram of [ZnZn(*Hi*DapE^{T})] molecular dynamics (the thickness of the line is proportional to the variation of the protein structure during the simulation). The crystallographic temperature factors indicating that the most dynamic (in red) and the most rigid (in blue) parts of the protein : (C) [ZnZn(*Vc*DapE^{T})]. (D) [ZnZn(*Hi*DapE^{T})].

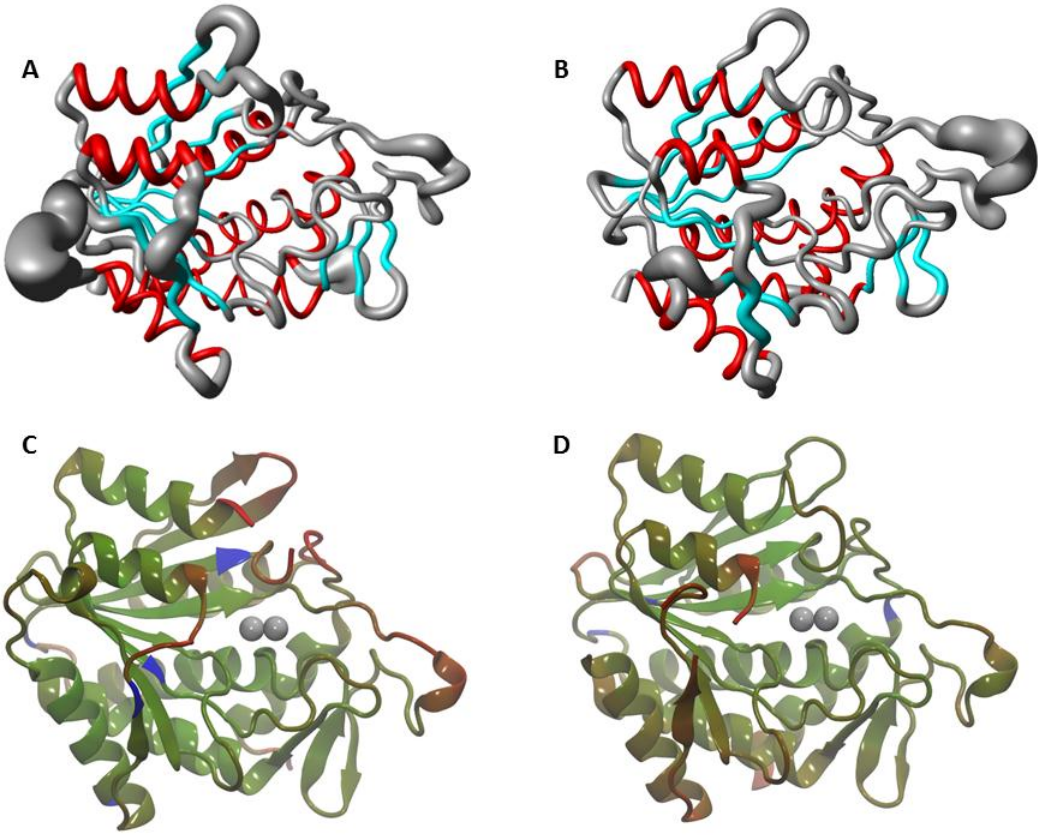

Figure 15. Molecular dynamic simulations showing regions of flexibility in catalytic domain. (A) [ZnZn(*Vc*DapE)]. (B) [ZnZn(*Hi*DapE)]. (C) AAP. The thickness of the line is proportional to the variation of the protein structure during the simulation. AS indicates the active site area, LVeq. equivalent of the LV loop in *Hi*DapE).

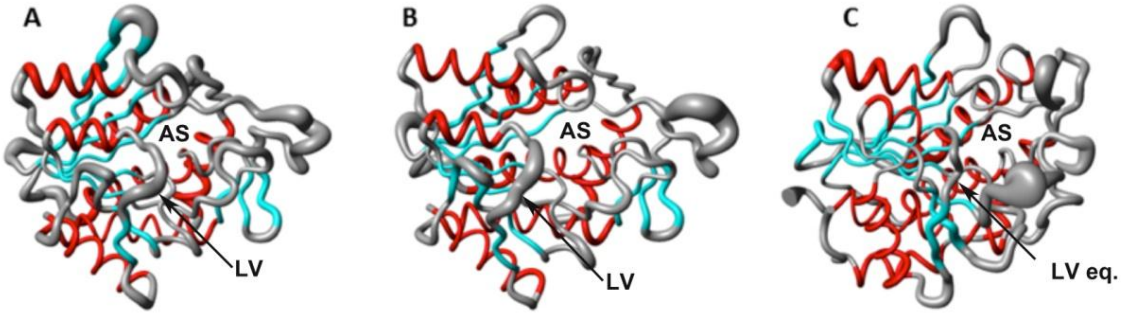

Figure 16. The active site of WT-*Hi*DapE showing loop V. T325 resides on loop V directly over the dinuclear active site.

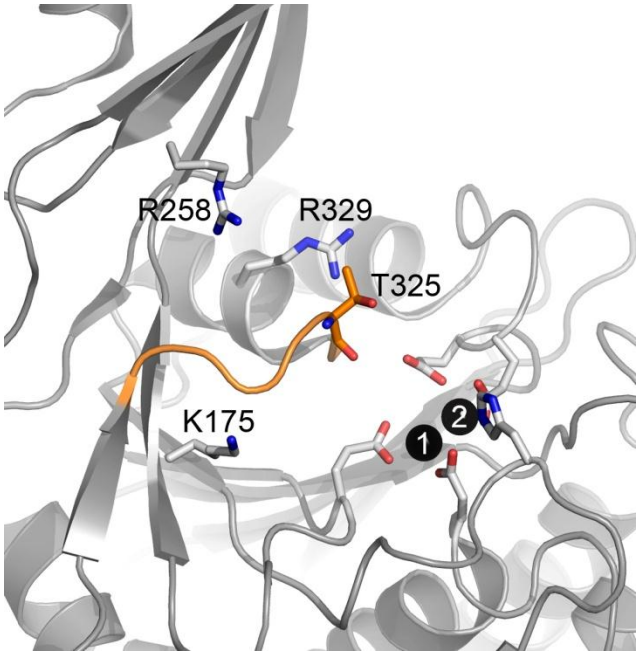

Figure 17. Circular Dichroism spectra of WT DapE (—), T325A (···), T325C (-) and T325S (-···).

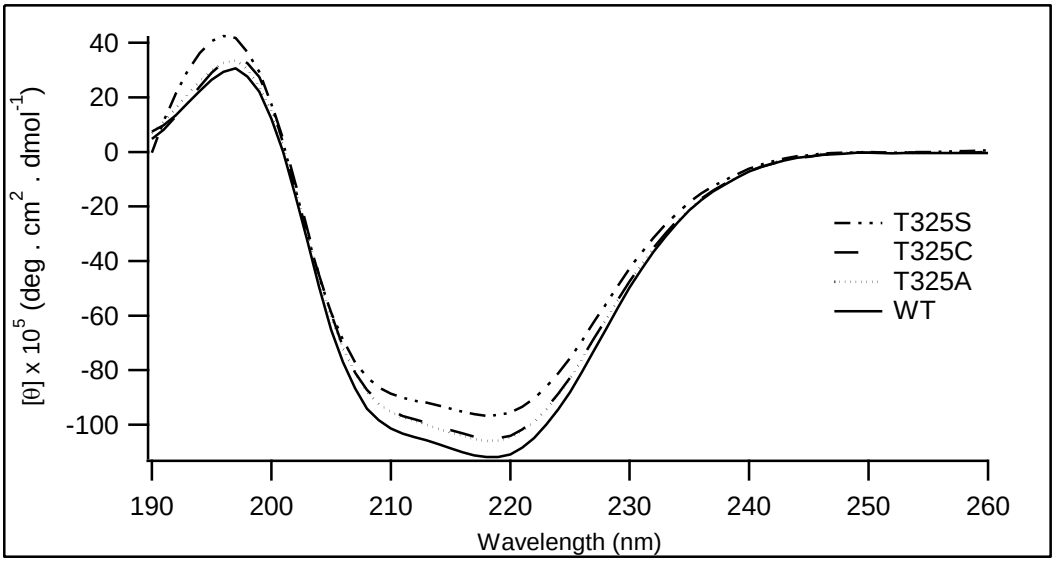

Table 3. Circular dichroism spectroscopy analysis of WT DapE and threonine mutants.

	Helix 1	**Helix 2**	**Strand 1**	**Strand 2**	**Turns**	**Unordered**	**Total**
Wild Type	0.24	0.05	0.20	0.12	0.17	0.23	1.01
T325A	0.23	0.07	0.19	0.12	0.15	0.23	0.99
T325C	0.23	0.05	0.18	0.12	0.19	0.22	0.99
T325S	0.30	0.06	0.17	0.11	0.14	0.21	0.99

Results are shown as proportions of each protein predicted to be folded in each of the indicated secondary structural conformations, or predicted to be unordered.

Discussion

Sequence comparison of all M20 classified metallopeptidases and the M28 family of dinuclear Zn(II)-dependent metalloproteases, which include AAP and CPG2 [62, 64], shows that all of the metal coordinating residues are strictly conserved.[53, 67b, 79]. Unlike

AAP, which is monomeric, DapE enzymes form dimers where each subunit consists of two functional domains: a larger catalytic domain, which houses the active site and a dimerization domain that forms the dimer interface (Figure 12A). The location and architecture of the catalytic domain and the dinuclear Zn(II) active site in dimeric WT-*Hi*DapE is nearly identical to the catalytic domain and the active site of monomeric AAP.[64a, 80] The catalytic domain of *Hi*DapE is composed of residues 1–179 and 293–376 where the core of the catalytic domain contains an eight-stranded twisted β-sheet that is sandwiched between seven α-helices. The active site is located in the center of the catalytic domain above the centrally located parallel strands of the β-sheet and is constituted by six loops. With the exception of loop V that encloses the active site from the top and does not interact with the zinc ions, the remaining loops contribute the conserved residues that coordinate the metal ions (Figure 12B). The dimerization domain of *Hi*DapE consists of a 114-residue insertion into the catalytic domain and is connected to the catalytic domain by two short loops. Since the dimerization domain is located away from the active site and has only limited interaction with the catalytic domain *via* loop V, it is unclear whether this domain plays any role in catalysis. Such a role for the dimerization domain would require a major conformational change to bring the dimerization domain residues into the active site. While this is possible, the time frame would be well beyond the range of atomistic MD simulations.

To address this issue we engineered DapE enzymes by removing their dimerization domains (*Hi*DapE^{T}, *Vc*DapE^{T}). The nested truncation was designed based on WT-*Hi*DapE crystal structures with the goal of preserving the catalytic domain

structure and keep its active site intact. The *Hi*DapE^T and *Vc*DapE^T constructs expressed well, were purified, the monomeric states of both proteins in solution was confirmed and their catalytic activities examined. Surprisingly, we could not detect enzyme activity for either truncated variant towards L,L-SDAP, whereas WT-*Hi*DapE exhibited k_{cat} and K_m values in good agreement with those previously reported.[67b] For comparison purposes, the k_{cat} and K_m were also determined for WT-*Vc*DapE and found to be similar to the values reported for WT-*Hi*DapE. These data suggest that the deletion mutants have significantly diminished catalytic activity or are fully catalytically inactive.

To understand the structural basis of the observed absence of catalytic activity of both engineered enzymes, we determined the crystal structures of the truncated forms of *Hi*DapE^T ([ZnZn(*Hi*DapE^T)]) and *Vc*DapE^T ([ZnZn(*Vc*DapE^T)]) along with the apo-form of *Vc*DapE^T. These structures reveal that the catalytic domain is indeed unchanged, including complete structural preservation of the catalytic site and metal core. It is clear that deletion of the dimerization domain does not compromise the catalytic domain structure. The structure of [ZnZn(*Hi*DapE^T)] is virtually identical to the catalytic domain the WT-*Hi*DapE with an rmsd of 0.8 Å for 248 equivalent Cα atoms. Interestingly, the newly determined structure of [ZnZn(*Vc*DapE^T)] also shows high similarity to the catalytic domain of WT-*Hi*DapE with an rmsd of 1.15 Å for 246 equivalent Cα atoms. Since the structures of *Vc*DapE^T were determined in both the apo- and dinuclear Zn(II)-loaded forms, it is evident that removal of either the dimerization domain or the metal cations does not alter the overall structure of the catalytic domain. The dinuclear Zn(II) active sites in both *Hi*DapE^T and *Vc*DapE^T are nearly identical to each other with Zn-Zn

distances of ~3.40 Å. These Zn-Zn distances are comparable to those observed for AAP (3.45 Å), *Hi*DapE (3.33 Å) and carboxypeptidase G2 (CPG2) (3.25 Å).[64b, 79b] Similar to AAP, *Hi*DapE, and CPG2 one of the Zn(II) ions in [ZnZn(*Vc*DapE^T)] adopts a distorted tetrahedral geometry while the second Zn(II) ion is trigonal bipyramidal. Identical to CPG2, *Hi*DapE, and AAP each zinc ion is coordinated by one imidazole group (H68 for Zn1 and H239 for Zn2) and the oxygen atoms of E164 for Zn1 and E136 for Zn2. Both zinc ions are bridged by D101 and a single oxygen atom of ethylene glycol (in the molecule one, chain A) or water molecule (in the second molecule, chain B). Overall the [ZnZn(*Vc*DapE^T)] structure confirms that the metal ions form a (μ-oxygen)(μ-carboxylato)dizinc(II) core similar to *Hi*DapE, AAP, and CPG2 [81], and indicates that the active site catalytic unit is intact in the truncated forms of DapE. Therefore, the lack of the catalytic activity is puzzling and clearly is not due to missing a key element in the *Hi*DapE^T and *Vc*DapE^T dinuclear active site.

Comparison of the [ZnZn(*Hi*DapE^T)] and [ZnZn(*Vc*DapE^T)] structures with that of WT-*Hi*DapE (PDB ID 3IC1) (Figure 12C & 13B) reveals that one of the six loops comprising the catalytic core, loop V (residues 210-214 in *Hi*DapE^T and 211-215 in *Vc*DapE^T, and corresponding to 321-325 in *Hi*DapE) exist in significantly different orientations than that observed in WT-*Hi*DapE. Interestingly, this loop is also partially disordered in the structure of *Hi*DapE^T, while in *Vc*DapE^T structures its conformational flexibility is signified by the double conformation of the main chain Gly 213 (peptide flip). In our previous studies, we proposed that this loop might be involved in the positioning and stabilization of the substrate in the active site, therefore the loop

conformation might be critical for proper substrate binding and positioning as well as stabilization of the transition-state during the catalytic cycle.[63] This is supported by two loop V mutations (T325A, T325S) that show similar K_m to WT but significantly reduced (25-50 times) k_{cat} values. These data suggest that the substrate is bound with similar specificity, but is not effectively presented to the catalytic core for successful catalysis. Since the same region is affected in both *Hi*DapE^T and *Vc*DapE^T, where loop V is out of place compared to the WT-*Hi*DapE, we hypothesized that this region is important for catalysis. Both of the observed orientations and the greater flexibility of this loop (Figures 13B & 14) seem to be due to the lack of interactions with specific portions of the dimerization domain. Several interactions may be particularly critical. First, loop V in WT-*Hi*DapE is partially held in position by the anti-parallel beta strands (β7 and β12) and interactions with a loop connecting β7 with the dimerization domain. These contacts are missing in the truncated protein as portions of strands β7 and β12 have been transformed into a deletion-derived loop and α helix (Figure 13B). Loop V in WT-*Hi*DapE is also held in place by the loop from the dimerization domain (residues 223 to 228) (Figure 16). These contacts are also missing in the truncated protein.

Interestingly, the structure of WT-*Hi*DapE contains a sulfate ion located at the interface of the catalytic and dimerization domains and positioned very closely to loop V. The sulfate binding may have biological relevance and might indicate region where the *L,L*-diaminopimelic acid moiety of the substrates binds. Several residues from both domains interact with this sulfate ion. These include Arg178 (NE), Arg179 (NH), and Gly324 (amide NH; residue in loop V) from the catalytic domain and Arg258 (NH) from

the dimerization domain (corresponding to Arg179, Arg180, Gly325 and Arg259 in WT-*Vc*DapE) (Figure 16). This interaction is completely absent in the structure of the [ZnZn(*Vc*DapE^{T})] and residues Arg178 and Arg179 are part of the deletion-derived distorted α helix, whereas Gly214 (corresponding to Gly324 in WT-*Hi*DapE) located within loop V does not form any observable interactions (Figure 16).

Another indication that the specific orientation of loop V may be crucial for catalysis comes from MD simulations of the truncated DapE structures compared to WT-DapE and AAP (Figure 15). Consistent with the large crystallographic temperature factors, the greatest flexibility in the truncated forms of DapE is observed in the engineered loop created to replace the deleted dimerization domain and loop V, which directly overhangs the dinuclear active site (Figure 14C and D). For comparison, loop V in the apo-structure of *Nm*DapE (PDB entry 1vgy) is well ordered and positioned such that it allows two arginine residues (Arg179, Arg259 corresponding to the pairs Arg178/Arg258 and Arg179/Arg259 in *Hi*DapE and *Vc*DapE, respectively) to closely approach the active site. It is highly likely that these Arg residues, which are semi-conserved (Arg178) or conserved (Arg259) in DapEs, might interact with the carboxylate moieties of the substrate. Conserved Arg residues were shown to be essential to interact with substrate in human aminoacylase-1 (Acy1).[82] Interestingly in AAP, which exists as a monomeric protein of only the single catalytic domain, there is a loop residing directly over the dinuclear zinc active site that corresponds to loop V in DapE. This loop is very rigid, unlike loop V in DapE, and appears to be held in place by an internal disulfide

bridge formed between C223 and C227 (Figure 18). A decrease in dynamic flexibility due to changes in quaternary structure has been suggested for other protein.[83]

Apart from loop V, an additional loop might play an important role in the catalysis. Studies on Acy1, another dimeric member of the M20 family, showed that the dimerization domain contributes to the active site probably by interacting with the substrate.[82] Lindner *et al.*[82] showed that the alanine mutant of His206, which is located at the center of the loop, rendered the enzyme nearly inactive. An equivalent histidine residue is conserved in DapE enzymes (H194 in *Hi*DapE and H195 in *Vc*DapE), but it is disordered in the WT-*Hi*DapE structure.[63] Modeling of this disordered loop region (Figure 12A) positions H194 roughly ~13Å from the active site core, which is likely too far to interact with the substrate. However, it is possible that this loop can rearrange upon substrate binding as was reported for Acy1 and Sapep.[82, 84]

Evidence for such a loop movement can be gleaned from the structure of apo-*Nm*DapE where this loop is positioned within 8 Å of the active site. These data suggest that this His residue may also play an important role in DapE enzymes by interacting with the substrate. This hypothesis is consistent with DapEs structural design as the presence of the inter-domain clefts and connectors would allow for significant movement of this domain. Confirmation of the role of His194 in substrate recognition and binding must await a structure of DapE in complex with a substrate analog.

Figure 18. The role of the dimerization domain in the stabilization of loop V in WT-*Hi*DapE. (A). Superimposition of the WT-*Hi*DapE (gray) and *Vc*DapE^T (cyan) structures is shown. Loop V of WT-*Hi*DapE and *Vc*DapE^T is labeled as *Hi*LV and *Vc*LV, respectively. WT-*Hi*DapE residues interacting with the sulfate ion (stick model) are shown as gray lines. Corresponding residues in *Vc*DapE^T (except for R258 that is absent in the deletion mutant) are shown as yellow (R179 and R180) and orange (G214) lines.

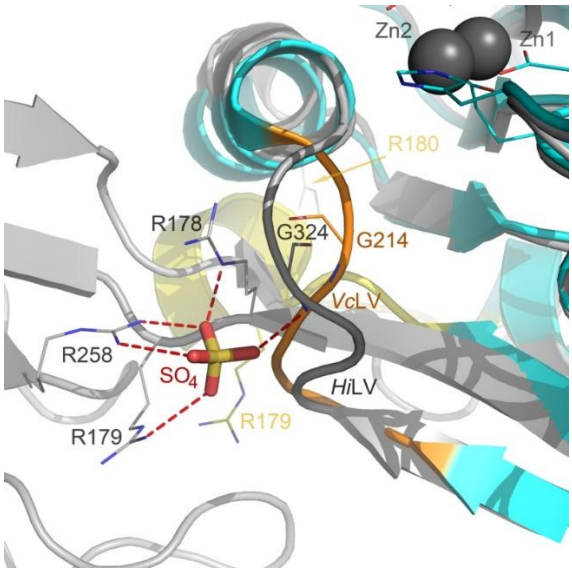

(B) Specific orientation of the active site loop V in *Vc*DapE^T and the corresponding loop in AAP. Overlay of the *Vc*DapE^T (cyan) and AAP (purple) structures is shown. The AAP loop and *Vc*DapE^T loop V are labeled as *Ap*LV and *Vc*LV, respectively. Stabilization of loop V in AAP by a disulfide bridge is indicated where Cys223 and Cys227 of AAP and the residues involved in zinc-binding in *Vc*DapE^T are shown as sticks. Zinc ions of *Vc*DapE^T are shown as black spheres. Zinc-bound ethylene glycol was omitted for clarity.

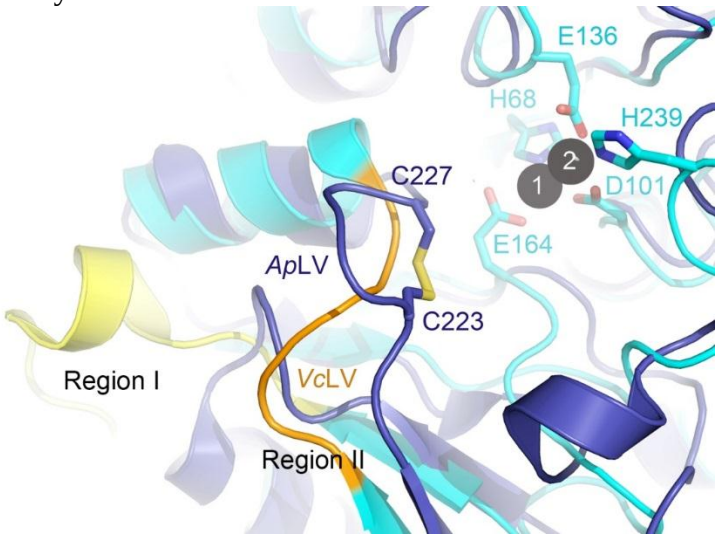

In conclusion, removal of the dimerization domain in DapE enzymes renders the enzyme inactive, even though the resulting truncated proteins have structures of the catalytic domain that are remarkably similar to WT-DapE and AAP. In fact, the dinculear Zn(II) site in the truncated DapE enzymes is nearly identical to those observed for AAP and WT-*Hi*DapE. Therefore, one would expect that the active site should be capable of catalyzing a hydrolytic reaction and yet no activity is detected. This suggests that positioning of the substrate in the active site is critical for the catalytic reaction to occur. Analysis of the structures *Hi*DapE^{T} and *Vc*DapE^{T} reveals that loop V is much more flexible in the truncated enzymes than WT-DapE due to the lack of interactions provided by the dimerization domain. These data suggest that the dimerization domain functions to restrict the conformational freedom of the loop V region and may contribute residues to the active site environment (H194, R179, R258, T325) that are important for substrate recognition, and binding. Designing small molecules inhibitors that interact with this active site loop V region as well as the dinuclear metal center, or disrupting dimer formation may lead to more potent DapE inhibitors that can function as antibacterial agents.

CHAPTER THREE

INHIBITION OF THE DAPE-ENCODED N-SUCCINYL-L,L-DIAMINOPIMELIC ACID DESUCCINYLASE FROM NEISSERIA MENINGITIDIS BY L-CAPTOPRIL

Introduction

The discovery of penicillin in 1929 was one of the greatest advances in therapeutic medicine considering the dramatic decrease in morbidity and mortality.[85] Unfortunately, conventional wisdom predicted that bacterial resistance to antibiotics was inevitable. The first strains of bacteria to develop resistance to penicillin were identified in 1940, less than 20 years after its discovery.[86] Bacteria have several means of developing resistance to antibiotics such as mutating existing genes (point mutations, deletions, inversions, insertions, etc.) or by acquiring new genes from other strains (horizontal gene transfer).[16] Therefore, the excessive and often unnecessary use of antibiotics in humans and animals accelerates the emergence of antibiotic resistant bacterial strains.[30] Since, nearly all newly developed antibiotics are simply structural variants of previously employed antimicrobial agents, many of them targeting the same enzymatic pathways, the risk of bacteria quickly developing resistance is very high.[4] In fact, several pathogenic bacteria, some of which were thought to have been eradicated, have made a significant resurgence due to bacterial resistance to antibiotics.[4, 44] According to the CDC, several bacterial strains currently exhibit multidrug resistance

with more than 60% of hospital acquired infections in the United States caused by the so-called ESKAPE pathogens (*Enterococcus faecium*, *Staphylococcus aureus*, *Klebsiella pneumoniae*, *Acinetobacter baumannii*, *Pseudomonas aeruginosa*, and *Enterobacter species*).[12]

To alleviate the problem of antibiotic resistance, it is urgent that new enzymatic targets in yet unexplored bacterial synthetic pathway be identified and specific inhibitors be developed.[87] The *meso*-diaminopimelate (*m*DAP)/lysine biosynthetic pathway offers several potential antibacterial enzyme targets, such as the *dapE*-encoded *N*-succinyl-l,l-diaminopimelic acid desuccinylase (DapE).[20, 23, 27] The products of this pathway, mDAP and lysine are essential components of the peptidoglycan cell wall for Gram-negative and most Gram-positive bacteria, providing a link between polysaccharide strands.[2, 20, 29] DapE genes have been identified in a large number of pathogenic Gram-positive and Gram-negative bacteria including all of the ESKAPE pathogens and sequence alignment of these DapE genes reveals a minimum of 49% identity.[32, 37, 42, 55b, 64a, 88] Deletion of the gene encoding for DapE is lethal to *Helicobacter pylori* and *Mycobacterium smegmatis* *e*ven in the presence of lysine supplemented media.[55] Therefore, DapEs appear to be essential for bacterial cell growth and as there are no similar biosynthetic pathways in mammals, DapEs are potential targets for inhibitors that may possess antimicrobial activity.[27]

DapEs are metalloenzymes that catalyzes the hydrolysis of *N*-succinyl-L,L-diaminopimelic acid (SDAP), forming L,L-diaminopimelic acid and succinate.[29] DapEs have been purified from multiple sources but the best characterized enzyme is the DapE

from *Haemophilus influenzae* (*Hi*DapE), which is a homodimeric enzyme (subunit Mr = 41.6 kDa) and requires two Zn(II) ions per mole of polypeptide for full enzymatic activity.[32] The X-ray crystal structures for both the mono and dinuclear Zn(II) forms of *Hi*DapE have been reported.[63] In the dinuclear Zn(II) form, each Zn(II) ion adopts a distorted tetrahedral geometry coordinated by one imidazole (H67 for Zn1 and H349 for Zn2) and one carboxylate group (E163 for Zn1 and E135 for Zn2). Both Zn(II) ions are bridged by an additional carboxylate groups (D100) and a water/hydroxide, forming a (μ-aquo)(μ-carboxylato)dizinc(II) core with a 3.3 Å Zn-Zn distance.[37] To date, few inhibitors of DapE enzymes have been reported and no X-ray structural data exists for a DapE enzyme in the presence of any inhibitor.

The design of highly specific, tight binding inhibitors of DapE enzymes hinges on the potential inhibitor's ability to bind to the metal ions in the active site. L-captopril, an angiotensin-converting enzyme (ACE) inhibitor, was shown to be a potent inhibitor of *Hi*DapE, (IC_{50} of 3.3 μM and a measured K_i of 1.8 μM) and showed a dose-responsive antibiotic activity towards *E. coli*.[42] Several factors are important for L-captopril interactions with the active site metal ions of DapE, some of which are metal coordination geometry, the open metal coordination sites (*i.e*. those filled by a water/hydroxide molecules), and the number of active site metal ions. Therefore, we have analyzed the binding of L-captopril to DapE using both spectroscopic and X-ray crystallographic evidence. These data provide insight into L-captopril binding to the active site metal ions as well as adjacent amino acid residues, affording new information towards the rational design of new, more potent DapE inhibitors.

Materials and Methods

Materials. D,L-α,ε-Diaminopimelic acid (98% pure), succinic anhydride and ion exchange resin (Dowex 50WX8−200,H^+ form) were purchased from Sigma. 2-Naphthalenesulfonic acid 1-hydrate (98%) was purchased from TCI Microcrystalline cellulose was purchased from Merck. All other chemicals used in this study were purchased from commercial sources and were of the highest quality available. SDAP was synthesized using the procedure described by Lin *et al.* [59] providing an overall yield of 41%.

Cloning, expression and purification of DapE. The *Hi*DapE enzyme was expressed and purified as described previously.[89] The DapE gene from *Neisseria meningitidis* (*Nm*DapE) was cloned into the pMCSG7 vector using the Ligation Independent Cloning method.[90] The primers used were: 5'- TAC TTC CAA TCC AAT GCC GCA GCT GCA GCT GCA AAA GAA AAA GTG GTT TCG TTG GCA CAA G - 3'and 5'- TTA TCC ACT TCC AAT GTT AGT TAG CTA TCC AAT AAA TTC ACT AAC ATT TTG TG-3'. The PCR product was purified using the QIAquick PCR Purification Kit (Qiagen) to remove the primers and dNTPs from the PCR reaction. T4 polymerase was employed to create overhangs on the PCR fragments. The resulting plasmid was transformed into BL21(DE3)/magic *E. coli* competent cells and grown in Luria-Bertani Broth (LB) media containing ampicillin (150 μg mL^{-1}) and kanamycin (25 μg mL^{-1}) at 37 ˚C to an A_{600} of 0.7 with shaking. IPTG was added (0.4 mM) and culture growth was continued for 16 h at 18 ˚C. Cells were recovered by centrifugation (12,000g) for 15 min. at 4 ˚C using a Beckman Coulter Avanti J-E Centrifuge. *Nm*DapE

was purified according to the standard protocol for Ni-NTA affinity chromatography and all steps were performed at 4 ˚C.[91] The His6-tag was removed by treating each enzyme with His6-tagged TEV protease for 16 h at 4 ˚C in 50 mM HEPES, pH 8.0. Cleaved protein was separated from His6-tagged TEV using Ni-NTA affinity chromatography.

Enzymatic Assay. The specific activity of *Hi*DapE and *Nm*DapE was determined using a 50/50 mixture of D,D and L,L-SDAP as the substrate in 50 mM Phosphate buffer (PPi), pH 7.5 as previously described.[67b] The kinetic parameters V_{max} and K_m were determined by quantifying the amide bond cleavage (decrease in absorbance) of L,L-SDAP at 225 nm ($\varepsilon = 698\ M^{-1}\ cm^{-1}$) in triplicate. Enzyme activities are expressed as units/mg where one unit is defined as the amount of enzyme that releases 1 μmol of L,L-SDAP at 30 ˚C in 1 min. Catalytic activities were determined with an error of ± 10 %. Initial rates were fit directly to the Michaelis-Menten equation to obtain the catalytic constants K_m and k_{cat} using Origin software.

Inhibition of NmDapE by L-captopril. The kinetic parameters v (velocity), k_{cat} ($V_{max}/[E]_0$), K_m (Michaelis constant), and K_i (inhibition constant) were determined in 50 mM PPi at pH 7.5 spectrophotometrically by recording the initial velocity of the hydrolysis of L,L-SDAP at 25 ^oC in triplicate.[92] L-captopril concentrations ranged from 0 to 0.1 mM. The linearity of the progress curves for product formation both in the absence and presence of inhibitor indicated that L-captopril is in rapid equilibrium with *Nm*DapE. The initial rates were plotted against substrate concentration and the kinetic constants were calculated using Origin software.[59, 67]

Co(II)-Substituted DapE samples. Apo-DapE was prepared by extensive dialysis for 72 h at 4 ˚C against 10 mM EDTA in 50 mM HEPES buffer, pH 7.5. DapE was then exhaustively dialyzed against metal-free (Chelex-100 treated) 50 mM HEPES buffer, pH 7.5. Any remaining metal ions were estimated by comparing the activity of the apo-enzyme with a sample that had been reconstituted with Zn(II). DapE incubated with EDTA typically had less than 5% residual activity after dialysis. The mono and dicobalt(II)-forms of *Hi*DapE and *Nm*DapE were prepared using apo-DapE samples that were incubated with $CoCl_2$ (99.999%; Strem Chemicals, Newburyport, MA) for 30 minutes at 25 ˚C prior to exhaustive dialysis into Chelex-100 treated buffer as previously reported.[93]

UV-Visible Measurements. Electronic absorption spectra were recorded on a Shimadzu UV-2450 spectrophotometer equipped with a temperature controller (25 ˚C). A protein concentration of 1.5 mM in 50 mM HEPES buffer, pH 7.5 was used to obtain each spectrum. The electronic absorption spectra of [Co_(*Hi*DapE)], [CoCo(*Hi*DapE)], [Co_(*Nm*DapE)], and [CoCo(*Nm*DapE)] were recorded in both the absence and presence of L-captopril, and the absorption due to apo-enzyme was subtracted.

EXAFS Spectroscopy. EXAFS spectra of a 1 mM sample of [ZnZn(*Hi*DapE)] frozen in polycarbonate cuvets (24 x 3 x 1 mm) with a 0.025 mm Mylar window covering face, were collected at the Stanford Synchrotron Radiation Laboratory (SSRL) on beamline 7-3. The SPEAR storage ring operated in a dedicated mode at 3.0 GeV. The Si[220] crystal monochromator was detuned to 50% maximum reflectivity for harmonic rejection. On beamline 9-3, a focusing mirror provided harmonic rejection. The edge

regions, for multiple scans obtained on the same sample, were compared to ensure that the sample was not damaged by exposure to X-ray radiation. EXAFS analysis was performed using EXAFSPAK software according to standard procedures, using E0 = 9670 eV for k-scale definition.

Electron Paramagnetic Resonance Spectroscopy. Electron paramagnetic resonance (EPR) spectra were recorded at 4.5 - 35 K, 9.63 GHz (ER4116DM resonator with $\mathbf{B}_0 \perp \mathbf{B}_1$), 9.37 GHz (ER4116DM resonator with $\mathbf{B}_0 \| \mathbf{B}_1$), or 9.39 GHz (SHQ resonator) using 1.2 mT (12 G) magnetic field modulation at 100 kHz with phase-sensitive detection on a Bruker EleXsys E600 spectrometer equipped with an Oxford Instruments ESR900 helium flow cryostat and ITC503 temperature controller. The SHQ resonator has a significantly higher $\mathbf{B}_1$ for a given microwave power than the ER4116DM resonator (we estimate by a factor of about 5). Background signals were collected on samples of frozen buffer and subtracted.

Magnetic Circular Dichroism Studies. The Magnetic circular dichroism (MCD) instrument consists of a JASCO J815 spectropolarimeter and an Oxford Instruments SM4000 cryostat/magnet. Variable-temperature variable-field (VTVH) MCD data were collected at increments of 0.5 Tesla (T) from 0 to 7.0 T and at temperatures (nominally) of 1.5, 3.0, 6.0, 12, 24 and 48 K. Spectra were collected at 1.0 nm band width and were scanned at 50 nm/min using a one second time constant. The sample cell has a 0.62 cm path length. Each spectrum was corrected for any natural CD by subtracting the zero-field spectrum of the sample. Even when there is no sample present the instrument the baseline exhibits a small deviation from zero that is both field- and wavelength-

dependent. Therefore, each spectrum was also corrected by subtraction of a spectrum recorded at the same magnetic field but with no sample present. The MCD spectra were fit to the minimum number of Gaussian peaks using GramsAI 9.1 software after converting the spectra to wavenumber units. In the fitting process, a minimum number of Gaussians were fit to achieve a satisfactory composite spectrum. Fitting of the VTVH MCD data was achieved using a Fortran program, VTVH 2.1.1, written by Mark Riley.[94] The spin Hamiltonian and additional details of the fitting program have been described previously.[95] The fits were tested for robustness once a complete set of parameters had been obtained. To do this, the initial parameters were set to the best fit parameters and then all allowed to float. Subsequently, one key parameter such as J, D, M_{xy}, M_{xz}, M_{yz} was chosen and its initial value was set differently after which the fit process was repeated. Percent polarization for a given fit was calculated from M_{xy}, M_{yz} and M_{xz} using $\%M_x = (M_{xy} \bullet M_{yz})^2/[(M_{xy} \bullet M_{xz})^2+(M_{xy} \bullet M_{yz})^2+(M_{xz} \bullet M_{yz})^2]$. M_y and M_z were calculated correspondingly.[96] Finally, the VTVH MCD data fitting program used a spin Hamiltonian that included the term $H = -2J S_1 S_2$.

Protein Crystallization. Prior to crystallization, a 25 mg/ml *Nm*DapE protein sample was incubated with 3 eq. of Zn^{2+} ions and left on ice for 20 minutes to equilibrate. Zinc-loaded *Nm*DapE was screened against three hundred commercially available conditions (Index HT and PEG/Ion HT from Hampton Research and Wizard TM from Emerald Biosystems) using a Mosquito liquid handling robot with 96 plates.[97] Several crystallization conditions were characterized yielding diffraction quality crystals. All crystals were screened and data were collected on the best diffracting crystals, which

were grown by the sitting-drop vapor-diffusion method at 16 ˚C using 400 nl of a precipitant solution (20% (w/v) PEG 3350, 100 mM HEPES pH 7.5) and 400 nl of [ZnZn(*Nm*DapE)]. X-ray quality crystals appeared within 2 weeks. Crystals of [Zn_*Nm*DapE] were also crystallized by the sitting-drop vapor-diffusion method at 16 ˚C but with a 400 nl precipitant solution (15% (w/v) PEG 3350 100 mM Succinic acid pH 7.0) and 400 nl of a protein providing crystals within 2 weeks. Crystals of [ZnZn(*Nm*DapE)] in complex with L-captopril were obtained by mixing 400 nl of a precipitant solution (0.2 M ammonium acetate, 0.1 M TRIS pH 8.5, 25% (w/v) and polyethylene glycol 3350 in a 1:1 ratio with a solution of [ZnZn(*Nm*DapE)] incubated with a 20 mM solution of L-captopril (50 mM HEPES pH 7.5, 150 mM NaCl) with crystals appearing within 3 weeks.

Structure Solutions and Refinement. The X-ray data were collected at the 19-ID beamline of the Structural Biology Center at the Advanced Photon Source.[37] All data were processed and scaled using HKL3000. All structures described in this manuscript were determined by the molecular replacement method and refined by slight variation of the same protocol. Molecular replacement searches were completed with the program MOLREP within the CCP4 suite using the apo-crystal structure of *Nm*DapE as a template (PDB id 1vgy).[37] The asymmetric unit of [Zn_(*Nm*DapE)] (space group $P2_12_12_1$) contains a dimer, while crystals of [ZnZn(*Nm*DapE)] and [ZnZn(*Nm*DapE)] in complex with captopril both crystallized in the $C222_1$ space group and contained only one subunit of the dimer. Several rounds of rebuilding and readjusting using COOT [98] and refinement using programs REFMAC [99] and PHENIX [68] were required to improve the

initial models. The final models were refined against all reflections using the program in the resolution ranges except for 5% of the reflections, which were randomly selected and used to monitor R_{free}. The final refinement statistics are presented in Table 4. Analysis and validation of all structures were performed with the aid of PROCHECK[100] and MOLPROBITY.[101] The refinement restraints for the L-Captopril structure were created with the assistance of the program Coot and were generated from SMILE[102] string.

PDB coordinates. The atomic coordinates for [Zn_(*Nm*DapE)], [ZnZn(*Nm*DapE)] and [ZnZn(*Nm*DapE)] bound by L-captopril were deposited in the PDB with id (4O23, 4PPZ and 4PQA), respectively.

Table 4. Data and Refinement Statistics for [Zn_*Nm*DapE], [ZnZn_*Nm*DapE] and [ZnZn_*Nm*DapE]-L-captopril.

Data collection statistics	[Zn_*Nm*DapE]	[ZnZn_*Nm*DapE]	[ZnZn_*Nm*DapE]-L-captopril
Space group	$P2_12_12_1$	$C222_1$	$C222_1$
Unit cell (Å)	a = 55.3 b =111.4, c = 132.5	a = 117, b =151.6 c = 55.5	a = 116.9, b =151.5 c = 55.1
Resolution (Å)	39.2-2.09	29.4-2.0	27.5-1.78
Wavelength (Å)	0.98 Å	0.98	0.98
Number of observed reflections	204709	202836	178375
Number of unique reflections	48738	33502	46112
Redundancy [b]	4.2(4.0)	6.1(5.8)	3.9(3.8)
R_{merge} [a,b] (%) R_{pim} [a,b] (%)	7.4 (82.1) 4.0 (45.7)	8.5 (89.9) 4.3 (59.4)	6.5 (75.2) 3.3(44.2)
Completeness[b] (%)	99.1 (96.7)	100 (100)	97.7 (99.5)
I/σ	17.9(1.5)	22.8(1.9)	17.7(1.7)
Phasing			
phasing method	**MR**	**MR**	**MR**
Refinement statistics			
R_{cryst} (%)	21.3	17.5	16.4
R_{free} (%)	24.1	20.8	19.6
protein residues	746	374	374
zinc/phosphate/sulfates ions	3/-/4	2/1/-	2/-/1
solvent	380	237	284
Rmsd from target values			
bond lengths (Å)	0.003	0.020	0.021
bond angles (deg)	0.71	1.69	1.90
Average *B* factors (Å^2)			
protein	43.8	32.2	24.8
Zn	32.0	23.2	17.9
H_2O	37.8	24.19	34.6
PDB ID	4O23	4PPZ	4PQA
Ramachandran (%)[c] M.F./A.A.	97.4/2.6	97.6/2/4	97.9/2.1

[a] $R_{merge} = \Sigma_{hkl}\Sigma_i|Ii_{(}hkl_{)} - \langle I_{hkl}\rangle |/\Sigma_{hkl}\Sigma_i I_{i(hkl)}$, where $Ii_{(}hkl_{)}$ is the *i*th observation of reflection *hkl*, and $\langle I_{hkl}\rangle$ is the weighted average intensity for all observations *i* of reflection *hkl*. and $R_{pim} = \Sigma_{hkl}(1/(N-1)^{1/2})\Sigma_i|Ii_{(}hkl_{)} - \overline{Ihkl}|/\Sigma_{hkl}\Sigma_i I_{i(hkl)}$.

[b] Numbers in parentheses are values for the highest-resolution bin.

[c] As defined by MOLPROBITY (M.F.-the most favored/ A.A additionally allowed)

Results

Kinetic studies on [Zn_(NmDapE)] and [ZnZn(NmDapE)]. The kinetic parameters for the [Zn_(*Nm*DapE)] and [ZnZn(*Nm*DapE)] were determined by monitoring the hydrolysis of L,L-SDAP, at pH 7.5 and 25 ^{o}C. For [Zn_(*Nm*DapE)], a k_{cat} value of 76 ± 10 s^{-1} and a K_m value of 795 ± 20 μM was obtained. On the other hand, [ZnZn(*Nm*DapE)] exhibited a k_{cat} of 120 ± 10 s^{-1} and a K_m of 610 ± 11μM. For [Zn_(*Hi*DapE)] and [ZnZn(*Hi*DapE)], k_{cat} values of 80 ± 5 s^{-1} and 140 ± 10 s^{-1} were obtained, respectively, with corresponding K_m values of 730 ± 15 μM for both enzymes (Table 5). Inhibition of *Nm*DapE by L-captopril was examined by monitoring the initial rates of hydrolysis of L,L-SDAP as a function of L-captopril concentration in triplicate. The double-reciprocal plot of velocity vs. L-captopril shows a pattern characteristic of competitive inhibition. The experimental data were fit to the Michaelis-Menten equation for competitive inhibition reported by Cleland.[103] The inhibition constant, K_i, for the binfing of L-captopril to *Nm*DapE was found to be 2.4 ± 0.1 μM in good agreement with the Ki value obtained for L-captopril inhibition of *Hi*DapE of 1.8 μM.[92]

Electronic Absorption Spectroscopy. Electronic absorption spectra were obtained for [Co_(*Hi*DapE)], [CoCo(*Hi*DapE)], [Co_(*Nm*DapE)], [CoCo(*Nm*DapE)] in both the

Table 5. Kinetic constants for the [Zn_(DapE)] and [ZnZn(DapE)] from *N. meningitidis* and *H. Influenzae*.

	***Nm*DapE**		***Hi*DapE**	
Kinetic constants	Zn	ZnZn	Zn	ZnZn
K_m (μM)	795 ± 20	610 ± 11	730 ± 15	730 ± 15
k_{cat} (s^{-1})	76 ± 10	120 ± 10	80 ± 5	140 ± 10
k_{cat}/K_m ($mM^{-1}min^{-1}$)	5,700 ± 200	11,800 ± 200	6,600 ± 200	11,400 ± 200

absence and presence of L-captopril, since the position and molar absorptivities of the Co^{2+} d-d bands reflect the coordination number and geometry of the metal ions.[104] The absorption due to apo-DapE was subtracted in all cases. The spectra of [Co_(*Nm*DapE)] and [CoCo(*Nm*DapE)] recorded in the absence of L-captopril are identical to those previously reported for [Co_(*Hi*DapE)] and [CoCo(*Hi*DapE)] (Figure 19A & B).[67b] For [Co_(*Nm*DapE)] two resolvable d-d transitions are observed with λ_{max} values of 560 nm (ε ~40 $M^{-1}cm^{-1}$) and a shoulder at 520 nm (ε ~30 $M^{-1}cm^{-1}$) while [CoCo(*Nm*DapE)] also exhibited an absorbance bands at 560 nm (ε ~130 $M^{-1}cm^{-1}$) and 520 nm (ε ~120 $M^{-1}cm^{-1}$). Upon the addition of 5 eq. of L-captopril to [Co_(*Nm*DapE)] the d-d band at 560 nm slightly red-shifted with little or no change in the molar absorptivity (Figure 19 A). However, when 5 eq. of L-captopril was added to [CoCo(*Nm*DapE)], the λ_{max} red-shifts to 590 nm while molar absorptivity increases from ~130 to 250 $M^{-1}cm^{-1}$ (Figure 19A). Similar spectra were recorded for [Co_(*Hi*DapE)] and [CoCo(*Hi*DapE)] (Figure 19B). The UV-Vis spectrum of [CoCo(*Hi*DapE)] in the presence of L-captopril was also recorded from 250 to 400 nm; however, the characteristic $S \rightarrow Co^{2+}$ ligand-to-metal charge-transfer (LMCT) band, which would be expected to exhibit a molar absorptivity of ~1000 $M^{-1}cm^{-1}$, was not observed due to strong protein absorption.[104]

Figure 19. Electronic Absorption Spectra: (A) a 1.5 mM solution of [Co_(*Nm*DapE)] in 50 mM HEPES buffer, pH 7.5 in the absence (black) and presence (blue) of 5 eq. of L-captopril and a 1.5 mM solution of [CoCo(*Nm*DapE)] in the absence (red) and presence (green) of 5 eq. of L-captopril in 50 mM HEPES buffer pH 7.5.

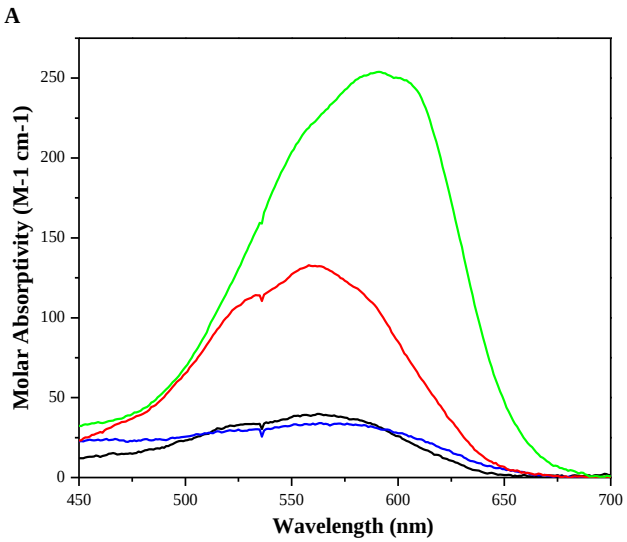

(B) a 1.5 mM solution of [Co_(*Hi*DapE)] in the absence (black) and presence (blue) of 5 eq. of L-captopril in 50 mM HEPES buffer at pH 7.5 and a 1.5 mM solution of [CoCo(*Hi*DapE)] in 50 mM HEPES buffer at pH 7.5 in the absence (red) and presence (green) of 5 eq. of L-captopril. The electronic absorption spectrum of apo enzyme was subtracted in each case.

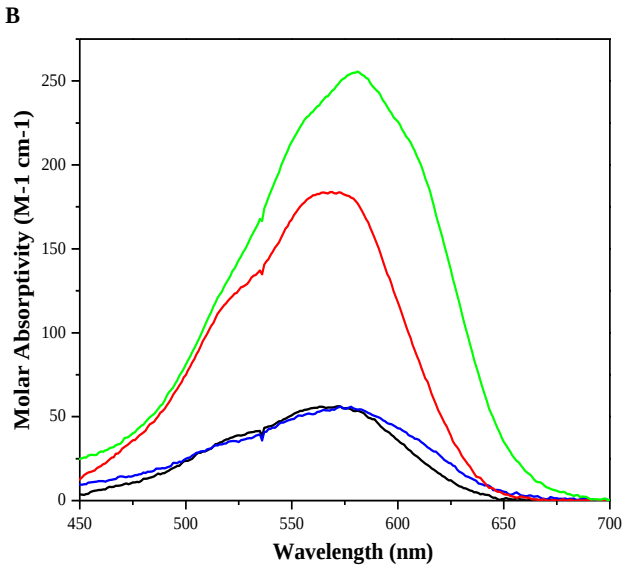

EPR spectra of L-captopril bound to [Co_(NmDapE)], [CoCo(NmDapE)], [Co_(HiDapE)], and [CoCo(HiDapE)]. EPR spectra of the resting forms of Co^{2+}-substituted *Nm*DapE (Figure 20A) and *Hi*DapE (Figure 20B) show distinct similarities. At 13 K and non-saturating microwave power, the [Co_(*Nm*DapE)] spectra are complex and appear due to a moderately rhombic (E/D ≤ 0.15) $M_S = \pm {}^1/_2$ signal with resonances at g' = 5.35 (1250 G), 4.05 (1660 G) and 2.25 (3015 G), superimposed on an $M_S = \pm {}^3/_2$ signal with a sharp resonance at g' = 6.5 (1030 G) and a broad derivative feature with an estimated turning point at g' ≈ 1.15. At 4.5 K and high microwave power, the $M_S \pm {}^1/_2$ signals are almost completely extinguished. This latter behavior indicates that the $M_S = \pm {}^1/_2$ signals are due to thermal population of the $M_S = \pm {}^1/_2$ Kramers' doublet at the higher temperature and is due to an excited state with a zero-field splitting,Δ, on the order of 10 cm^{-1} for [Co_(*Nm*DapE)], and less for [Co_(*Hi*DapE)] where some $M_S = \pm {}^1/_2$ contribution is still evident at 4.5 K (1 cm^{-1} corresponds to 1.44 K). If the $M_S = \pm {}^1/_2$ signals were ground state signals due to a distinct chemical species, rapid-passage signals would be expected to be observed rather than disappearance or diminution of the signals.[105] The data indicate, therefore, a preferred binding site with an $M_S = \pm {}^3/_2$ ground state, suggesting a distorted tetrahedral coordination environment.[105] Upon adding a second equivalent of Co^{2+}, a poorly resolved and apparently $M_S = \pm {}^1/_2$ signal is observed at 13 K. In addition, a very weak but clearly identifiable ^{59}Co hyperfine pattern with A_z = 90 G was observed on the low field edge of the $M_S = \pm {}^1/_2$ signal, centered at g' = 7.9 (850 G; see e.g. Figure 20A, trace C), that could be due to a small amount of an

Figure 20. EPR spectra at 9.39 GHz (SHQ resonator) of: (A) [Co_(*Nm*DapE)] (A, B) and [CoCo(*Nm*DapE)] (C, D), recorded at 13 K, 0.5 mW (A, C) and 4.5 K, 100 mW (B, D). Spectral amplitudes are shown normalized for $1/T$, $\sqrt{P_{microwave}}$, and eq. of Co^{2+} added. (B) of [Co_(*Hi*DapE)] (A, B) and [CoCo(*Hi*DapE)] (C, D), recorded at 13 K, 1.0 mW (A, C) and 4.5 K, 200 mW (B, D). Spectral amplitudes are shown normalized for $1/T$, $\sqrt{P_{microwave}}$, and eq. of Co^{2+} added.

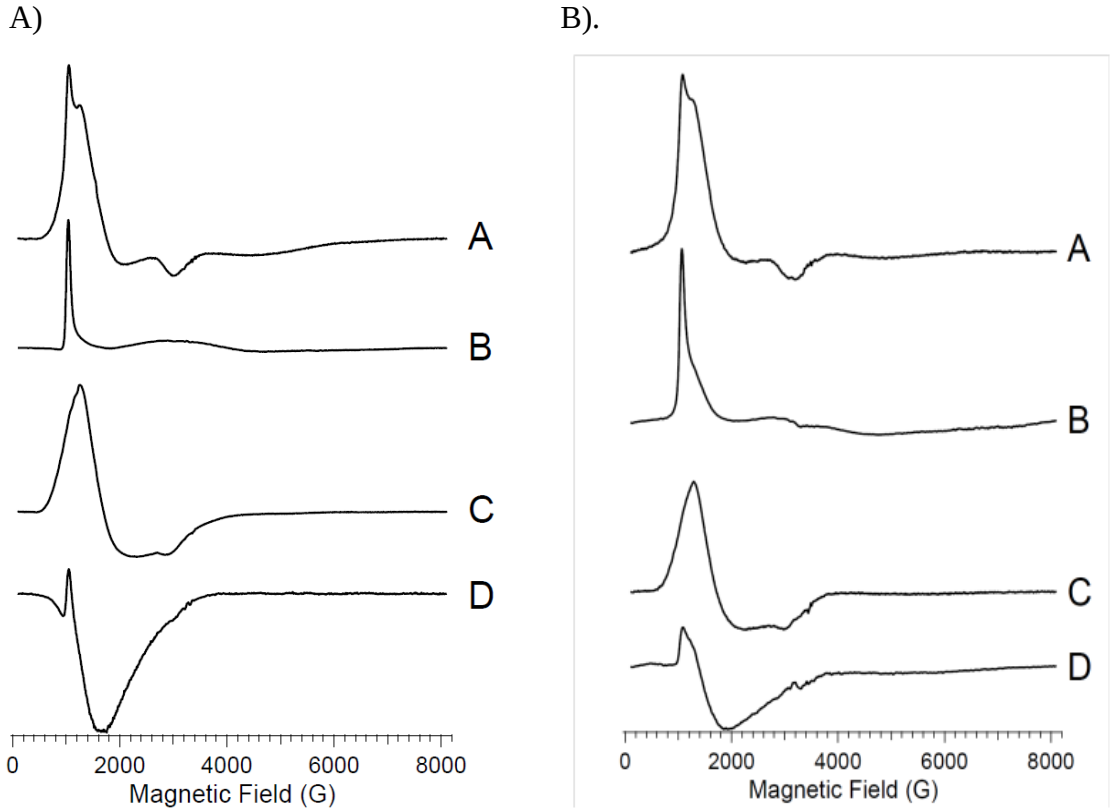

additional $M_S = \pm {}^3/_2$ signal with $g_{real(z)} \sim 2.6$ or else a very rhombic ($E/D \sim {}^1/_3$) $M_S = \pm {}^1/_2$ signal with $g_{real(y)} \sim 2.9$; the origin of the hyperfine-split signal is unclear but it was completely insensitive to captopril and is not considered further.

In contrast to [Co_(*Nm*DapE)] and [Co_(*Hi*DapE)], when EPR spectra of [CoCo(*Nm*DapE)] and [CoCo(*Hi*DapE)]were recorded at 4.5 K, the predominant $M_S = \pm$

$^1/_2$ signal was clearly still observable as a rapid-passage signal that appears as an inverted absorption-shaped feature, superimposed on the sharp $M_S = \pm {}^3/_2$ signal at g' = 6.5. The appearance of a slow-relaxing ground-state $M_S = \pm {}^1/_2$ signal is consistent with the second added eq. of Co^{2+} occupying a five- or six-coordinate site. There is a slight difference between the signals from [CoCo(*Nm*DapE)] and [CoCo(*Hi*DapE)]. The signal from [CoCo(*Nm*DapE)] appears to account for the entire cobalt complement, whereas that from [CoCo(*Hi*DapE)] indicates that some EPR silent Co^{2+} is present. Further, the $M_S = \pm {}^3/_2$ signal in [CoCo(*Hi*DapE)] is specifically and significantly smaller than in [Co_(*Hi*DapE)], whereas this is not the case in [CoCo(*Nm*DapE)]. These data suggest weak antiferromagnetic interaction between the Co^{2+} ions in [CoCo(*Hi*DapE)], such that $|J| > h\nu$ for some, but not all, of the population of dinuclear centers in the sample, *i.e*. that there is a distribution of J that includes 0.3 cm^{-1}. No parallel mode ($\mathbf{B}_0 \| \mathbf{B}_1$) EPR signals were observed.

L-captopril addition was found to induce differential effects in [CoCo(*Nm*DapE)] and [CoCo(*Hi*DapE)]. Upon adding L-captopril to [CoCo(*Nm*DapE)], the sharp $M_S = \pm {}^3/_2$ signal at $g' = 6.5$ is essentially extinguished but no overall signal intensity is lost (Figure 21, traces A & B). This is consistent additional coordination of the hitherto four-coordinate Co^{2+} ion but no mediation of significant (≥ 0.3 cm^{-1}) exchange coupling between the two Co^{2+} ions. In contrast, the addition of L-captopril to [CoCo(*Hi*DapE)] leads to a wholesale loss of about 30 % of the EPR intensity, with no detectable change in line shape (Figure 21, traces C & D), signifying an increase, albeit modest, in the exchange coupling between the two Co^{2+} ions.

Figure 21. EPR spectra at 9.63 GHz (ER4116DM resonator) of [CoCo(*Nm*DapE)] before (A) and after (B) the addition of L-captopril; and [CoCo(*Hi*DapE)] before (C) and after (D) addition of L-captopril. Spectra were recorded at 4.5 K, 100 mW. Spectral amplitudes are shown normalized for 1/*T*, $\sqrt{P_{microwave}}$, and eq. of Co^{2+} added.

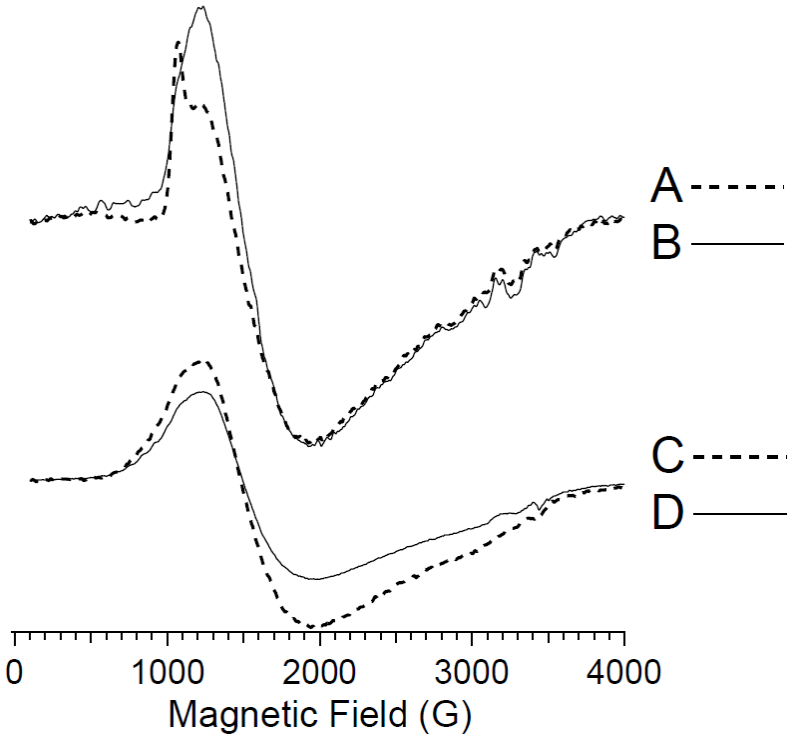

MCD spectra of L-captopril bound to [Co_(NmDapE)], [CoCo(NmDapE)], [Co_(HiDapE)], and [CoCo(HiDapE)]. MCD spectra of [CoCo(*Nm*DapE)] and [CoCo(*Hi*DapE)] are nearly identical in shape, band energies, and intensities (Figure 22). It should be noted that the MCD spectra at room temperature in pure buffer (no glycerol glassing agent) have the same bands as the low temperature spectra; however, they are much less intense and broader. All of the bands are temperature–dependent C-terms arising from the paramagnetic high-spin Co^{2+} ground states. The intense negative band at 576 nm is asymmetric due to a small component at 559 nm in [CoCo(*Hi*DapE)] and at

558 nm in [CoCo(*Nm*DapE)]. This intense negative band along with an intense positive band at 532 nm are characteristic of high-spin Co^{2+} in a four-coordinate, distorted tetrahedral ligand field.[106] These bands arise from the $^4A_2 \rightarrow {}^4T_1(P)$ d-d transition in T_d that have been split into three components by the lower symmetry environment in the active site. The negative band at 503 nm along with a very weak positive band at shorter wavelength are characteristic of high-spin Co^{2+} in a six-coordinate, distorted octahedral ligand field.[106a, b, 107] The band at 503 nm arises from the $^4T_{1g} \rightarrow {}^4T_{1g}(P)$ d-d transition in

Figure 22. MCD spectra of : (A) [CoCo(*Hi*DapE)] (top) and [CoCo(*Nm*DapE)] (bottom) and (B) [CoCo(*Hi*DapE)] + 5 eq. of L-captopril (top) and [CoCo(*Nm*DapE)] + 5 eq. of L-captopril (bottom). All spectra were recorded at 1.3 K and 7.0 T in a 0.62 cm path length cell. The enzymes were in a solution of 60/40 (v/v) glycerol/buffer. [CoCo(*Hi*DapE)] was 32 mg/mL (0.77 mM enzyme, 1.6 mM in active sites, 3.1 mM in Co^{2+}). [CoCo(*Nm*DapE)] was 29 mg/mL (0.70 mM enzyme, 1.4 mM in active sites, 2.8 mM in Co^{2+}). The units of $\Delta\varepsilon/H$ are $M^{-1}cm^{-1}T^{-1}$, where the concentration of actives sites was used. In both figures the blue trace is the experimental spectrum and the red traces are the Gaussians used to fit the spectra.

A)

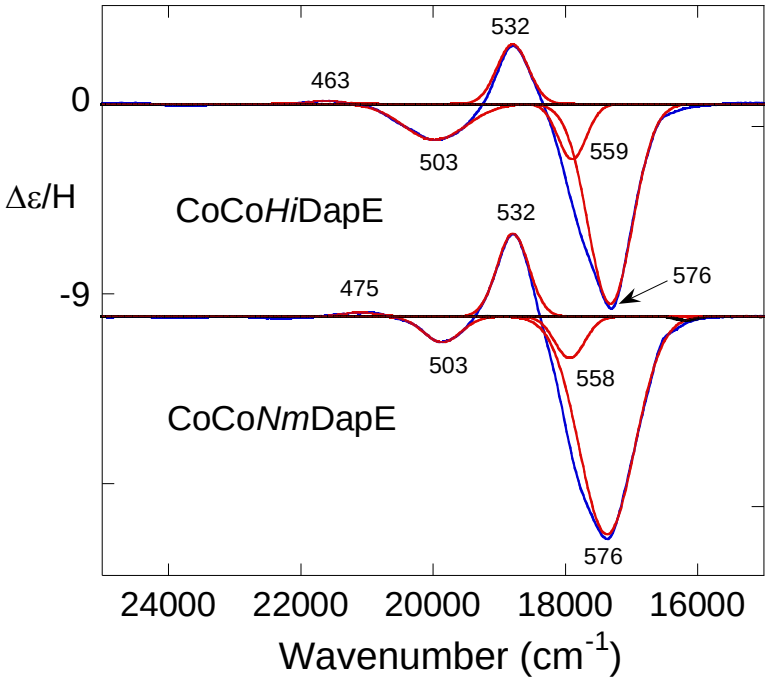

B)

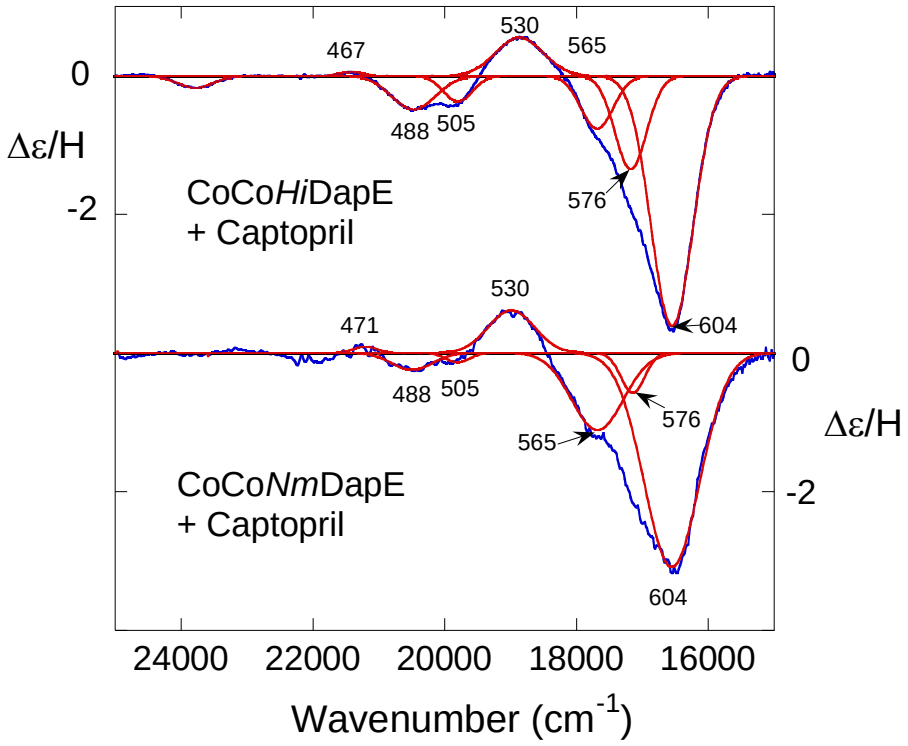

O_h that can broaden or split in lower symmetries. The 503 nm band does not split in [CoCo(*Nm*DapE)] or [CoCo(*Hi*DapE)] but is noticeably broader in [CoCo(*Hi*DapE)] than in [CoCo(*Nm*DapE)]. The very weak positive bands at 463 and 475 nm in [CoCo(*Hi*DapE)] and [CoCo(*Nm*DapE)], respectively, are doublet transitions, which gain intensity through spin-orbit coupling to the nearby spin-allowed 503 nm band.[107a] Despite the similarity in the MCD spectra of [CoCo(*Hi*DapE)] and [CoCo(*Nm*DapE)], there is a difference in the relative metal binding affinities between the two enzymes. When 1 eq. of Co^{2+} is added to apo-*Nm*DapE, both the six-coordinate and four-coordinate sites are partially occupied. Addition of a second eq. of Co^{2+} saturates both binding sites. On the other hand, addition of 1 eq. of Co^{2+} to apo-*Hi*DapE saturates the four-coordinate site leaving the six-coordinate site virtually empty.

VTVH MCD data were collected at 503, 532 and 576 nm on both [CoCo(*Nm*DapE)] and [CoCo(*Hi*DapE)]. The data were used to construct magnetization plots. The VTVH MCD were fitted as previously described [88a, 94], which yield the electronic ground state parameters for magnetic exchange coupling (*J*), axial (*D*) and rhombic (*E*) zero-field splitting (ZFS). Multiple experiments were run and average values of these parameters along with the standard deviations are given in Table 6. Magnetic exchange coupling, if it occurs, will be strongest through the monoatomic bridges (*e.g.* μ-1,1 as opposed to μ-1,3). In none of the fittings of the VTVH data from [CoCo(*Nm*DapE)] or [CoCo(*Hi*DapE)] was the quality of fit improved (lower value of χ^2) by having a non-zero *J* (positive or negative). This strongly suggests that the bridging oxygen atom is in the form of a μ-aqua as opposed to a μ-hydroxo. Many dicobalt(II) complexes with either a μ-aqua or μ-hydroxo have been studied.[29, 108] Aqua bridged complexes consistently exhibit a small antiferromagnetic coupling (negative *J*) or no coupling at all; whereas, hydroxo-bridged complexes consistently have a small ferromagnetic (positive *J*) coupling. The ZFS parameters that were determined in the fitting of the VTVH data from [CoCo(*Nm*DapE)] and [CoCo(*Hi*DapE)] were also consistent with assignment of the 503 nm band to a six-coordinate Co^{2+}, and the 532 and 576 nm bands to a four-coordinate Co^{2+}. Generally the axial ZFS parameter, *D*, is greater than 50 cm^{-1} for six-coordinate high-spin Co^{2+} and less than 10 cm^{-1} for four-coordinate

Table 6. VTVH MCD Fitting Parameters.

Parameter	[CoCo(*Nm*DapE)] [a]	[CoCo(*Nm*DapE)] + Captopril[b]	[CoCo(*Hi*DapE)][c]	[CoCo(*Hi*DapE)] + Captopril[d]
J (cm^{-1})	0	-0.1	0	-0.05 ±0.04
D (cm^{-1}), 4C	3.7 ±0.6	0.05	3.7 ±1.0	4.1 ±1.5
E/D, 4C	~0	0.002	~0	0.25 ±0.14
D (cm^{-1}), 6C	>100	>50	>100	28 ±5
E/D, 6C	0.18 ±0.04	~0	0.27 ±0.04	0.08 ±0.03
Polarizations	503 nm x-pol.	505 nm na	503 nm x-pol.	505 nm z-pol.
	532 nm xy-pol.	530 nm na	532 nm xy-pol.	530 nm z-pol.
	576 nm xy-pol.	604 nm z-pol.	576 nm xy-pol.	604 nm z-pol.

[a]Based on 3 independent experiments; ± one standard deviation. [b]Based on a single experiment. [c]Based on 8 independent experiments. [d]Based on 4 independent experiments.

high-spin Co^{2+}.[29, 106c] The addition of 1 eq. (based on concentration of active sites) of L-captopril to either [CoCo(*Hi*DapE)] or [CoCo(*Nm*DapE)] has no apparent effect on the MCD spectra. However, addition of 5 eq. of L-captopril causes the green resting enzyme solutions to turn blue (Figure 22B). The four-coordinate Co^{2+} bands shift from 532, 559 and 576 nm in [CoCo(*Hi*DapE)] to 530, 565 and 604 nm in the [CoCo(*Hi*DapE)]-L-captopril complex while the four-coordinate Co^{2+} bands shift from 532, 558 and 576 nm in [CoCo(*Nm*DapE)] to 530, 565 and 604 nm in the [CoCo*Nm*DapE]-L-captopril complex. The six-coordinate band at 503 nm splits into two bands at 488 and 505 nm for both [CoCo(*Hi*DapE)]-L-captopril and [CoCo(*Nm*DapE)]-L-captopril. There is a small peak at 576 nm in both spectra, which is due to uncomplexed enzyme. In addition to these band shifts, there is a roughly three-fold decrease in MCD intensity, which is not due to any removable of metal from the enzyme by L-captopril. Finally the quality of the optical glasses formed in the presence of L-captopril was not as high as for the resting

enzyme alone. This resulted in MCD spectra that had considerably lower signal to noise than in the MCD spectra of the resting enzymes.

VTVH MCD data were also collected on the 505, 530, and 604 nm bands in [CoCo(*Hi*DapE)]-L-captopril and only for the 604 nm band in [CoCo(*Nm*DapE)]-L-captopril. Example magnetization plots and fits are shown in Figures SI-9 through SI-12. The χ^2 values for the 505 and 530 nm band fits are quite high as is the χ^2 value for the 604 nm band fit in [CoCo(*Nm*DapE)]-L-captopril. The best fits were obtained with a small negative value for *J*. In addition the ZFS parameters for both the six- and four-coordinate sites changed, but are still in the ranges expected for four- and six-coordinate Co^{2+} (Table 6).

EXAFS of L-captopril bound to [ZnZn(HiDapE)]. Zn K-edge extended X-ray absorption fine structure (EXAFS) spectra were recorded for [ZnZn(*Hi*DapE)] in the presence of L-captopril (Figure 23). The EXAFS data reveal an average of both metal ion environments. The dominant peak in the Fourier transformed (FT) EXAFS data for [ZnZn(*Hi*DapE)] is centered at ~2.0 Å with a second shell feature at ca. 3.3 Å, identical to previously reported EXAFS data.[81] Coordination of L-captopril to [ZnZn(*Hi*DapE)] results in EXAFS spectra that can be fit to 5 ± 1 N/O scatterers. However, the Zn-Zn distance increases from 3.32 to 3.40 Å. In addition, the EXAFS data for [ZnZn(*Hi*DapE)]-L-captopril reveal a new feature at 2.3 Å that is highly characteristic of a direct zinc-sulfur interaction.

Figure 23. Zn K-edge EXAFS spectra of a 1 mM solution of [ZnZn(*Hi*DapE)] 50 mM HEPES buffer, pH 7.5 in the absence (red) and presence (black) of L-captopril.

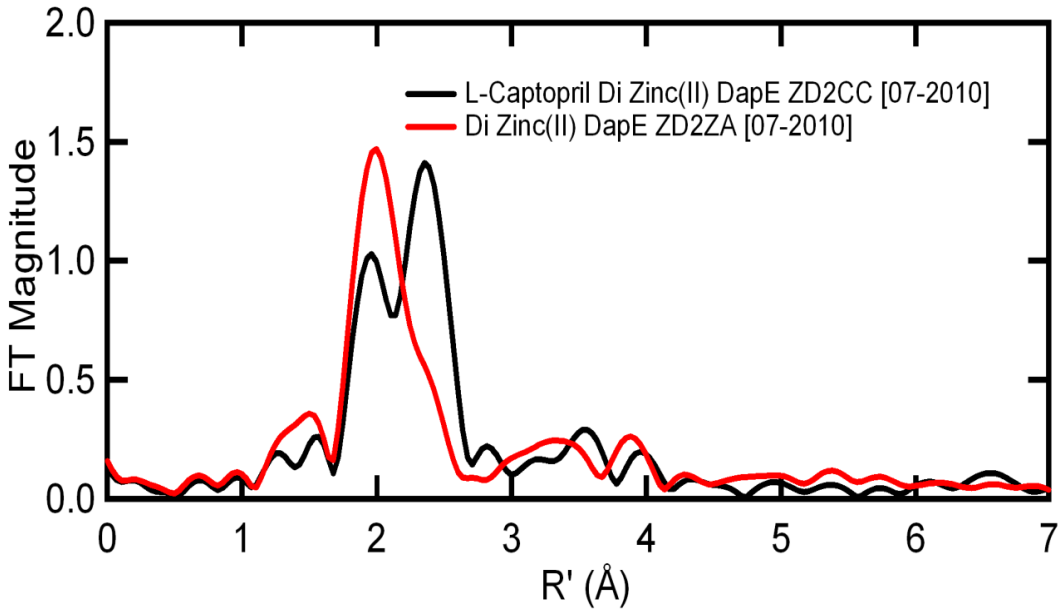

Crystal structures of [Zn_(NmDapE)],[ZnZn(NmDapE)], and the L-captopril bound [ZnZn(NmDapE)] complex. The X-ray crystal structures of [Zn_(*Nm*DapE)], (2.1 Å), [ZnZn(*Nm*DapE)] (2.0 Å) and the [ZnZn(*Nm*DapE)]-L-captopril complex (1.8 Å) were solved. These three structures along with apo-*Nm*DapE, which was previously determined (1vgy) [109], reveals the typical two-domain homodimer structure (either present in the asymmetric unit, or generated by the crystallographic two-fold axis) observed for all DapE enzymes. Comparison of all four structures of *Nm*DapE shows that the overall fold is well preserved and the structures of the apo, mono and di-zinc, and L-captopril bound forms are nearly identical. Each of these structures overlay with an rmsd for Cα atoms of 0.59 Å (apo-*Nm*DapE over [Zn_(*Nm*DapE)]) and 0.73Å (apo-*Nm*DapE over [ZnZn(*Nm*DapE)] and L-captopril bound [ZnZn(*Nm*DapE)]). Close

analysis of the [ZnZn(*Nm*DapE)] and [ZnZn(*Nm*DapE)]-L-captopril structures (both were determined from isomorphous crystals grown under similar conditions (Table 4), reveals that inhibitor binding does not introduce any significant changes in the structure as evidenced by a very low rmsd deviation of 0.2 Å. Furthermore, analysis of the active site regions of the [ZnZn(*Nm*DapE)] structure indicates that the metal ions and ligands are in nearly identical positions. The dinuclear Zn^{2+} active sites in both [ZnZn(*Nm*DapE)] and the [ZnZn(*Nm*DapE)]-L-captopril complex adopt identical coordination geometries to that reported for *Hi*DapE.[37]

For [ZnZn(*Nm*DapE)], the first metal binding site, Zn1, resides in a distorted tetrahedral geometry and is bound by the carboxylate oxygen atoms OD1 of D101 and OE1of E164 as well as a nitrogen atom NE1 of H68. The Zn2 metal ion resides in a distorted trigonal bipyramidal geometry and is bound by a nitrogen atom NE2 of H350, two oxygen atoms, OD2 from D101 and OE2 from E136, and the O1 oxygen atom of ethylene glycol. Interestingly, for [Zn_(*Nm*DapE)] a full dimer resides in the asymmetric unit and Zn^{2+} binding is different between the two active sites. In one of the active sites, a single Zn^{2+} ion is bound in the first metal binding site while in the second active site site, two Zn^{2+} ions are present but with occupancies modeled at 50% for Zn1 and 20% for Zn2. These data suggest that metal binding is not sequential for *Nm*DapE, which is different from that observed for *Hi*DapE.

The structure of the [ZnZn(*Nm*DapE)]-L-captopril complex was obtained by co-crystallization of [ZnZn(*Nm*DapE)] and L-captopril and solved to 1.8 Å resolution. The structure reveals clear electron density corresponding to L-captopril inside the positively

charged grove, formed between the catalytic and the dimerization domains (Figure 24). The sulfhydryl group of L-captopril bridges between the two active site Zn^{+2} ions with a Zn-S distance of 2.3 Å and a Zn2-S distance of 2.3 Å, displacing the bridging water molecule. The carboxy-end of the proline moiety of L-captopril forms a hydrogen bonds with N346 (ND2-O3, 3.0 Å) and the amide of G325 (N-O2, 2.9 Å). It also forms a strong hydrogen bond with the hydroxyl of Y198 (OH-O3, 2.5Å), which reaches over from the second subunit of the dimer. The O1 carbonyl oxygen of the L-captopril (the carbonyl oxygen of the peptide bond) also forms a hydrogen bond with a well-ordered water molecule (2.8Å), which is stabilized by its interaction with R179 (NH2-O 3.1 Å) and P165 (2.6 Å)

Discussion

Because of the emergence of bacterial resistance to antibiotics used in current standard of care, new small molecules need to be designed and synthesized that inhibit novel antibacterial enzyme targets, such as DapE. Several structural classes that containing different zinc-binding groups (ZBG's) such as carboxylic acids, boronic acids, phosphates, and thiols have been reported to inhibit DapE enzymes. Thiols are commonly used as inhibitors for Zn^{2+} metalloproteins since Zn(II) is a soft acid and thiols are soft bases.[110] Examination of several thiol based compounds has led to the identification of low micromolar inhibitors of DapE.[81, 92] For example, L-penicillamine exhibits an IC50 value of 13.7 μM, and is a competitive inhibitor of *Hi*DapE with a measured K_i of 4.6 μM. DapE is also stereoselective with respect to the recognition of substrate and inhibitors, as D-penicillamine provided an IC50 value of 50 μM.[92]

Figure 24. Structure of [ZnZn(*Nm*DapE)] bound by L-captopril. (A) Ribbon diagram of the homodimer of [ZnZn(*Nm*DapE)] (subunit A in orange and subunit B in blue). The Zn^{2+} ions in the dinuclear active site are shown as black spheres while molecules of L-captopril are shown as green sticks. (B) Close-up of the active site region showing the hydrogen bonding interactions of L-captopril (green) with surrounding protein residues and solvent molecule (red sphere). The active site residues are color coded (orange and blue sticks) according to the subunit coloring, while the conserved residues binding to the Zn^{2+} ions are grey. (C) Schematic drawing of the dinuclear Zn^{2+} active site bound by L-captopril (distances are displayed in angstroms).

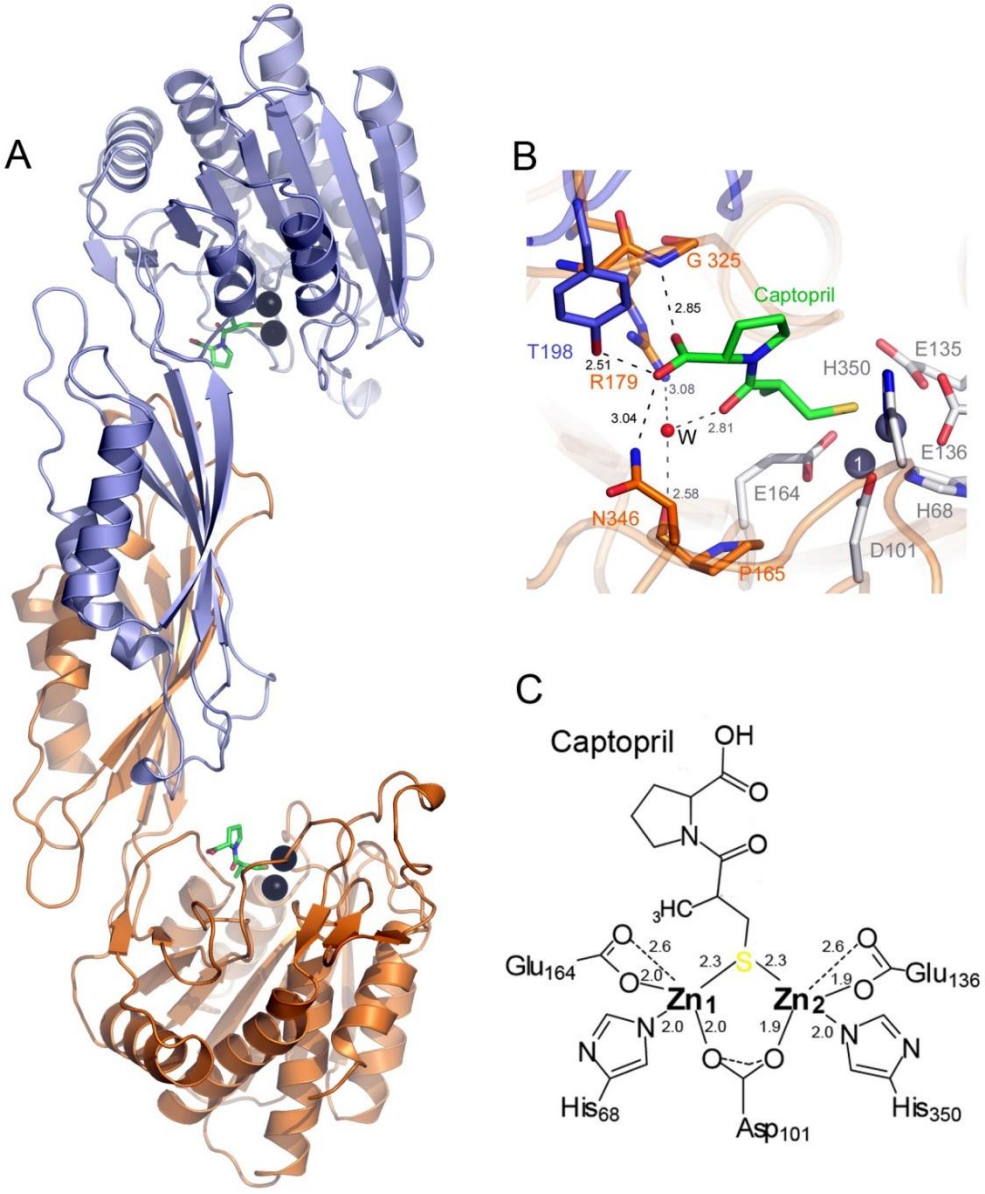

Similarly, L-captopril, and angiotensin-converting enzyme (ACE) inhibitor, exhibited an IC50 value of 3.3 μM towards *Hi*DapE and is also a competitive inhibitor with a measured K_i of 1.8 μM while D-captopril yielded an IC50 value of 42 μM. Similar to *Hi*DapE, L-captopril is a competitive inhibitor of *Nm*DapE with a measured K_i of 2.8 μM. Interestingly, it has been showed recently by Uda *et al.* that L-captopril targets only the Zn^{2+}-metallo-isoform of the enzyme, whereas the Mn^{2+}-enzyme was not inhibited. Since the Mn^{2+}-substituted isoform is also physiologically relevant in bacteria, it is important while designating inhibitor compounds, as it has implications in substrate and ligand binding at the active site in vivo.[111] Even though L-captopril is a tight binding inhibitor of DapE enzymes and is a promising lead compound for the development of a novel class of DapE inhibitors, no information exists on how L-captopril binds to DapE, a requirement for the rational design of new, more potent DapE inhibitors.

Evidence of L-captopril binding to the dinuclear active site of DapE was gleaned from spectroscopic data obtained on the L-captopril complexes of the Co^{2+}-substituted forms for both *Hi*DapE and *Nm*DapE ([Co_(*Nm*DapE)], [CoCo(*Nm*DapE)], [Co_(*Hi*DapE)] and [CoCo(*Hi*DapE)]). Electronic absorption spectra suggest that the Co^{2+} ions bound to both *Hi*DapE and *Nm*DapE reside in either a distorted five- or six-coordinate site.[67b] Upon the addition of L-captopril to either [CoCo(*Nm*DapE)] or [CoCo(*Hi*DapE)], results in UV-Vis spectra where the λ_{max} is red-shifted by ~30 nm while the molar absorptivities increase by ~120 $M^{-1}cm^{-1}$ (Figure 19) The observed changes upon L-captopril binding to the Co^{2+}-forms of both *Nm*DapE and *Hi*DapE, suggest that L-captopril interacts with both active site Co^{2+} ions.

Interestingly, EPR spectra of [Co_(*Nm*DapE)] and [Co_(*Hi*DapE)] suggest the Co^{2+} ion resides in a distorted tetrahedral coordination geometry at low temperature since an $M_S = \pm {}^3/_2$ signal persists between the temperatures of 4.5 and 13K, characterized by a spike at $g' \sim 6.5$ (Figure 20).[67b] The fact that the presence of a feature at 13 K due to an $M_S = \pm {}^1/_2$ transition is almost completely extinguished at 4.5 K and high microwave powers, renders the five- or six-coordination geometry highly unlikely and is explained by thermal population of the $M_S = \pm {}^1/_2$ Kramers' doublet. EPR spectra of [CoCo(*Nm*DapE)] and [CoCo(*Hi*DapE)] indicate a five- or six-coordinate Co^{2+} ion in the second binding site due to the slow-relaxing ground state $M_S = \pm {}^1/_2$ signal present at both high and low temperatures and reveal substantial line-broadening at the low-field line upon binding the second Co^{2+} ion, suggesting an increase of geometric flexibility within the second Co^{2+} binding site.[67b] The EPR data also suggest an antiferromagnetic interaction due to the formation if a spin-coupled species with $|J| >> 0.3$ cm^{-1} between the Co^{2+} ions in [CoCo(*Hi*DapE)].[67b] Some of the Co^{2+} appears to be EPR silent and the $M_S = \pm {}^3/_2$ signal is significantly diminished in [CoCo(*Hi*DapE)] compared to [Co_(*Hi*DapE)] which is not the case for [CoCo(*Nm*DapE)]. The addition of L-captopril to [CoCo(*Nm*DapE)] and [CoCo(*Hi*DapE)] essentially extinguished the $M_S = \pm {}^3/_2$ signal; however, the other signals are unperturbed, indicating that the tetrahedral species has gained a ligand (Figure 21). On the other hand, the addition of L-captopril to [CoCo(*Hi*DapE)] abolishes the EPR intensity suggesting that the spin-coupling between the two Co^{2+} ions increases upon L-captopril binding indicative of a thiolate bridge between the two active site Co^{2+} ions.

Additional electronic information on [CoCo(*Nm*DapE)] and [CoCo(*Hi*DapE)] and their L-captopril complexes was derived from MCD data (Figure 22). For both [CoCo(*Nm*DapE)] and [CoCo(*Hi*DapE)] characteristic bands for high-spin Co^{2+} in a distorted tetrahedral and distorted octahedral ligand field are observed, consistent with EPR data. An interesting finding is that despite the similarity in the MCD spectra between [CoCo(*Nm*DapE)] and [CoCo(*Hi*DapE)], the spectra obtained for [CoCo(*Nm*DapE)] reveals that both the four- and six-coordinate sites are occupied upon the addition of only 1 eq. of Co^{2+} suggesting a cooperative binding model for *Nm*DapE that is not observed for *Hi*DapE. This finding is consistent with EPR data as well as the X-ray crystal structure of [Zn_(*Nm*DapE)] where one of the active sites contains a Zn^{2+} ion bound in the first metal binding site while in the second active site contains two Zn^{2+} ions with occupancies modeled at 50% for Zn1 and 20% for Zn2. Correlation of the observed ZFS with coordination number was used as a coordination number indicator (referred to as the CN/ZFS correlation). In the CN/ZFS correlation, four-coordinate Co^{2+} exhibits ZFS < 13 cm^{-1}, five-coordinate between 20 and 50 cm^{-1}, and six-coordinate > 50 cm^{-1}.[112] The ZFS parameters determined from fits of VTVH data for [CoCo*Nm*DapE] and [CoCo*Hi*DapE] are consistent with four-coordinate and six-coordinate Co^{2+} centers in the active site. Based on previously published magnetic properties of several μ-aqua μ-hydroxo dicobalt(II) model complexes, weak to moderately strong antiferromagnetic coupling would be expected from a single oxygen atom bridge.[113] Fitting of the VTVH data from [CoCo*Nm*DapE] and [CoCo*Hi*DapE] strongly suggest that the bridging atom is in the μ-aqua as opposed to a μ-hydroxo form.

Upon the addition of L-captopril to [CoCo*Nm*DapE] and [CoCo*Hi*DapE] the bands shift for both the four- and six-coordinate Co^{2+} ions and a decrease in the MCD intensity is also observed (Figure 22). These data are consistent with the thiol of L-captopril bridging between the two active site Co^{2+} ions producing an antiferromagnetically coupled dicobalt(II) center with an S = 0 ground-state. The overall changes strongly suggest that the L-captopril displaces the bridging water molecule and binds to both metals through a monatomic bridge that exhibits a lower ligand field strength than that of water. These data are consistent with EPR data and also EXAFS spectra for [CoCo*Hi*DapE] bound by L-captopril. Upon binding L-captopril, the Zn-Zn distance increases by 0.08 Å and a new feature at 2.3 Å appears that is highly characteristic of a direct zinc-sulfur interaction. Taken together, these data indicate that L-captopril interacts with both metal ions and strongly suggests the replacement of the bridging water molecule with a more strongly bound ligand such as the thiol functionality of L-captopril.

A major limitation in developing a previously undescribed class of antimicrobials that target DapE enzymes is the lack of knowledge about inhibitor binding to the DapE active site including potential residues involved in substrate recognition and binding. While the spectroscopic studies suggest that L-captopril bridges between the two active site metal ions in DapE in solution *via* a μ-thiolate moiety, these data provide no detailed information regarding any interaction of the remaining functional groups of L-captopril with the active site. In order to further characterize the binding of L-captopril to DapE, the [ZnZn(*Nm*DapE)] enzyme was crystallized in the presence of L-captopril and the X-

ray crystal structure was determined to 1.8 Å resolution (Figure 24). As predicted by the EPR, MCD, and EXAFS data, no active site ligands are displaced upon L-captopril binding except the water molecule that bridges the two Zn^{2+} ions in the wild-type structure. This bridging water molecule is displaced by the thiol sulfur of L-captopril with Zn1-S and Zn2-S distances 2.3 Å. L-captopril binding also increases the Zn-Zn distance from 3.3 Å to 3.4 Å. The binding of L-captopril to the dinculear active site of [ZnZn(*Nm*DapE)] provides the first structural data for an inhibited form of any DapE enzyme providing a model for inhibitor design as well as enzyme-substrate interactions.

DapE enzymes have strict specificity for the L,L-isoform of SDAP.[67b] This specificity is built into the active site that includes both the dinuclear metal cluster as well as adjacent amino acid residues that form a substrate binding pocket. Several studies indicate that substrate binding pockets play an important role in substrate recognition and binding for metallohydrolases.[41a, 114] Inspection of the X-ray crystal structures of [Zn_(*Nm*DapE)] and [ZnZn(*Nm*DapE)], combined with surface analysis, reveals a smile-shaped cavity that extends along the catalytic domain and surrounds the active site. This well-defined and negatively charged cavity is shaped from the top by strand β12 and α8 and in the middle by the loop connecting these two elements. The bottom of the cavity is formed by a loop connecting β-strands β6 and β7, and a loop connecting β5 and α4. Taking into account the linear character of the substrate, it is likely that the substrate binds in an extended conformation, lining up along the grove with the peptide bond positioned over the active site metals. Insight into the role of this cavity comes from the [ZnZn(*Nm*DapE)]-L-captopril structure as several interactions between the inhibitor and

residues within this cavity are formed. The O1 carbonyl oxygen of the L-captopril (the carbonyl oxygen of the peptide bond) forms a hydrogen bond with a well-ordered water molecule (2.8Å), which is stabilized by R179 (NH2-O; 3.1 Å) and P165 (2.6 Å). In addition, the carboxy-end of the proline moiety of L-captopril is held in position by ionic interactions between N346 (ND2-O3; 3.0 Å) and the amide of G325 (N-O2; 2.9 Å). Interestingly, the carboxy group also forms a hydrogen bond with the hydroxyl moiety of Y198 (OH-O3; 2.5 Å), which resides on the other subunit of the dimer. This interaction is of great interest, since it is first evidence of a residue from the second subunit interacting with an inhibitor bound to the first subunit. This suggests a heretofore unknown function for the dimerization of DapE enzymes. These data suggest that the dimerization domain is not only crucial for dimer formation but could also play an important role in substrate recognition and binding of substrate. This is consistent with dimerization domain deletion mutants of *Hi*DapE, which were inactive highlighting the importance of DapE dimer formation.[37]

In summary, we have spectroscopically and crystallographically characterized the binding of L-captopril to DapE. The thiol moiety of L-captopril coordinates to both active site metal ions in a μ-thiolate fashion. No other inhibitor centered ligands interact with the active site metal ions. Since the X-ray crystal structure of the [ZnZn(*Nm*DapE)]-L-captopril complex is the first structure of a DapE enzyme complexed by an exogenous ligand, several active site pocket residues including R179, P165, and N346 were identified that form hydrogen bonds to functional groups of L-captopril. Remarkably, the Y198 residue on subunit B was discovered to be involved in hydrogen bond formation with the

L-captopril inhibitor bound to the active site in subunit A. This unforeseen hydrogen bonding interaction may prove crucial in the development of novel medicinal chemistry leads and may also be critical for catalysis. Since L-captopril is an angiotensin-converting enzyme (ACE) inhibitor and a moderately strong inhibitor of DapE enzymes, understanding the electronic and structural properties of L-captopril binding to the active site of DapE provides a foundation for the design of new, more potent DapE inhibitors.

CHAPTER FOUR

DISCOVERY OF NOVEL DAPE INHIBITORS THROUGH HIGH-THROUGHPUT SCREENING

Introduction

Bacterial infections, some of which were thought to be eradicated, have made a significant resurgence due to bacterial resistance to all known antibiotics.[2, 4-5, 115] Resistance occurs because microorganisms that cause infections quickly develop ways to survive drugs meant to kill or weaken them through random mutation and natural selection. Once a mutated gene is generated, bacteria horizontally transfer this genetic information by plasmid echange.[4-5] Consequently, it's important to the health and general welfare of society to continually renew our arsenal of compounds that combat these pathogens.[116] Ideally, such new compounds would target enzymes involved in bacterial cell wall synthesis or pathways involved in cell replication.[117] The dapE-encoded N-succinyl-L,L-diaminopimelic acid desuccinylase (DapE), a member of the *meso*-diaminopimelate (mDAP)/lysine biosynthetic pathway, is just such as candidate as a novel target for the development of a new class of antibiotics. DapE's catalyze the hydrolysis of N-succinyl-L,L-diaminopimelic acid (SDAP) to diaminopimelate and succincate (Figure 4), both of which are required for protein synthesis and peptidoglycan layer formation in both Gram-positive and Gram-negative bacterial cell walls.[59] Deletion of the gene encoding for DapE, is lethal to *H. pylori* and *M. smegmatis*, even in the

presence of lysine supplemented media.[55] Therefore, DapEs are essential for cell growth and proliferation. Since there are no similar biosynthetic pathways in mammals, inhibitors that target DapEs are hypothesized to exhibit selective toxicity against bacteria.[27]

DapE enzymes belong to the M28 family of dinuclear Zn(II)-dependent metalloproteases all of which contain a (μ-aquo)(μ-carboxylato)dizinc(II) core with one terminal carboxylate and one histidine residue at each metal site.[62] The amino acid residues that function as metal ligands in the crystallographically characterized DapE enzymes are identical to other M28 family members, including the carboxypeptidase from *Pseudomonas sp* strain-RS-16 (CPG2) and the leucine aminopeptidase from *Aeromonas proteolytica* (AAP), which contain a terminal histidine and carboylate residue at each site.[28-29, 64a, 67b, 88b] X-ray crystallographic and kinetic data obtained on the DapE from *Haemophilus influenzae* (*Hi*DapE) indicate that the divalent metal binding sites bind in a sequential fashion and that the enzyme exhibits ~60% activity, based on k_{cat}, in the presence of one Zn(II) ion. These structural data provide the foundation for the design and synthesis of novel molecules, representing different structural classes that contain various zinc-binding groups (ZBGs). Typical ZBGs include thiols, carboxylic acids, boronic acids, and phosphates. High-throughput screening (HTS) has been successful in discovoring inhibitors for several metallohydrolases, including metalloform-specific inhibitors (*i.e*. preferentially bind to mononuclear vs. dinuclear forms of an enzyme). For example, metalloform-specific inhibitors has been identified

using HTS for methionine aminopeptidases (MetAP), which bind one metal ion *in vivo* and are active with a variety of divalent first row transition metal ion.[118]

Inhibitor screening *via* HTS of DapE enzymes has been limited by the lack of a spectrophotometric assay that is amenable to HTS. To overcome this issue, we report herein a reliable and reproducible spectrophotometric assay for DapE enzymes. Utilizing this assay, we analyzed the binding ability of over 39,000 compounds representing different structural classes and containing different ZBG's. This approach identified five novel inhibitors of DapE enzymes and these lead compounds, along with several derivatives, were examined to determine their potential structure-activity relationships (SARs).

Materials and Methods

Reagents. All chemicals used were purchased commercially and were of the highest quality available. All metal reagents were obtained from Strem Chemicals, Newburyport, MA with ≥99.999% purity. Stock solutions Zn(II) (10 mM) were prepared by dissolving the metal chloride salts ($ZnCl_2$) in nanopure water.

Expression and Purification of HiDapE. Plasmid containing the *Hi*DapE gene with an N-terminal His_6-tag was transformed into BL21(DE3)/magic *Escherichia coli* competent cells and grown in Luria-Bertani Broth as previously reported.[119] The following steps were performed at 4 ˚C. The DapE was purified according to the standard protocol for Ni-NTA affinity chromatography, as described previously.[91] The His_6-tag was removed by treating each enzyme with His_6-tagged TEV protease for 16 h at

4 ˚C in 50 mM HEPES, pH 8.0. Cleaved protein was separated from TEV using Ni-NTA affinity chromatography.

Expression and purification of L,L-diaminopimelate aminotransferase (LL-DAP-AT) from E. coli. The plasmid for LL-DAP-AT was kindly provided by Professor John C. Vederas and LL-DAP-AT was expressed and purified following the published procedure.[120] Briefly, the plasmid was transformed into *E. coli* strain M15 (pREP4) (Qiagen Inc.) and grown in 2×YT medium at 37 ˚C until an OD_{600} of 0.7 was reached with shaking. IPTG was added (1 mM) and culture growth was continued for 4 h. Cells were recovered by centrifugation (12,000g) for 15 min. at 4 ˚C using a Beckman Coulter Avanti J-E Centrifuge. The resulting cell paste was suspended in lysis buffer (50 mM sodium phosphate, 300 mM NaCl, 10 mM imidazole, 10 mM 2-mercaptoethanol (pH 7.7) and lysed by sonication. Next, the protein was purified according to the standard protocol for Ni-NTA affinity chromatography, as described previously.[91] The column was washed with lysis buffer and eluted using a gradient of 50 mM sodium phosphate, 300 mM NaCl, 200 mM imidazole, and 10 mM 2-mercaptoethanol (pH 8.0). The protein was dialyzed against 200 mM NaCl, 20 mM HEPES- KOH (pH 7.6), 3 mM TCEP and stored at -80 ˚C until further needed.

Enzyme-Coupled Spectrophotometric Assay. Testing was carried out using 96 well plates with a total volume of 218 µl in each well. Every well on the plate, except the last row, contained 50 µL of compound (final conc 95 µM) in 1.25% DMSO. The last row served as a negative control and contained only 1.25% DMSO. Second to last row served as a positive control and contained enzyme completely inhibited by EDTA (30 mM). The reaction mixture containing DapE 0.15 µM, HEPES-KOH 100 mM (pH 7.6)

was added to individual wells on the microplate and allowed to incubate for 10 min at 25 ˚C. Next, 40 µl of the reaction mixture in HEPES-KOH (100 mM at pH 7.6) containing DapE (0.25 µM), LL-DAP-AT (1µM), 2-OG (1 mM), OAB (10 mM) was added to individual wells of the microplate using a 96-channel robotic liquid dispenser. The reaction was then initiated by addition of 1.5 mM SDAP. The initial absorbance was measured at 440 nm with a SpectraMax Plus384 microplate reader. The final absorbance was measured after 3 h.

For the discontinuous assay, the reaction mixture containing DapE 0.15 µM, HEPES-KOH 100 mM (pH 7.6) was added to individual wells on the microplate and allowed to incubate for 10 min. at 25 ˚C. The reaction was initiated by addition of 3.6 mM SDAP and the reaction was allowed to proceed for 15 min. after which is was stopped by addition of EDTA (30 mM) via the direct addition into the well and allowed to incubate for 1 h. The second part of the reaction was introduced by addition of HEPES-KOH 100 mM (pH 7.6), 2-OG (8.5 mM), OAB (10 mM), and LL-DAP-AT (3µM) and the initial absorbance was measured at 440 nm with a Spectra94 microplate reader and again after 3 h at the plateau region.

Controls on LL-DAP-AT were carried out in similar fashion using 96 well plates. Every well on the plate, except the last row, contained 50 µL of compound (final conc 95 µM) in 1.25% DMSO. The last row served as a negative control and contained only 1.25% DMSO. The second to last row served as a positive control and contained no LL-DAP-AT enzyme. Next, a reaction mixture containing HEPES-KOH 100 mM (pH 7.6), 2-OG (8.5 mM); OAB (7 mM); DAP (2.3 mM assuming 25% of total DAP) was

aliquated to each well on a plate. The reaction was initiated by addition of LL-DAP-AT (3μM) and the absorbance was monitored at 440 nm on a Spectra94 microplate reader.

High-Throughput Screening. High-throughput screening was carried out using 348 well plates with a total volume of 60 μl in each well. Every well on the plate, except the last row, contained 20 μL of compound (final conc 12 μM) in 1.25% DMSO. The last row served as a negative control and contained only 1.25% DMSO. The second to last row served as a positive control and contained no DapE enzyme. Next, 40 μl of the reaction mixture in HEPES-KOH (100 mM at pH 7.6) containing DapE (0.25 μM), LL-DAP-AT (1μM), 2-OG (1 mM), OAB (10 mM) was added to individual wells of the microplate using a 96-channel robotic liquid dispenser. The reaction was initiated by the addition of 1.5 mM of SDAP and the initial absorbance measured at 440 nm with a SpectraMax Plus384 microplate reader. The final absorbance was measured after 3 h.

Results and Discussion

The discovery of novel inhibitors of DapE enzymes has been hindered due to the lack of a spectrophotometric assay that can continuously monitor, in real-time, a product in the visible region.[26] The current DapE kinetic assay monitors the decrease in absorbance at 225 nm due to the hydrolysis of N-succinyl-L,L-diaminopimelic acid (SDAP), forming L,L-diaminopimelic acid (DAP) and succinate (Figure 4). Unfortunately, measurements performed at wavelengths in the UV region are subject to significant interference from other biological components, inhibitor side-chains, and compounds commonly used to make buffer solutions. Therefore, such an assay is not

Figure 4. Reaction catalyzed by DapE.

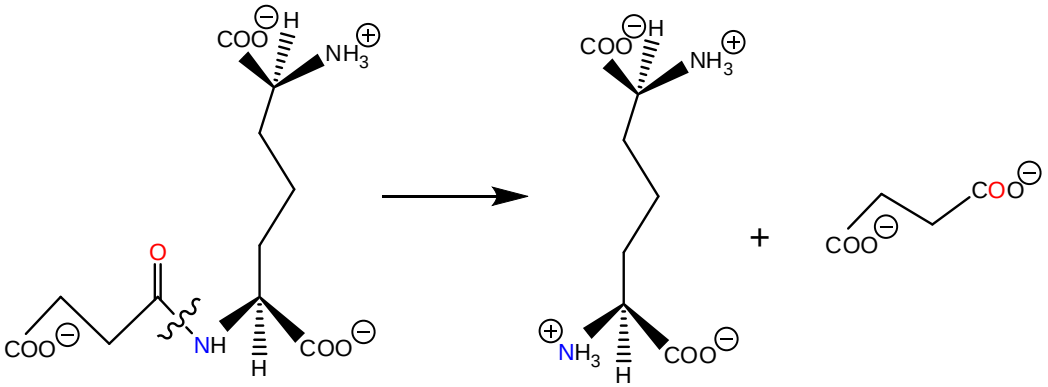

N-succinyl-L,L-diaminopimelic acid (SDAP) **L,L-diaminopimelic acid** **Succinic acid**

amenable to HTS. To overcome this issue, an enzyme-coupled continuous spectrophotometric assay was developed for DapE in 100 mM HEPES-KOH at pH 7.6 in the presence of 1.25% DMSO based on the production of the DapE product DAP. As previously reported, DAP functions as a substrate for LL-diaminopimelate aminotransferase (LL-DAP-AT) from *Arabidopsis thaliana*, which can utilize DAP as an amino donor and 2-oxoglutarate (2-OG) as an amino acceptor, to produce tetrahydrodipicolinate (THDP). Reaction of THDP with 2-aminobenzaldehyde (OAB) produces dihydroquinazolium (DHQ), which strongly absorbs at 440 nm (Figure 25).[121]

Figure 25. Schematic for the enzyme-coupled continuous spectrophotometric assay used for high-throughput screening of DapE inhibitors.

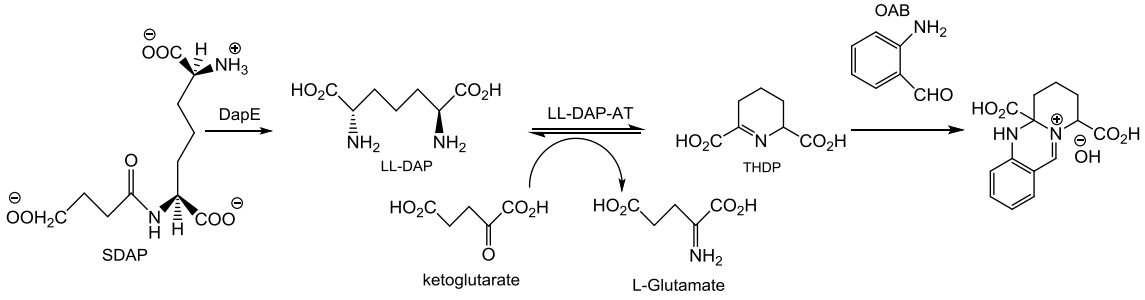

Unfortunately, the molar absorptivity of DHQ is unknown given to its instability; therefore, DapE activity can only be expressed in absorbance units (AU) for this assay. In order to optimize this enzyme-coupled continuous spectrophotometric assay for HTS experiments, several control reactions were carried out. In the absence of DapE, SDAP, OAB, LL-DAP-AT, or 2-OG no increase in absorbance at 440 nm was observed. These data indicate that the increase in absorbance observed at 440 nm is dependent on the concentration of DapE, SDAP, and LL-DAP-AT verifying that the hydrolytic reaction catalyzed by DapE is required for the production of DHQ. Titrations, in which the concentrations of DapE, SDAP, and LL-DAP-AT were systematically varied, were carried out by monitoring the absorbance at 440 nm in 100 mM HEPES-KOH at pH 7.6 in the presence of 1.25% DMSO (Figure 26). These titration data provided the optimum concentrations of DapE, SDAP, and LL-DAP-AT to produce the maximum absorbance at 440 nm. Once these concentrations were optimized, the concentrations of 2-OG and OAB were also systematically altered. Interestingly, at 2-OG concentrations greater than 1 mM, the observed absorbance at 440 nm decreased in 100 mM HEPES-KOH at pH 7.6

Figure 26. Optimization of the enzyme coupled continuous spectrophotometric assay for high-throughput screening of DapE. Varied concentration of DapE, L,L-SDAP, LL-DAP-AT, OAB and 2-OG in 100 mM HEPES-KOH, pH 7.6 at 25 °C.

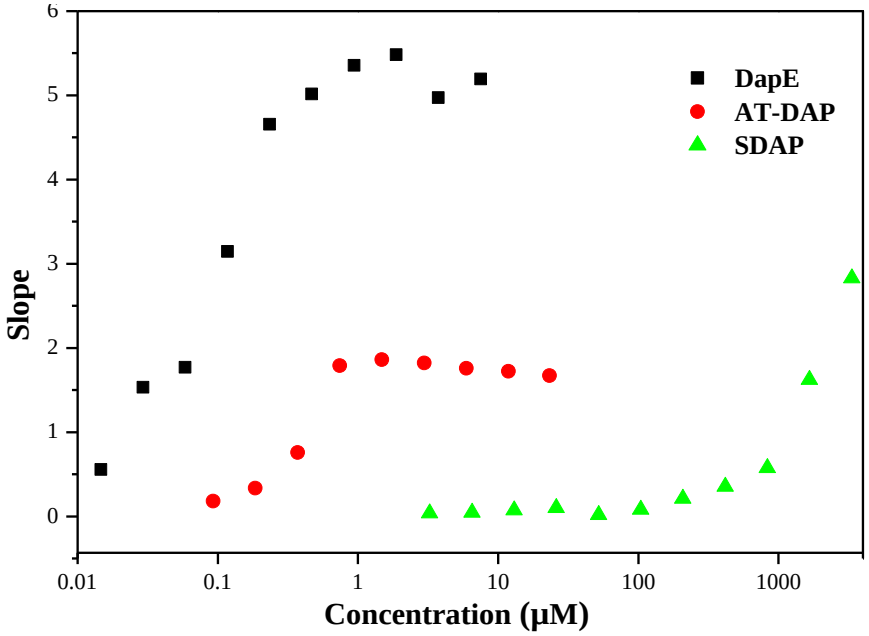

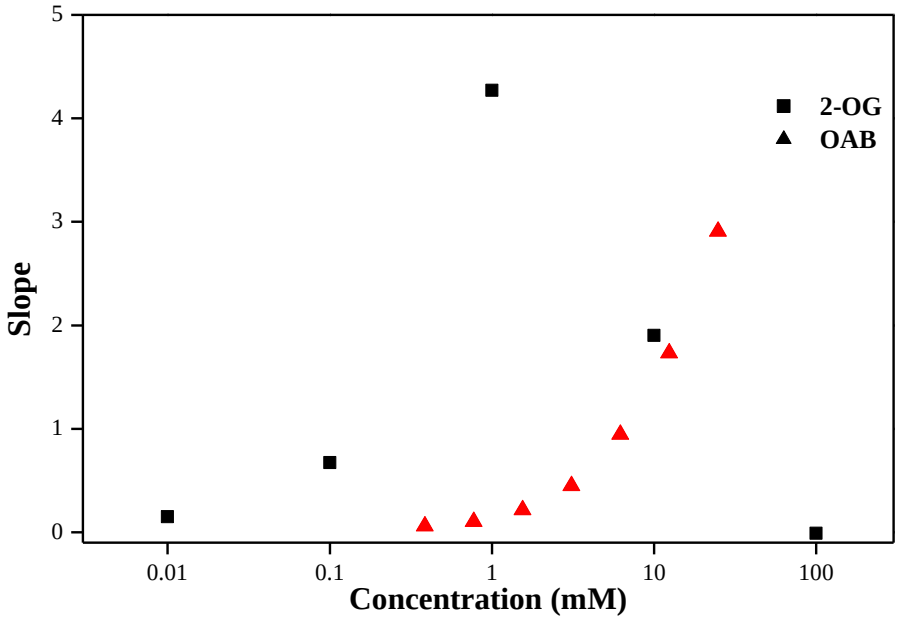

in the presence of 1.25% DMSO (Figure 3B). No such decrease was observed for OAB. This observed decrease in absorbance at 440 nm is likely due to product inhibition, since 2-OG could potentially mimic DAP at high concentrations, which is one of the products of SDAP hydrolysis. Therefore, 1 mM 2-OG concentrations were used in all screenings experiments. To further test the viability of the DapE enzyme-coupled continuous spectrophotometric assay a known DapE inhibitor, L-captopril, was examined (Figure 27). L-captopril, an angiotensin-converting enzyme (ACE) inhibitor, inhibits the DapE from *H. influenzae* with an IC50 value of 3.3 μM and a measured K_i of 1.8 μM (competitive) [42] but does not inhibit LL-DAP-AT. By monitoring the formation of DHQ at 440 nm in the presence of various concentrations of L-captopril in 100 mM HEPES-KOH at pH 7.6 in the presence of 1.25% DMSO, a clear decrease in absorbance at 440 nm is observed as a function of L-captopril concentration. The enzyme-coupled spectrophotometric assay can also be run in a discontinuous fashion. Quenching the DapE reaction after 15 min with 30 mM EDTA followed by a 1 h incubation period after which all other reagents in 100 mM HEPES-KOH at pH 7.6 are added, is adventitious to remove any metal ions that might interfere with the activity of LL-DAP-AT by binding to DAP. To test the discontinuous enzyme-coupled spectrophotometric assay, the DapE inhibitors L-captopril and L-penicillamine were investigated at various concentrations (Figure 28). As the amount of L-captopril or L-penicillamine increased, the absorbance

Figure 27. DapE activity and inhibition of L-captopril monitored using an enzymecoupled continuous spectrophotometric assay in 100 mM HEPES-KOH, pH 7.6 at 25 °C in the presence of varying concentrations of L-captopril: 0, 50, 100, 200 and 500 µM.

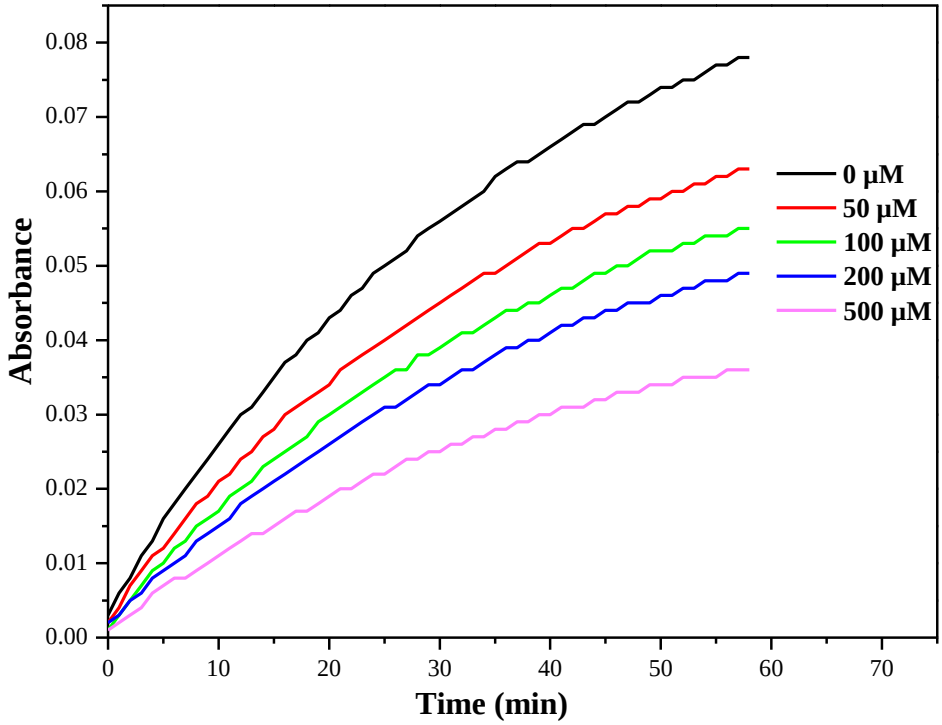

Figure 28. The inhibition of DapE using an enzyme-coupled discontinuous spectrophotometric assay in 100 mM HEPES-KOH, pH 7.6 at 25 °C in the presence of varying concentrations of (A). L-captopril: 0, 15, 50, 100, 300 and 2000 µM; and (B). L-penicillamine: 0, 300, 500, 1000 and 3000 µM.

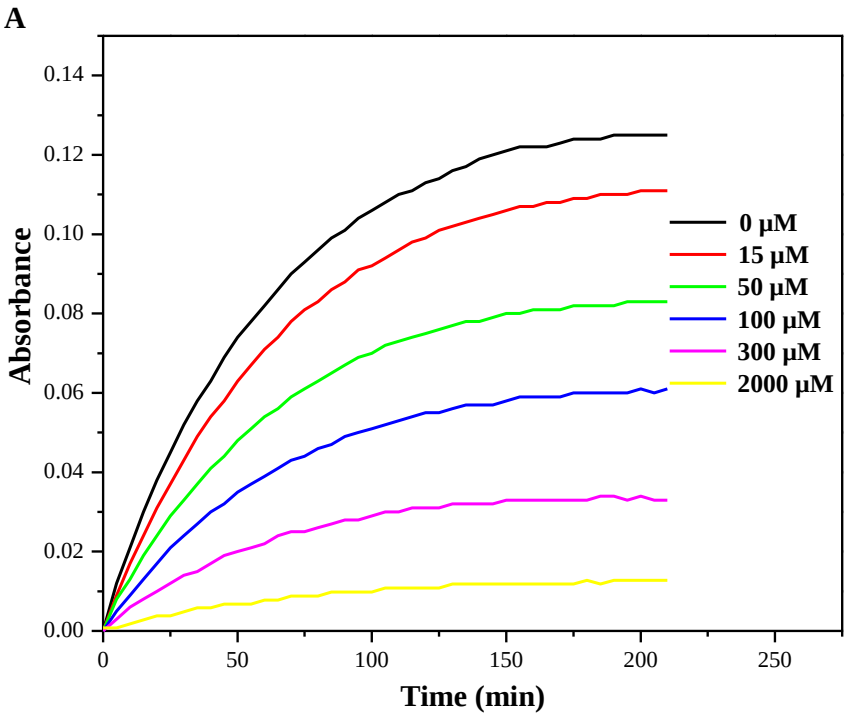

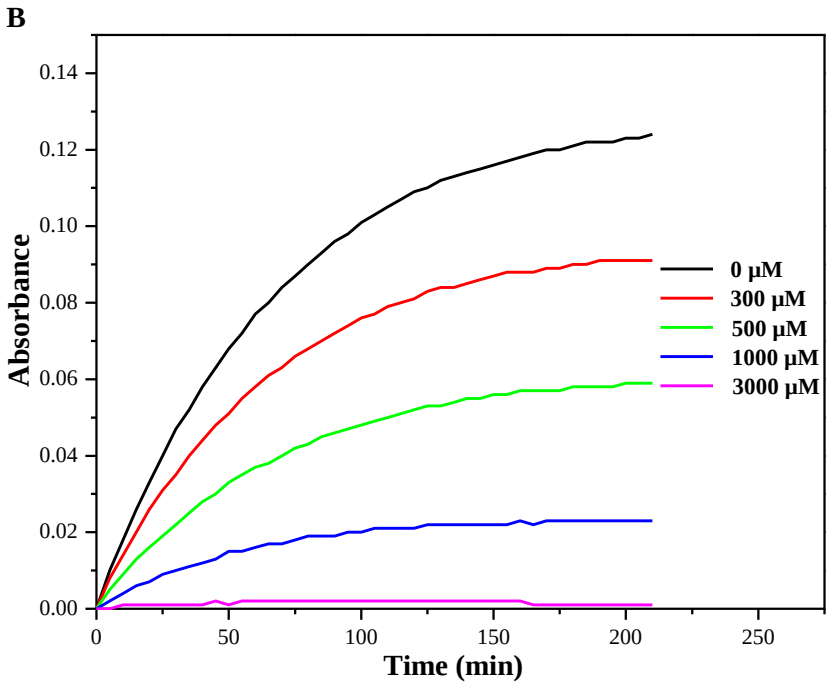

at 440 nm decreased proportionately. These data indicate that both the continuous and discontinuous assays respond as expected towards the inhibition of DapE. Therefore, this enzyme-coupled assay directly reflects the hydrolysis of SDAP by DapE.

While this enzyme-coupled continuous spectrophotometric assay for DapE appears promising, a viable HTS assay must discriminate between actual inhibitors and false positives. Therefore, prior to large-scale HTS studies, the Z'-factor, the most commonly used parameter to describe the quality of an assay, was determined where a single 384 well plate was analyzed to assess the quality of the assay, in order to warrant whether the assay's response is sufficient in comparison to control compounds. The Z' value is defined by:

$$Z' = \frac{1 - 3(SD_{control+} + SD_{control-})}{|mean_{control+} - mean_{control-}|} \qquad \text{(eq. 1)}$$

where $SD_{control+}$ and $SD_{control-}$ represent standard deviations of the signals from positive and negative controls, respectively, and $mean_{control+}$ and $mean_{control-}$ represent the values corresponding to the means.[122] The Z-factor for the DapE enzyme-coupled continuous spectrophotometric assay was found to be 0.89, indicating excellent separation between positive and negative control samples.[122] Therefore, this DapE assay is a viable endpoint-type measurement mode, which allows for an increase in throughput without sacrificing assay quality.

With a viable DapE assay in hand that is amenable to HTS, the hydrolysis of SDAP was monitored by following the formation of DHQ at 440 nm in 100 mM HEPES-KOH at pH 7.6 in the presence of 1.25% DMSO. At this point, 39,072 compounds have been screened successfully using the HTS approach. This productive screen provided

five clear hits that exhibit a >20% inhibition of DapE (Figure 29). Unfortunately, inhibition studies were not viable for any of these five compounds due to their poor solubility in buffered aqueous solution. Even so, four out of five compounds contained either a sulfonamide or sulfonyl functional group and a carbonyl moiety three to four atoms away. This structural backbone is of particular interest, as sulfonamides have previously been shown to possess biological activity particularly as antibacterials, diuretics, antidiabetics, antithyroid, antihypertensive, or antiviral agents.[123] Sulfonamides

Figure 29. Compounds discovered *via* high-throughput screening.

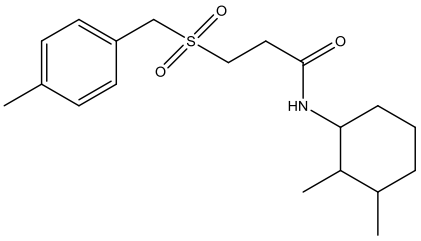

Compound A

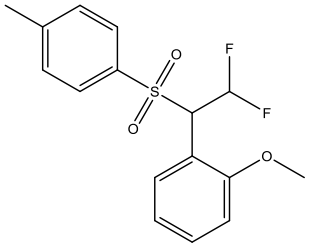

Compound B

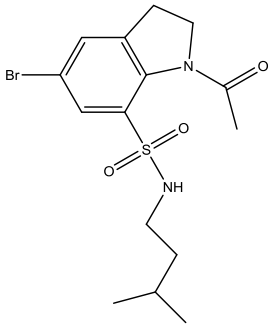

Compound C

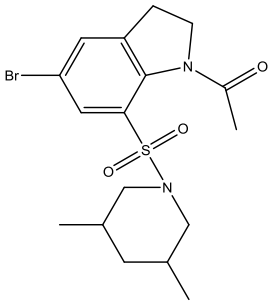

Compound D

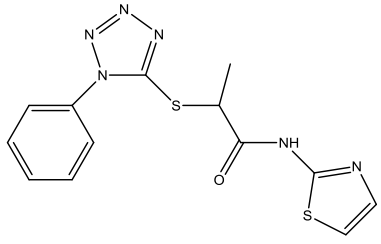

Compound E

have also attracted attention recently as the amino group can function as a metal ligand.[124] Amines are commonly used as inhibitors of Zn(II) metalloproteins since Zn(II) is a good Lewis acid and amines serve as good Lewis bases.[110] Therefore, it was hypothesized that compounds containing these groups might be involved in DapE inhibition by coordination to the dinuclear Zn(II) active site. Since two out of the five lead compounds contain idoline sulfonamides, a structure activity relationship (SAR) study was undertaken based on this molecular backbone in order to identify structural groups that are critical for DapE recognition and binding.

Several indoline sulfonamide derivatives were synthesized in collaboration with Dr. Becker, where both X and R were varied (Figure 30). Each of these inhibitors was screened using the DapE enzyme-coupled discontinuous spectrophotometric assay, and the percent inhibition calculated:

$$\% \text{ Inhibition} = \frac{(Abs_0 - Abs_I)}{Abs_0} \times 100 \qquad \text{(eq. 2)}$$

where Abs_0 is the absorbance in the absence of inhibitor while Abs_I is the absorbance in the presence of inhibitor after a 3 h reaction period.

Figure 30. Schematic for the idoline sulfonamides derivatives subjected to SAR studies.

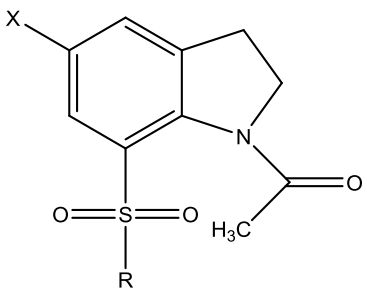

Since sulfonamides have previously been shown to be LL-DAP-AT inhibitors, as a control each inhibitor was also analyzed for inhibitory activity against LL-DAP-AT by reaction with DAP in 100 mM HEPES-KOH at pH 7.6 and monitoring the formation of DHQ at 440 nm.[125] No inhibition towards LL-DAP-AT was observed for any of the compounds tested. For comparison purposes, L-captopril inhibited 50% of the DapE activity at a concentration of 100 μM while L-penicillamine inhibited 50% of the DapE activity at a concentration of 500 μM. The best inhibitors tested were **1A**, **2A**, **3A** and **5**, which exhibited 9.2% inhibition of the DapE hydrolysis reaction (Table 7).

Table 7. Percent inhibition of derivative compounds of indoline sulfonamides (± 1.5% at 90 uM final concentrations)

Entry	Structure	%Inhibition	Entry	Structure	%Inhibition
1A	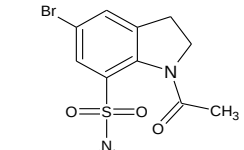	9.2	1B	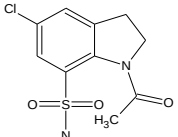	6.6
2A	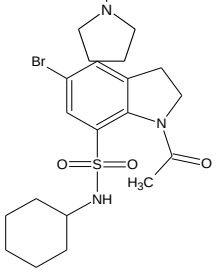	9.2	2B	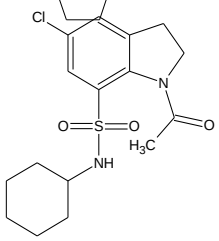	1.6
3A	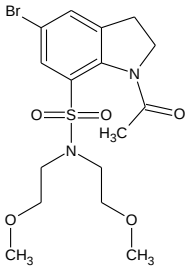	9.2	3B	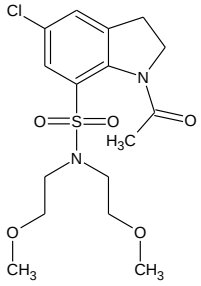	3.2
4A	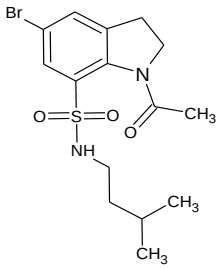	6.6	4B	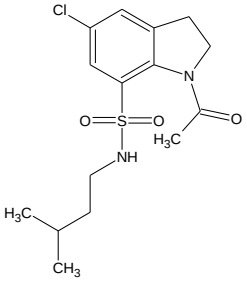	4.9
5	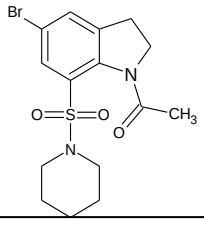	9.2			

Entry	Structure	%Inhibition	Entry	Structure	%Inhibition
6A	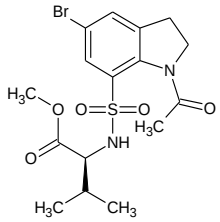	1.7	6B	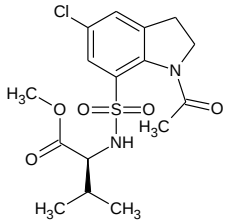	N/I
7A	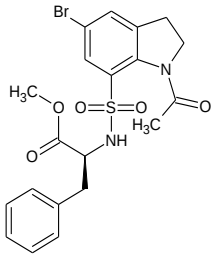	1.7	7B	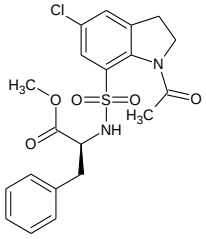	N/I
8A	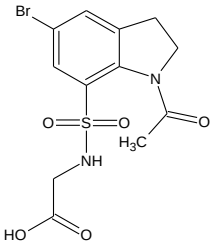	3.3	8B	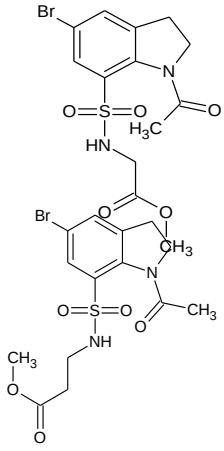	3.2
9A	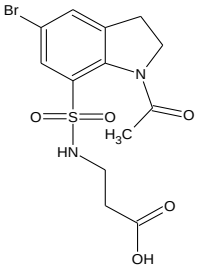	N/I	9B		3.4
10	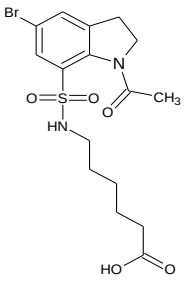	3.3			

Entry	Structure	%Inhibition	Entry	Structure	%Inhibition
11	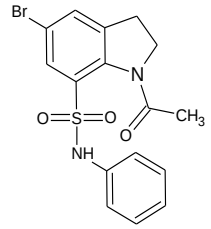	5.0	15	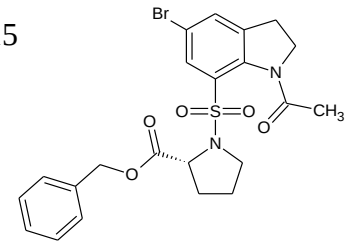	N/I
12	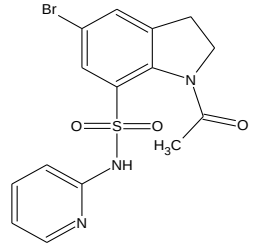	3.3			
13	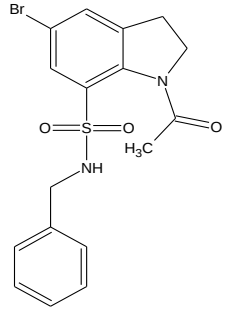	3.3			
14	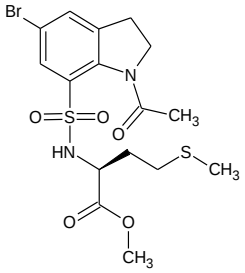	3.4			

Each of these derivatives contains a bromo-indoline group with various hydrophobic R groups such as piperidine, pyrrolidine cyclohexane or diethyl methoxy. Substituting the R group with an isopropol (**4A**), aromatic ring (**7A**) or a bulkier dimethyl moiety (**6A**), or alkyl carboxylic acid groups (**8A**, **9A**, **10**) decreases the inhibitory ability. Surprisingly, the ability of **1A**, **2A**, **3A** and **5** to inhibit DapE is not dependent on whether the compound contains a secondary or tertiary amine adjacent to the sulfone functional group. Therefore, the amine is unlikely serving as a ZBG, which may partially explain the weak affinity for DapE of these compounds. Interestingly, simply substituting the X group of the indoline sulfonamide backbone from bromo to chloro (**1B**, **2B**, **3B**) decreases the inhibitory ability of the compounds by 30% to 83%. Clearly the size and polarizability of this group is important for recognition and binding to DapE.

Shityakov *et al.* [126] recently published a study in which they emphasize the importance of structure-activity relationship studies coupled with computational techniques in order to analyze and confirm experimentally derived inhibitory data, since this approach could be a valuable tool in the future design of potent medicinal lead compounds. In the absence of structural information, SWISSDock was used to explore potential binding modes and predict molecular interactions that may occur between DapE and **1A**.[127] By analyzing the free energy of binding for multiple poses, the best binding model was found where a sulfone oxygen atom bridges between the two Zn(II) ions with the indoline carbonyl moiety binding to Zn2. An alternate pose was also explored where the carbonyl oxygen from the indoline ring bridges between the two zinc ions and the sulfone oxygen binds to Zn2 (Figure 8). While this would be a viable binding mode to the dinuclear Zn(II) active site, the free energy of binding was significantly less negative.

Figure 31. Docking pose for compound 1A. Color depiction: Blue: positive charge; Red: negative charge.

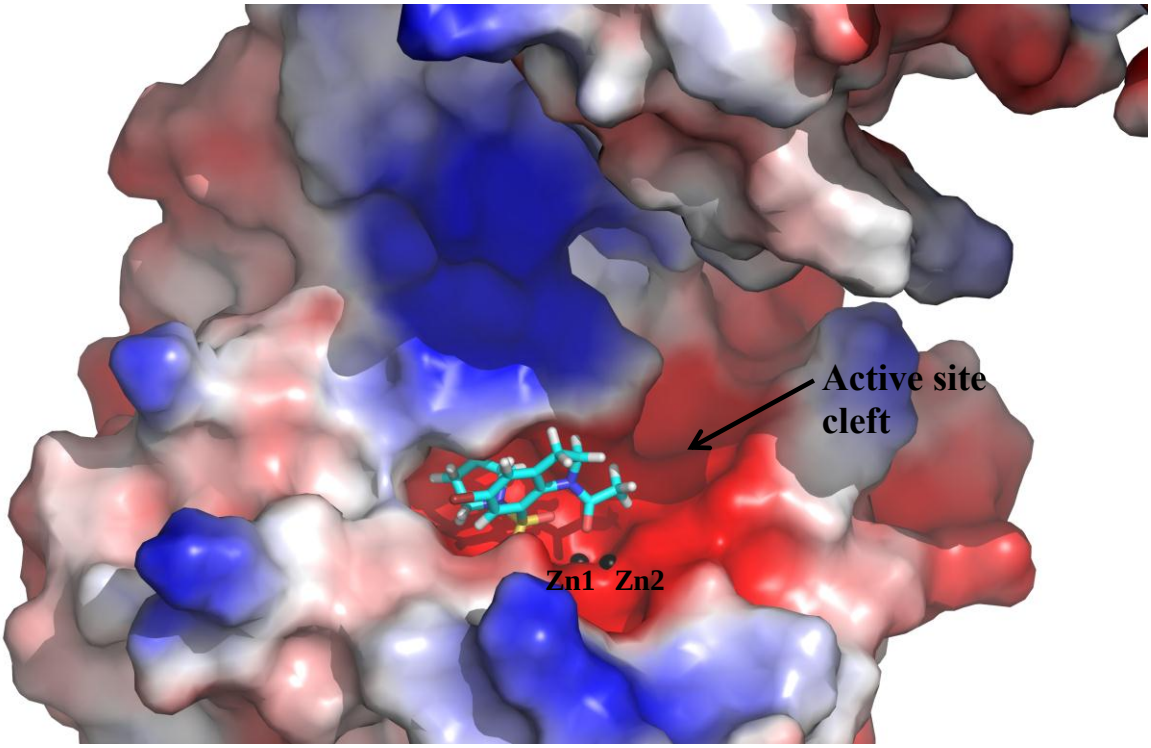

Interestingly, the carbonyl oxygen atom is bound to only Zn2 while the pyrrolidine ring is buried deeper into a hydrophobic pocket within the active site cleft. This binding mode is favorable for inhibitors with less bulky, hydrophobic R groups. This binding pose is consistent with SAR data in that potential inhibitors with bulky, or hydrophilic R groups such as **4A**, **6A**, **7A**, **8A**, **9A**, or **10** either do not inhibit DapE or are significantly weaker inhibitors than **1A**. It is evident from the docking simulations that the compounds with the best inhibitory properties interact with the active site Zn(II) ions as well as active site residues within a smile-shaped cleft that extends along the catalytic domain and surrounds the active site (Figure 31). Therefore, linear structures without large, bulky

groups and with a ZBG, such as the sulfone and/or carbonyl oxygen, would likely bind the best to DapE. Such an inhibitor would also have to contain functional groups that are properly positioned to form hydrogen bonds with active site lysine and arginine groups, such as K135, R258, and R329 that reside in the smile-shaped cleft.

In conclusion, a rapid and reliable enzyme-coupled spectrophotometric assay for DapE has been developed and tested against the previously reported DapE inhibitors L-captopril and L-penicillamine. This enzyme-coupled spectrophotometric assay allowed for HTS studies to be conducted with over 39,000 compounds screened thus far providing five new compounds that showed >20% inhibition, providing strong verification that the newly developed coupled assay for DapE is selective and robust. Four of the five newly identified DapE inhibitors contained a sulfone with two of the five containing an excellent building block, an indoline sulfonamide. Eighteen new compounds were synthesized and the resulting SAR analysis indicated the importance of the sulfone, indoline carbonyl and bromo moieties along with a relatively small, hydrophobic group. Inhibitor docking studies reaffirm the importance of each of these groups and propose a μ-sulfone oxygen-binding mode with a terminal carbonyl oxygen atom. These new medicinal chemistry lead compounds provide insight into the structural determinants of inhibitor binding to the active site of DapE and how active site residues can be advantageously targeted to improve inhibitor binding free energy. Given that multidrug-resistant organisms pose a serious and increasing threat to human health, it is critically important that new antibiotic lead compounds that target enzymes, such as DapE be discovered.

CHAPTER FIVE

CONCLUSION

The overall goal of this research was to obtain valuable information on the catalytic mechanism of DapE enzymes that might ultimately contribute in subjugating the problem of increasing resistance of bacteria. The importance of this project is emphasized by the emergence of bacteria that are resistant to some or all currently available antibiotics. This trend of increasing resistance in bacteria makes today's antibiotics more and more ineffective, thus increasing the need for a new class of antibiotics. One of the approaches to prevent this problem from getting out of control is developing drugs that target essential bacterial biosynthetic pathways. Advances in the area of genomics have influenced the discovery of novel antimicrobial agents greatly. It has provided the ability to scientists to identify essential genes that result in the inhibition of cell growth. This approach has been very useful in selecting the meso-diaminopimelate (mDAP)/lysine biosynthetic pathway, which identifies DapE as a potential target for the development of antimicrobial agents.[26]

In order to accomplish the research objectives in this thesis and gain insight into the catalytic mechanism of DapE along with the determinants of substrate/inhibitor binding, several biochemical and biophysical techniques were employed. These data have provided essential information for rational design of DapE inhibitors, which relies

on understanding of the active site architecture including residues in and around the active site that are important for substrate recognition and binding.

In Chapter 1, the significance of increasing antimicrobial resistance is presented. Despite the critical need for new antibiotics to treat drug-resistant infections the number of new antibiotics approved by the FDA has been declining significantly in the past two decades with only five new antibiotics approved in the last few years.[17] Fortunately, congress together with other health organizations have recognized this growing problem and raised awareness to the urgent need to develop new classes of antibiotics. Policymakers have offered patent extensions as well as various tax breaks, in order to revive interest and make antibiotic research profitable for pharmaceutical companies. One example of this approach is the "10 x `20" initiative, which calls for U.S. and European Union leaders to join forces and develop 10 novel antibiotics by 2020.[21] This is just one of the examples that our government is undertaking to try and restore interest in antibiotic research. Another to approach this problem is to develop drugs that target enzymes, such as DapE, that are present within essential bacterial biosynthetic pathways. This approach should yield inhibitors that may exhibit selective toxicity against bacteria and not humans, since there are no similar biosynthetic pathways in mammals.[27] This research should contribute to benefit the health and general wellbeing of society given that multidrug resistant bacteria pose a serious and increasing threat to human health.

In Chapter 2, I examined the role of the catalytic domain of DapE by preparing truncated DapE enzymes by deleting the dimerization domains of the DapE from *Vibrio cholera* and *H. influenzae* (*Hi*DapE^{T} and *Vc*DapE^{T}). The resulting truncated enzymes,

*Hi*DapE^{T} and *Vc*DapE^{T}, were hypothesized to be very similar to the aminopeptidase from *Aeromonas proteolytica* (AAP), which is a monomeric protein and contains a single catalytic domain.[88b] Interstingly, these studies revealed that removal of the dimerization domain in DapE renders the enzyme inactive. The lack of activity was quite surprising taking into the account that the mutants were folded properly and the overall structure was very similar to WT DapE. Therefore, the truncated mutants were examined using molecular dynamic, X-ray crystallographic, and mutagenesis methods to understand why they were inactive. Analysis of the X-ray crystal structures of *Hi*DapE^{T} and *Vc*DapE^{T} revealed that loop V is much more flexible in the truncated enzymes than WT-DapE due to the lack of interactions provided by the dimerization domain. These data suggest that the dimerization domain restricts the conformational freedom of the loop V region and may contribute residues to the active site environment that are important for substrate recognition and binding. Molecular Dynamic simulations, which were consistent with the crystallographic data, showed that the truncated proteins have greater flexibility in the loop created to replace the dimerization domain and also in the active site loop V. Mutation of T325, a residue that resides on loop V and is positioned directly above the dinuclear active site forming a hydrogen bond with the bridging water molecule, confirmed that the position of loop V is important for the proper organization of active site residues, which are directly to catalysis.[119] Moreover, these data suggested that designing small molecules inhibitors that interact with this active site loop V region as well as the dinuclear metal center might lead to potent DapE inhibitors that can function

as antibacterial agents. Disrupting dimer formation may also be an avenue to explore for the development of potent DapE inhibitors.

In Chapter 3, I investigated the inhibition of L-captopril on the DapE enzymes from *H. influenzae* and *N. meningitidis*. Previous studies have shown that L-captopril is a competitive inhibitor of the DapE from *H. influenzae* (K_i = 3.3μM).[42] L-captopril was found to also be a competitive inhibitor of the DapE form *N. meningitidis* (K_i = 2.8 μM). The electronic properties of the Co(II)-forms of DapE bound by L-captopril was examined using electronic absorption, EPR, and MCD spectroscopies. In the presence of L-captopril, UV-Vis spectra of Co(II)-substituted DapE enzymes revealed a red-shift in the λ_{max} of ~30 nm along with an increase in molar absorptivity, suggesting that L-captopril interacts with both metal ions in the dinuclear active site. EPR and MCD data indicate that the Co(II) ions in [Co_DapE] and [CoCoDapE] are five- and six-coordinate, respectively and are weakly antiferromagnetically coupled upon the addition of L-captopril yielding an S = 0 ground state. These data confirm that L-captopril interacts with both metal ions residing within the active site of DapE and suggest that the thiolate of L-captopril bridges between the two metal ions. Conformation of this proposed structure was derived from EXAFS and X-ray crystallography. EXAFS data clearly indicate the coordination of a thiolate to the dinuclear Zn(II) center of DapE with an increase in the Zn-Zn distance, suggesting a bridging thiolate. The three-dimensional structure of the DapE from *N. meningitidis* bound by L-captopril was solved to 1.78 Å. This is the first structure of any DapE enzyme bound by an exogenous molecule. The structure reveals that the thiolate of L-captopril does, in fact, bridge between the two

Zn(II) ions consistent with the EPR, MCD, and EXAFS data. The results obtained in this study provide new insight into the important determinants of inhibitor binding including active site residues that form hydrogen-bonding interactions. These data are crucial for the rational design and synthesis of potent DapE inhibitors.

In Chapter 4, new medicinal chemistry lead compounds for DapE enzymes were discovered through high-throughput screening (HTS) studies. In order to perform HTS, an enzyme-coupled continuous spectrophotometric assay for DapE was designed and developed. The hydrolysis of N-succinyl-L,L-diaminopimelic acid (SDAP) was coupled to L,L-diaminopimelate aminotransferase (LL-DAP-AT), which can utilize DAP as an amino donor and 2-oxoglutarate (2-OG) as an amino acceptor, to produce tetrahydrodipicolinate (THDP) that when coupled with 2-aminobenzaldehyde (OAB) produces dihydroquinazolium (DHQ), which absorbs at 440 nm. Extensive testing of this assay proved that it was dependent on the hydrolysis reaction catalyzed by DapE. With a viable spectrophotometric assay in hand for DapE, HTS was carried out at the Chemical Genomics Core Facility at Indiana University School of Medicine in collaboration with Professor Ye. More than 39,000 compounds were screened with five inhibiting DapE activity by >20 %, which is a strong verification that the newly developed coupled assay for DapE is selective and robust. Four of these compounds contained either sulfonamide or sulfonyl functional groups, which have not been explored previously as DapE inhibitors. A discontinuous form of this enzyme-coupled assay was also developed to test the inhibition of eighteen newly synthesized sulfonamide derivatives by determining the percent inhibition. Four of the newly synthesized compounds proved to be moderate

inhibitors of DapE. Finally, the best inhibitor was docked into the active site to analyze the important inhibitor-enzyme interactions for the design of new, more potent DapE inhibitors.

The completion of this research provided insight into the determinants of substrate/inhibitor binding to DapE. In addition, new medicinal chemistry lead compounds were discovered and studies were conducted to gains an understanding of their mode of binding to DapE. These data are critical to future studies on the design and synthesis of highly-selective inhibitors of DapE. The discovery of such inhibitors will potentially provide a novel class of antibiotics, which are desperately needed to fight the spread of infectious disease.

REFERENCES

1. Spellberg, B.; Powers, J. H.; Brass, E. P.; Miller, L. G.; Edwards, J. E., Trends in Antimicrobial Drug Development: Implications for the Future. *Clinical Infectious Diseases* **2004,** *38* (9), 1279-1286.

2. Howe, R. A.; Bowker, K. E.; Walsh, T. R.; Feest, T. G.; MacGowan, A. P., Vancomycin-resistant *Staphylococcus aureus*. *Lancet* **1997,** *351*, 601-602.

3. McDolald, L. C.; Kuehnert, M. J.; Tenover, F. C.; Jarvis, W. R., Vancomycin-reststant enterococci outside the health-care setting: prevalence, sources, and public health implications. *Emerg.-Infect. Diseas.* **1997,** *3*, 311-317.

4. Levy, S. B., The challenge of antibiotic resistance. *Sci. Am.* **1998,** *278*, 46-53.

5. Chin, J., Resistance is useless. *New Scientist* **1996,** *152*, 32-35.

6. Morar, M. W. G. D., The Genomic Enzymology of Antibiotic Resistance. *Annual Review of Genetics* **2010,** *44* (1).

7. Hancock, R. E. W., The end of an era? *Nature Reviews Drug Discovery* **2007,** *6* (1).

8. Palumbi, S. R., Humans as the World's Greatest Evolutionary Force. *Science* **2001,** *293* (5536), 1786-1790.

9. Clatworthy, A. E.; Pierson, E.; Hung, D. T., Targeting virulence: a new paradigm for antimicrobial therapy. *Nature chemical biology* **2007,** *3* (9), 541-8.

10. Choffnes, E. R.; Relman, D. A. Antibiotic resistance implications for global health and novel intervention strategies : workshop summary. http://site.ebrary.com/id/10439406.

11. Knobler, S. The resistance phenomenon in microbes and infectious disease vectors implications for human health and strategies for containment : workshop summary.

12. Rice, L. B., Federal Funding for the Study of Antimicrobial Resistance in Nosocomial Pathogens: No ESKAPE. *Journal of Infectious Diseases* **2008,** *197* (8), 1079-1081.

13. Kumarasamy, K. K.; Toleman, M. A.; Walsh, T. R.; Bagaria, J.; Butt, F.; Balakrishnan, R.; Chaudhary, U.; Doumith, M.; Giske, C. G.; Irfan, S.; Krishnan, P.; Kumar, A. V.; Maharjan, S.; Mushtaq, S.; Noorie, T.; Paterson, D. L.; Pearson, A.; Perry, C.; Pike, R.; Rao, B.; Ray, U.; Sarma, J. B.; Sharma, M.; Sheridan, E.; Thirunarayan, M. A.; Turton, J.; Upadhyay, S.; Warner, M.; Welfare, W.; Livermore, D. M.; Woodford, N., Emergence of a new antibiotic resistance mechanism in India, Pakistan, and the UK: a molecular, biological, and epidemiological study. *The Lancet Infectious Diseases* **2010,** *10* (9), 597-602.

14. *Threat Report 2013*; The US Centers f or Disease Control and Prevention (CDC): Washington, DC., 2013.

15. McManus, M. C., Mechanisms of bacterial resistance to antimicrobial agents. *AMERICAN JOURNAL OF HEALTH SYSTEM PHARMACY* **1997,** *54* (12), 1420-1433.

16. Normark Bh, N. S., Evolution and spread of antibiotic resistance. *Journal of internal medicine* **2002,** *252* (2), 91-106.

17. Colson, A., THE ANTIBIOTIC PIPELINE. *Policy Brief 6 for the Disease Dynamics, Economics & Policy: Washington, D.C.,* **2008**.

18. Christoffersen, R. E., Antibiotics[mdash]an investment worth making? *Nat Biotech* **2006,** *24* (12), 1512-1514.

19. Projan, S. J.; Shlaes, D. M., Antibacterial drug discovery: is it all downhill from here? *CLM Clinical Microbiology and Infection* **2004,** *10*, 18-22.

20. Coates, A. R. M.; Hu, Y., Novel approaches to developing new antibiotics for bacterial infections. *British Journal of Pharmacology* **2007,** *152* (8), 1147-1154.

21. The 10 × '20 Initiative: Pursuing a Global Commitment to Develop 10 New Antibacterial Drugs by 2020. *Clinical Infectious Diseases* **2010,** *50* (8), 1081-1083.

22. In *Interagency Task Force on Antimicrobial Resistance (ITFAR): An Update of A Public Health Action Plan to Combat Antimicrobial Resistance,* Centers for Disease Control and Prevention, Washington, DC., Washington, DC., 2011.

23. Goldman, M., Reflections on the Innovative Medicines Initiative. *Nature reviews. Drug discovery* **2011,** *10* (5), 321-322.

24. An Act To amend the Federal Food, Drug, and Cosmetic Act to revise and extend the user-fee programs for prescription drugs and medical devices, to establish user-fee programs for generic drugs and biosimilars, and for other purposes. 112th ed.; 2012.

25. Taylor, P. L.; Wright, G. D., Novel approaches to discovery of antibacterial agents. *Animal Health Research Reviews* **2008,** *9* (Special Issue 02), 237-246.

26. Hutton, C. A.; Perugini, M. A.; Gerrard, J. A., Inhibition of lysine biosynthesis: an evolving antibiotic strategy. *Molecular Biosystems* **2007,** *3* (7), 458-465.

27. Scapin, G.; Blanchard, J. S., Enzymology of bacterial lysine biosyntesis. *Adv. Enzymol.* **1998,** *72*, 279-325.

28. Born, T. L.; Blanchard, J. S., Structure/function studies on enzymes in the diaminopimelate pathway of bacterial cell wall synthesis. *Cur. Opin. Chem. Biol.* **1999,** *3*, 607-613.

29. Born, T. L.; Zheng, R.; Blanchard, J. S., Hydrolysis of N-succinyl-L,-Ldiaminopimelic acid by the *Haemophilus influenzae* dapE-encoded desuccinylase: metal activation, solvent isotope effects, and kinetic mechanism. *Biochemistry* **1998,** *37*, 10478-10487.

30. Henery, C. M., Antibiotic resistance. *C&E News* **2000,** (March 6), 41-58.

31. Miller, J. B., Antibiotics and isotopes. *The Pharma Century* 2000, pp 52-71.

32. Gillner, D. M.; Bienvenue, D. L.; Nocek, B. P.; Joachimiak, A.; Zachary, V.; Bennett, B.; Holz, R. C., The dapE-encoded N-succinyl-L,L-Diaminopimelic Acid Desuccinylase from Haemophilus influenzae Contains two Active Site Histidine Residues. *J. Bio. Inorg. Chem.* **2009,** *14*, 1-10.

33. Cosper, N. J.; Bienvenue, D. L.; Shokes, J.; Gilner, D. M.; Tsukamoto, T.; Scott*, R.; Holz*, R. C., The dapE-encoded N-succinyl-L,L-Diaminopimelic Acid Desuccinylase from Haemophilus influenzae is a Dinuclear Metallohydrolase. *J. Am. Chem. Soc.* **2004,** *125*, 14654-14655.

34. Broder, D. H.; Miller, C. G., DapE can function as an aspartyl peptidase in the presence of Mn2+. *Journal of bacteriology* **2003,** *185* (16), 4748-54.

35. Makarova, K. S.; Grishin, N. V., The Zn-peptidase superfamily: functional convergence after evolutionary divergence. *Journal of Molecular Biology* **1999,** *292* (1), 11-17.

36. Badger, J.; Sauder, J. M.; Adams, J. M.; Antonysamy, S.; Bain, K.; Bergseid, M. G.; Buchanan, S. G.; Buchanan, M. D.; Batiyenko, Y.; Christopher, J. A.; Emtage, S.; Eroshkina, A.; Feil, I.; Furlong, E. B.; Gajiwala, K. S.; Gao, X.; He, D.; Hendle, J.; Huber, A.; Hoda, K.; Kearins, P.; Kissinger, C.; Laubert, B.; Lewis, H. A.; Lin, J.; Loomis, K.; Lorimer, D.; Louie, G.; Maletic, M.; Marsh, C. D.; Miller, I.; Molinari, J.; Muller-Dieckmann, H. J.; Newman, J. M.; Noland, B. W.; Pagarigan, B.; Park, F.; Peat, T. S.; Post, K. W.; Radojicic, S.; Ramos, A.; Romero, R.; Rutter, M. E.; Sanderson, W. E.; Schwinn, K. D.; Tresser, J.; Winhoven, J.; Wright, T. A.; Wu, L.; Xu, J.; Harris, T. J., Structural analysis of a set of proteins resulting from a bacterial genomics project. *Proteins* **2005,** *60*, 787-796.

37. Nocek, B. P.; Gillner, D. M.; Fan, Y.; Holz, R. C.; Joachimiak, A., Structural Basis for Catalysis by the Mono- and Dimetalated Forms of the dapE-Encoded N-succinyl-l,l-Diaminopimelic Acid Desuccinylase. *J Mol Biol* **2010,** *397* (3), 617-626.

38. Davis, R.; Bienvenue, D.; Swierczek, S. I.; Gilner, D. M.; Rajagopal, L.; Bennett, B.; Holz, R. C., Kinetic and spectroscopic characterization of the E134A- and E134D-altered dapE-encoded N-succinyl-L,L-diaminopimelic acid desuccinylase from Haemophilus influenzae. *J Biol Inorg Chem.* **2006,** *11*, 206-16.

39. Chevrier, B.; Schalk, C.; D'Orchymont, H.; Rondeau, J.-M.; Moras, D.; Tarnus, C., Crystal structure of Aeromonas proteolytica aminopeptidase: a prototypical member of the co-catalytic zinc enzyme family. *Structure* **1994,** *2* (4), 283-291.

40. Greenblatt, H. M.; Almog, O.; Maras, B.; Spungin-Bialik, A.; Barra, D.; Blumberg, S.; Shoham, G., *Streptomyces griseus* Aminopeptidase: X-ray crystallographic structure at 1.5A resolution. *J. Mol. Biol.* **1997,** *265*, 620-636.

41. (a) Ustynyuk, L.; Bennett, B.; Edwards, T.; Holz, R. C., Inhibition of the Aminopeptidase from *Aeromonas proteolytica* by Aliphatic Alcohols. Characterization of the Hydrophobic Substrate Recognition Site. *Biochemistry* **1999,** *38*, 11433-11439; (b) Stamper, C.; Bienvenue, D.; Moulin, A.; Bennett, B.; Ringe, D.; Petsko, G.; Holz, R. C., Spectroscopic and X-ray Crystallographic Characterization of the Bestatin Bound Form of the Aminopeptidase from Aeromonas proteolytica. *Biochemistry* **2004,** *43*, 9620-9628.

42. Gillner, D. M.; Armush, N.; Holz, R. C.; Becker, D., Inhibitors of Bacterial N-Succinyl-L,L-diaminopimelic Acid Desuccinylase (DapE) and Demonstration of in vitro Antimicrobial Activity. *Bioorg. Med. Chem. Lett.* **2009,** *19*, 6350-6352.

43. Andrykovitch, M.; Routzahn, K. M.; Li, M.; Gu, Y.; Waugh, D. S.; Ji, X., Characterization of four orthologs of stringent starvation protein A. *Acta Crystallographica Section D* **2003,** *59* (5), 881-886.

44. Nemecek, S., Beating Bacteria. New ways to fend off antibiotic-resistant pathogens. *Sci. Am.* **1997,** *276*, 38-39.

45. Spellberg, B.; Powers, J. H.; Brass, E. P.; Miller, L. G.; Edwards Jr., J. E., Trends in antimicrobial drug development: implications for the future. *Clin Infect Dis* **2004,** *38*, 1279–1286.

46. Walsh, C., *Antibiotics : actions, origins, resistance*. ASM Press: Washington, D.C., 2003.

47. Butler, M. B. A., Natural products The future scaffolds for novel antibiotics? *Biochemical Pharmacology Biochemical Pharmacology* **2006,** *71* (7), 919-929.

48. Zappia, G.; Menendez, P.; Monache, G. D.; Misiti, D.; Nevola, L.; Botta, B., The contribution of oxazolidinone frame to the biological activity of pharmaceutical drugs and natural products. *Mini reviews in medicinal chemistry* **2007,** *7* (4), 389-409.

49. Hair, P. K. S., Daptomycin: A Review of its Use in the Management of Complicated Skin and Soft-Tissue Infections and Staphylococcus aureus Bacteraemia. *Drugs* **2007,** *67* (10), 1483-1512.

50. Howe, R. A.; Bowker, K. E.; Walsh, T. R.; Feest, T. G.; MacGowan, A. P., Vancomycin-Resistant *Staphylococcus aureus*. *Lancet* **1998,** *351*, 601-602.

51. Miller, J. R.; Dunham, S.; Mochalkin, I.; Banotai, C.; Bowman, M.; Buist, S.; Dunkle, B.; Hanna, D.; Harwood, H. J.; Huband, M. D.; Karnovsky, A.; Kuhn, M.; Limberakis, C.; Liu, J. Y.; Mehrens, S.; Mueller, W. T.; Narasimhan, L.; Ogden, A.; Ohren, J.; Prasad, J. V.; Shelly, J. A.; Skerlos, L.; Sulavik, M.; Thomas, V. H.; VanderRoest, S.; Wang, L.; Wang, Z.; Whitton, A.; Zhu, T.; Stover, C. K., A Class of Selective Antibacterials Derived from a Protein Kinase Inhibitor Pharmacophore. *Proc Natl Acad Sci U S A.* **2009,** *106* (6), 1737-1742.

52. Hutton, C. A.; Peruginibc, M. A.; Gerrard, J. A., Inhibition of Lysine Biosynthesis: An Evolving Antibiotic Strategy. *Mol. BioSyst.* **2007,** *3*, 458–465.

53. Born, T. L.; Zheng, R.; Blanchard, J. S., Hydrolysis of *N*-succinyl-L,-L-Diaminopimelic Acid by the *Haemophilus influenzae dapE*-Encoded Desuccinylase: Metal Activation, Solvent Isotope Effects, and Kinetic Mechanism. *Biochemistry* **1998,** *37*, 10478-10487.

54. Girodeau, J.-M.; Agouridas, C.; Masson, M.; R., P.; LeGoffic, F., The lysine pathway as a target for a new genera of synthetic antibacterial antibiotics? *J. Med. Chem.* **1986,** *29*, 1023-1030.

55. (a) Karita, M.; Etterbeek, M. L.; Forsyth, M. H.; Tummuru, M. R.; Blaser, M. J., Characterization of *Helicobacter pylori* dapE and construction of a conditionally lethal dapE mutant. *Infect. Immun.* **1997,** *65*, 4158-4164; (b) Pavelka, M. S.; Jacobs, W. R., Biosynthesis of diaminopimelate, the precursor of lysine and a component of peptidoglycan, is an essential function of *Mycobacterium smegmatis*. *J. Bacteriol.* **1996,** *178*, 6496-6507.

56. Bouvier, J.; Richaud, C.; Higgins, W.; Bögler, O.; Stragier, P., Cloning, characterization, and expression of the dapE gene of *Escherichia coli*. *J. Bacteriol.* **1992,** *174*, 5265-5271.

57. Fuchs, T. O.; Schneider, B.; Krumbach, K.; Eggeling, L.; Gross, R., Characterization of the *Bordetella pertussis* diaminopimelate (DAP) biosynthesis locus identifies dapC, a novel gene coding for an N-succinyl-L,L-DAP aminotransferase. *J. Bacteriol.* **2000,** *182*, 3626-3631.

58. Shaw-Reid, C. A.; McCormick, M. M.; Sinskey, A. J.; Stephanopoulos, G., Flux through the tetrahydrodipicolinate succinylase pathway is dispensible for L-lysine production in *Corynebacterium glutamicum*. *Appl. Microbiol. Biotechnol.* **1999,** *51*, 325-333.

59. Lin, Y.; Myhrman, R.; Schrag, M. L.; Gelb, M. H., Bacterial N-succinyl-L-diaminopimelic acid desuccinylase. Purification, partial characterization, and substrate specificity. *J. Biol. Chem.* **1988,** *263*, 1622-1627.

60. Boucher, H. W.; Talbot, G. H.; Bradley, J. S.; Edwards, J. E.; Gilbert, D.; Rice, L. B.; Scheld, M.; Spellberg, B.; Bartlett, J., Bad Bugs, No Drugs: No ESKAPE! An Update from the Infectious Diseases Society of America. *Clinical Infectious Diseases* **2009,** *48* (1), 1-12.

61. Gillner, D. M.; Bienvenue, D. L.; Nocek, B. P.; Joachimiak, A.; Zachary, V.; Bennett, B.; Holz, R. C., The *dapE*-Encoded *N*-Succinyl-L,L-Diaminopimelic Acid Desuccinylase from *Haemophilus influenzae* Contains two Active Site Histidine Residues. *J. Biol. Inorg. Chem.* **2009,** *14*, 1-10.

62. Barrett, A. J.; Rawlings, N. D.; Woessner, J. F., *Handbook of proteolytic enzymes*. Academic Press: London, 1998; p 1-1666.

63. Nocek, B. P.; Gillner, D. M.; Fan, Y.; Holz, R. C.; Joachimiak, A., Structural Basis for Catalysis by the Mono- and Dimetalated Forms of the *dapE*-Encoded *N*-succinyl-L,L-Diaminopimelic Acid Desuccinylase. *J. Mol. Biol.* **2010,** *397* (3), 617-626.

64. (a) Rowsell, S.; Pauptit, R. A.; Tucker, A. D.; Melton, R. G.; Blow, D. M.; Brick, P., Crystal structure of carboxypeptidase G2, a bacterial enzyme with applications in

cancer therapy. *Structure* **1997,** *5*, 337-347; (b) Desmarais, W.; Bienvenue, D. L.; Bzymek, K. P.; Petsko, G. A.; Ringe, D.; Holz, R. C., The High-Resolution Structures of the Neutral and the Low pH Crystals of the Aminopeptidase from *Aeromonas proteolytica*. *J. Biol. Inorg. Chem.* **2006,** *11*, 398-408.

65. Kim, Y.; Babnigg, G.; Jedrzejczak, R.; Eschenfeldt, W. H.; Li, H.; Maltseva, N.; Hatzos-Skintges, C.; Gu, M.; Makowska-Grzyska, M.; Wu, R.; An, H.; Chhor, G.; Joachimiak, A., High-throughput protein purification and quality assessment for crystallization. *Methods* **2011,** *55* (1), 12-28.

66. Nocek, B.; Stein, A. J.; Jedrzejczak, R.; Cuff, M. E.; Li, H.; Volkart, L.; Joachimiak, A., Structural Studies of ROK Fructokinase YdhR from Bacillus subtilis: Insights into Substrate Binding and Fructose Specificity. *J Mol Biol* **2011,** *406* (2), 325-342.

67. (a) Bergmann, M.; Stein, W. H., Naphthalene-b-sulfonic acid as a reagent for amino acids. *J. Biol. Chem.* **1939,** *129*, 609-618; (b) Bienvenue, D. L.; Gilner, D. M.; Davis, R. S.; Bennett, B.; Holz, R. C., Substrate Specificity, Metal Binding Properties, and Spectroscopic Characterization of the dapE-encoded-N-succinyl-L,L-Diaminopimelic Acid Desuccinylase from Haemophilus influenzae. *Biochemistry* **2003,** *42*, 10756-10763.

68. Adams, P. D.; Afonine, P. V.; Bunkóczi, G.; Chen, V. B.; Davis, I. W.; Echols, N.; Headd, J. J.; Hung, L.-W.; Kapral, G. J.; Grosse-Kunstleve, R. W.; McCoy, A. J.; Moriarty, N. W.; Oeffner, R.; Read, R. J.; Richardson, D. C.; Richardson, J. S.; Terwilliger, T. C.; Zwart, P. H., PHENIX: a comprehensive Python-based system for macromolecular structure solution. *Acta Crystallographica Section D: Biological Crystallography* **2010,** *66* (2), 213-221.

69. (a) Vagin, A.; Teplyakov, A., An approach to multi-copy search in molecular replacement. *Acta Crystallogr D Biol Crystallogr* **2000,** *56* (Pt 12), 1622-4; (b) The CCP4 suite: programs for protein crystallography. *Acta Crystallogr D Biol Crystallogr* **1994,** *50* (Pt 5), 760-3.

70. Murshudov, G. N.; Vagin, A. A.; Dodson, E. J., Refinement of macromolecular structures by the maximum-likelihood method. *Acta Crystallogr D Biol Crystallogr* **1997,** *53* (Pt 3), 240-55.

71. Humphrey, W.; Dalke, A.; Schulten, K., VMD: Visual molecular dynamics. *J. Mol. Graphics* **1996,** *14*, 33.

72. Jorgensen, W. L.; Chandrasekhar, J.; Madura, J. D.; Impey, R. W.; Klein, M. L., Comparison of simple potential functions for simulating liquid water. *J. Chem. Phys.* **1983,** *79*, 926-935.

73. MacKerell Jr., A. D.; Banavali, N.; Foloppe, N., Development and current status of the CHARMM force field for nucleic acids. *Biopolymers* **2001,** *56* 257–265.

74. Phillips, J. C.; Braun, R.; Wang, W.; Gumbart, J.; Tajkhorshid, E.; Villa, E.; Chipot, E.; Skeel, R. D.; Kale, L.; Schulten, K., Scalable molecular dynamics with NAMD. *J. Comp. Chem.* **2005,** *26*, 1781-1802.

75. Guex N, P. M. C., SWISS-MODEL and the Swiss-PdbViewer: an environment for comparative protein modeling. *Electrophoresis* **1997,** *18* (15), 2714-23.

76. Arnold, K.; Bordoli, L.; Kopp, J.; Schwede, T., The SWISS-MODEL Workspace: A web-based environment for protein structure homology modelling. *Bioinformatics* **2006,** *22*, 195-201.

77. Koradi, R.; Billeter, M.; Wuthrich, K., MOLMOL: A program for display and analysis of macromolecular structures. *J. Mol. Graphics* **1996,** *14*, 51-55.

78. Whitmore, L. W. B. A., DICHROWEB, an online server for protein secondary structure analyses from circular dichroism spectroscopic data. *Nucleic acids research* **2004,** *32* (Supplement), 668.

79. (a) Chevrier, B.; Schalk, C.; D'Orchymont, H.; Rondeau, J.-M.; Moras, D.; Tarnus, C., Crystal Structure of *Aeromonas proteolytica* Aminopeptidase: A Prototypical Member of the Co-Catalytic Zinc Enzyme Family. *Structure* **1994,** *2* (4), 283-291; (b) Greenblatt, H. M.; Almog, O.; Maras, B.; Spungin-Bialik, A.; Barra, D.; Blumberg, S.; Shoham, G., *Streptomyces griseus* Aminopeptidase: X-ray Crystallographic Structure at 1.75 A Resolution. *J. Mol. Biol.* **1997,** *265*, 620-636.

80. Chevrier, B.; D'Orchymont, H.; Schalk, C.; Tarnus, C.; Moras, D., The structure of the *Aeromonas proteolytica* aminopeptidase complexed with a hydroxamate inhibitor. Involvement in catalysis of Glu151 and two zinc ions of the cocatalytic unit. *Eur. J. Biochem.* **1996,** *237*, 393-398.

81. Cosper, N. J.; Bienvenue, D. L.; Shokes, J. E.; Gilner, D. M.; Tsukamoto, T.; Scott, R.; Holz, R. C., The dapE-Encoded *N*-succinyl-L,L-Diaminopimelic Acid Desuccinylase from H*aemophilus influenzae* is a Dinuclear Metallohydrolase. *J. Am. Chem. Soc.* **2003,** *125*, 14654-14655.

82. Lindner, H. A.; Lunin, V. V.; Alary, A.; Hecker, R.; Cygler, M.; Ménard, R., Essential Roles of Zinc Ligation and Enzyme Dimerization for Catalysis in the Aminoacylase-1/M20 Family. *Journal of Biological Chemistry* **2003,** *278* (45), 44496-44504.

83. Griffin, M. D. W.; Dobson, R. C. J.; Pearce, F.; Grant, A.; Laurence, W. A. E.; Liew, C. K.; Mackay, J. P.; Trewhella, J.; Jameson, G. B.; Perugini, M. A.; Gerrard, J. A., Evolution of Quaternary Structure in a Homotetrameric Enzyme. *YJMBI Journal of Molecular Biology* **2008,** *380* (4), 691-703.

84. Girish, T. S.; Gopal, B., Crystal Structure of Staphylococcus aureus Metallopeptidase (Sapep) Reveals Large Domain Motions between the Manganese-bound and Apo-states. *Journal of Biological Chemistry* **2010,** *285* (38), 29406-29415.

85. Abraham, E. P.; Chain, E.; Fletcher, C. M.; Gardner, A. D.; Heatley, N. G.; Jennings, M. A.; Florey, H. W., FURTHER OBSERVATIONS ON PENICILLIN. *The Lancet* **1941,** *238* (6155), 177-189.

86. Davies J, D. D., Origins and evolution of antibiotic resistance. *Microbiol. Mol. Biol. Rev. Microbiology and Molecular Biology Reviews* **2010,** *74* (3), 417-433.

87. Supuran, C. T.; Scozzafava, A.; Clare, B. W., Bacterial Protease Inhibitors. *Med. Res. Revs.* **2002,** *22*, 329-372.

88. (a) Gillner, D. M.; Becker, D. P.; Holz, R. C., Lysine biosynthesis in bacteria: a metallodesuccinylase as a potential antimicrobial target. *Journal of biological inorganic chemistry : JBIC : a publication of the Society of Biological Inorganic Chemistry* **2013,** *18* (2), 155-63; (b) Desmarais, W.; Bienvenue, D. L.; Bzymek, K. P.; Petsko, G. A.; Ringe, D.; Holz, R. C., The 0.95 Å Resolution and Low pH Crystal Structures of the Aminopeptidase from *Aeromonas proteolytica*. *J Biol Inorg Chem.* **2006,** *11*, 398-408.

89. Nocek, B.; Starus, A.; Makowska-Grzyska, M.; Gutierrez, B.; Sanchez, S.; Jedrzejczak, R.; Mack, J. C.; Olsen, K. W.; Joachimiak, A.; Holz, R. C., The Dimerization Domain in DapE Enzymes Is required for Catalysis. *PLoS ONE* **2014,** *9* (5), e93593.

90. Aslanidis C, d. J. P. J., Ligation-independent cloning of PCR products (LIC-PCR). *Nucleic acids research* **1990,** *18* (20), 6069-74.

91. Kim, Y.; Babnigg, G.; Jedrzejczak, R.; Eschenfeldt, W. H.; Li, H.; Maltseva, N.; Hatzos-Skintges, C.; Gu, M.; Makowska-Grzyska, M.; Wu, R.; An, H.; Chhor, G.; Joachimiak, A., High-throughput protein purification and quality assessment for crystallization. *Methods Methods* **2011,** *55* (1), 12-28.

92. Gillner, D.; Armoush, N.; Holz, R. C.; Becker, D. P., Inhibitors of bacterial N-succinyl-l,l-diaminopimelic acid desuccinylase (DapE) and demonstration of in vitro antimicrobial activity. *Bioorg Medicinal Chem Letter* **2009,** *19* (22), 6350-6352.

93. D'souza, V. M.; Holz, R. C., The Methionyl Aminopeptidase from *Escherichia coli* is an Iron(II) Containing Enzyme. *Biochemistry* **1999,** *38*, 11079-11085.

94. Riley, M. J., VTVH 2.1.1 Program for the Simulation and Fitting Variable Temperature−Variable Field MCD Spectra. *The University of Queensland: Brisbane, Australia* **2008**.

95. Ely, F.; Hadler, K. S.; Mitic, N.; Gahan, L. R.; Ollis, D. L.; Plugis, N. M.; Russo, M. T.; Larrabee, J. A.; Schenk, G., Electronic and geometric structures of the organophosphate-degrading enzyme from Agrobacterium radiobacter (OpdA). *Journal of biological inorganic chemistry : JBIC : a publication of the Society of Biological Inorganic Chemistry* **2011,** *16* (5), 777-87.

96. Paulat, F. L. N., Detailed Assignment of the Magnetic Circular Dichroism and UVvis Spectra of Five-Coordinate High-Spin Ferric [Fe(TPP)(Cl)]. *Inorganic Chemistry* **2008,** *47* (11).

97. Argonne National, L., Crystal structure of aminopeptidase N from human pathogen Neisseria meningitides. *Proteins: Struct. Function Bioinform* **2008,** *70* (1).

98. Emsley, P. C. K., Coot: model-building tools for molecular graphics. *Acta Crystallographica Section D: Biological Crystallography* **2004,** *60* (12-1), 2126-2132.

99. Murshudov, G. N.; Vagin, A. A.; Dodson, E. J., Refinement of Macromolecular Structures by the Maximum-Likelihood Method. *AYD Acta Crystallographica Section D* **1997,** *53* (3), 240-255.

100. Laskowski, R. A.; MacArthur, M. W.; Moss, D. S.; Thornton, J. M., PROCHECK: a program to check the stereochemical quality of protein structures. *JCR Journal of Applied Crystallography* **1993,** *26* (2), 283-291.

101. Davis, I. W.; Leaver-Fay, A.; Chen, V. B.; Block, J. N.; Kapral, G. J.; Wang, X.; Murray, L. W.; Arendall, W. B.; Snoeyink, J.; Richardson, J. S.; Richardson, D. C., MolProbity: all-atom contacts and structure validation for proteins and nucleic acids. *Nucleic acids research* **2007,** *35* (Web Server issue), 375-83.

102. Eufri, D. S. A., Smile - Shaded Molecular imaging on low-cost equipment. *Journal of Molecular Graphics Journal of Molecular Graphics* **1989,** *7* (3), 184-184.

103. Cleland, W. W., Steady state kinetics. *Methods Enzymol.* **1979,** *63*, 103-138.

104. Bertini, I.; Luchinat, C., High-spin cobalt(II) as a probe for the investigation of metalloproteins. *Adv. Inorg. Biochem.* **1984,** *6*, 71-111.

105. Bennett, B., EPR of Cobalt-Substituted Zinc Enzymes. In Metals in Biology: Applications of High Resolution EPR to Metalloenzymes. . *Biol. Magn. Reson.* **2010,** *29*, 345-370.

106. (a) Larrabee, J. A.; Riley, M. J., Magnetic circular dichroism. In Handbook of Dinuclear Metallohyrolases: Structure, Function, Mechanism and Application. *Bentham Science Publishers* **submitted**; (b) Kaden, T. A.; Holmquist, B.; Vallee, B. L., Magnetic circular dichroism of cobalt(II) complexes. *Inorganic Chemistry* **1974,** *13* (11), 2585-2590; (c) Larrabee, J. A.; Alessi, C. M.; Asiedu, E. T.; Cook, J. O.; Hoerning, K. R.; Klingler, L. J.; Okin, G. S.; Santee, S. G.; Volkert, T. L., Magnetic circular dichroism spectroscopy as a probe of geometric and electronic structure of cobalt(II)-substituted proteins: Ground-state zero-field splitting as a coordination number indicator. *J. Am. Chem. Soc.* **1997,** *119*, 4182-4196.

107. (a) Harding, M. J. B. B., The electronic absorption and magnetic circular dichroism spectra of cobalt (II) bromate hexahydrate. *Molecular Physics* **1973,** *25* (4), 745-776; (b) Daumann, L. J.; Comba, P.; Larrabee, J. A.; Schenk, G.; Stranger, R.; Cavigliasso, S.; German, G.; Lawrence, R., Synthesis, Magnetic Properties, and Phosphoesterase Activity of Dinuclear Cobalt(II) Complexes. *Inorganic Chemistry* **2013,** *52* (4).

108. (a) Larrabee, J. A.; Chyun, S.-A.; Volwiler, A. S., Magnetic Circular Dichroism Study of a Dicobalt(II) Methionine Aminopeptidase/Fumagillin Complex and Dicobalt II−II and II−III Model Complexes†. *Inorganic Chemistry* **2008,** *47* (22), 10499-10508; (b) Larrabee, J. A.; Johnson, W. R.; Volwiler, A. S., Magnetic Circular Dichroism Study of a Dicobalt(II) Complex with Mixed 5- and 6-Coordination: A Spectroscopic Model for Dicobalt(II) Hydrolases. *Inorganic Chemistry* **2009,** *48* (18), 8822-8829.

109. Badger, J.; Sauder, J. M.; Adams, J. M.; Antonysamy, S.; Bain, K.; Bergseid, M. G.; Buchanan, S. G.; Buchanan, M. D.; Batiyenko, Y.; Christopher, J. A.; Emtage, S.; Eroshkina, A.; Feil, I.; Furlong, E. B.; Gajiwala, K. S.; Gao, X. H. D.; Hendle, J.; Huber, A.; Hoda, K.; Kearins, P.; Kissinger, C.; Laubert, B.; Lewis, H. A.; Lin, J.; Loomis, K.; Lorimer, D.; Louie, G.; Maletic, M.; Marsh, C. D.; Miller, I.; Molinari, J.; Muller-Dieckmann, H. J.; Newman, J. M.; Noland, B. W.; Pagarigan, B.; Park, F.; Peat, T. S.; Post, K. W.; Radojicic, S.; Ramos, A.; Romero, R.; Rutter, M. E.; Sanderson, W. E.; Schwinn, K. D.; Tresser, J.; Winhoven, J.; Wright, T. A.; Wu, L.; Xu, J.; Harris, T. J., Structural analysis of a set of proteins resulting from a bacterial genomics project. *Proteins* **2005,** *60* (4), 787-96.

110. Jacobsen, F. E.; Lewis, J. A.; Cohen, S. M., The Design of Inhibitors for Medically Relevant Metalloproteins. *ChemMedChem* **2007,** *2*, 152-171.

111. Uda, N. R.; Upert, G.; Angelici, G.; Nicolet, S.; Schmidt, T.; Schwede, T.; Creus, M., Zinc-selective inhibition of the promiscuous bacterial amide-hydrolase DapE:

implications of metal heterogeneity for evolution and antibiotic drug design. *Metallomics* **2013**.

112. Makinen, M. W.; Yim, M. B., Coordination environment of the active-site metal ion of liver alcohol dehydrogenase. *Proc. Natl. Acad. Sci. USA* **1981,** *78*, 6221-6225.

113. (a) Turpeinen, U.; Ahlgren, M.; Hämäläinen, R., Structures of di-m-acetato-(O,O')-m-aqua-bis[acetato(N,N,N',N'-tetramethylethylenediamine)cobalt(II) and m-aqua-di-m-chloroacetato-(O,O')-bis[chloroacetato(N,N,N',N'-tetramethylethylenediamine)cobalt(II). *Acta Cryst.* **1982,** *B32*, 1580-1583; (b) Chaudhuri, P.; Ouerbach, J.; Wieghardt, K.; Nuber, B.; Weiss, J., Synthesis, electrochemistry, and magnetic properties of binuclear cobalt complexes containing the Co_2(m-X)(m-carboxylato)$_2^{+n}$ core (X=OH, Cl, or Br; n=1-3). *J. Chem. Dalton Trans.* **1990**, 271-278.

114. (a) Chen, G.; Edwards, T.; D'souza, V. M.; Holz, R. C., Mechanistic studies on the aminopeptidase from Aeromonas proteolytica: A two-metal ion mechanism for peptide hydrolysis. *Biochemistry* **1997,** *36*, 4278-4286; (b) Lowther, W. T.; Matthews, B. W., Metalloaminopeptidases: Common Functional Themes in Disparate Structural Suroundings. *Chem. Rev.* **2002,** *102*, 4581-4607.

115. C.D.C., Hospital infection control practices advisory committee's recommendations for preventing the spread of vancomycin resistance. *MMWR Morb. Mortal. Wkly Rep.* **1995,** *44*, 1-13.

116. Miller, J. R.; Dunham, S.; Mochalkin, I.; Banotai, C.; Bowman, M.; Buist, S.; Dunkle, B.; Hanna, D.; Harwood, H. J.; Huband, M. D.; Karnovsky, A.; Kuhn, M.; Limberakis, C.; Liu, J. Y.; Mehrens, S.; Mueller, W. T.; Narasimhan, L.; Ogden, A.; Ohren, J.; Prasad, J. V. N. V.; Shelly, J. A.; Skerlos, L.; Sulavik, M.; Thomas, V. H.; VanderRoest, S.; Wang, L.; Wang, Z.; Whitton, A.; Zhu, T.; Stover, C. K., A class of selective antibacterials derived from a protein kinase inhibitor pharmacophore. *Proc Natl Acad Sci U S A.* **2009,** *106* (6), 1737-1742.

117. (a) Arfin, S. M.; Kendall, R. L.; Hall, L.; Weaver, L. H.; Stewart, A. E.; Matthews, B. W.; Bradshaw, R. A., Eukaryotic methionyl aminopeptidases: Two classes of cobalt-dependent enzymes. *Proc. Natl. Acad. Sci. USA* **1995,** *92*, 7714-7718; (b) Ben-Bassat, A.; Bauer, A.; Chang, S.-Y.; Myambo, K.; Boosman, A.; Chang, S., Processing of the initiation methionine from proteins: properties of the Escherichia coli methionine aminopeptidase and its gene structure. *J. Bacteriol.* **1987,** *169*, 751-757; (c) Ben-Bassat, A.; Bauer, K., Amino-terminal processing of proteins. *Nature* **1987,** *326*, 315; (d) Chang, S.-Y. P.; McGary, E. C.; Chang, S., Methionine Aminopeptidase gene of *Escherichia coli* is essential for cell growth. *J. Bacteriol* **1989,** *171, No. 7* (July 1989), 4071-4072; (e) Gonzales, T.; Bobert-Baudouy, J., Bacterial aminopeptidases: Properties and functions. *FEMS Microbiol. Rev.* **1996,** *18*, 319-344; (f) Taylor, A., Aminopeptidases: structure and function. *FASEB J.* **1993,** *7*, 290-298; (g) Taylor, A., Aminopeptidases: towards a

mechanism of action. *TIBS* **1993,** *18*, 167-172; (h) Taylor, A., *Aminopeptidases*. R. G. Landes Co.: Austin, TX USA, 1996; p 1-219.

118. (a) Wang, J.; Sheppard, G. S.; Lou, P.; Kawai, M.; Park, C.; Egan, D. A.; Schneider, A.; Bouska, J.; Lesniewski, R.; Henkin, J., Physiologically relevant metal cofactor for methionine aminopeptidase-2 is manganese. 2003; Vol. 42, pp 5035 - 5042; (b) Huang, M.; Xie, S. X.; Ma, Z. Q.; Huang, Q. Q.; Nan, F. J.; Ye, Q. Z., Inhibition of Monometalated Methionine Aminopeptidase: Inhibitor Discovery and Crystallographic Analysis. 2007; (c) Ma, Z.-Q.; Xie, S.-X.; Huang, Q.-Q.; Nan, F.-J.; Hurley, T.; Ye, Q.-Z., Structural analysis of inhibition of E. coli methionine aminopeptidase: implication of loop adaptability in selective inhibition of bacterial enzymes. *BMC Struc. Biol.* **2007,** *7* (1), 84.

119. Nocek, B.; Starus, A.; Makowska-Grzyska, M.; Gutierrez, B.; Sanchez, S.; Jedrzejczak, R.; Mack, J. C.; Olsen, K. W.; Joachimiak, A.; Holz, R. C., The Dimerization Domain in DapE Enzymes Is required for Catalysis. *PLoS ONE* **2014,** *9* (5), 93593.

120. Watanabe, N.; Cherney, M. M.; van Belkum, M. J.; Marcus, S. L.; Flegel, M. D.; Clay, M. D.; Deyholos, M. K.; Vederas, J. C.; James, M. N. G., Crystal Structure of ll-Diaminopimelate Aminotransferase from Arabidopsis thaliana: A Recently Discovered Enzyme in the Biosynthesis of l-Lysine by Plants and Chlamydia. *Journal of Molecular Biology Journal of Molecular Biology* **2007,** *371* (3), 685-702.

121. Hudson, A. O.; Singh, B. K.; Leustek, T.; Gilvarg, C., An LL-diaminopimelate aminotransferase defines a novel variant of the lysine biosynthesis pathway in plants. *Plant physiology* **2006,** *140* (1), 292-301.

122. Zhang, J. H.; Chung, T. D.; Oldenburg, K. R., A Simple Statistical Parameter for Use in Evaluation and Validation of High Throughput Screening Assays. *J Biomol Screen* **1999,** *4* (2), 67-73.

123. Drews, J., Drug Discovery: A Historical Perspective. *Science* **2000,** *287* (5460).

124. Syed Shoaib Ahmad Shah, G. R. M. A., Recent Advances in Medicinal Chemistry of Sulfonamides. Rational Design as Anti-Tumoral, Anti-Bacterial and Anti-inflammatory Agents. *Mini-Reviews in Medicinal Chemistry* **2013,** *13* (1), 70-86.

125. (a) Fan, C.; Clay, M. D.; Deyholos, M. K.; Vederas, J. C., Exploration of inhibitors for diaminopimelate aminotransferase. *Bioorganic & Medicinal Chemistry Bioorganic & Medicinal Chemistry* **2010,** *18* (6), 2141-2151; (b) Fan, C.; Vederas, J. C., Synthesis and structure-activity relationships of o-sulfonamido-arylhydrazides as inhibitors of LL-diaminopimelate aminotransferase (LL-DAP-AT). *Organic & biomolecular chemistry* **2012,** *10* (30), 5815-9.

126. Shityakov, S.; Broscheit, J.; Puskás, I.; Roewer, N.; Foerster, C., Three-dimensional quantitative structure–activity relationship and docking studies in a series of anthocyanin derivatives as cytochrome P450 3A4 inhibitors. *AABC Advances and Applications in Bioinformatics and Chemistry* **2014**, 11.

127. Grosdidier, A.; Zoete, V.; Michielin, O., SwissDock, a protein-small molecule docking web service based on EADock DSS. *Nucleic Acids Research Nucleic Acids Research* **2011,** *39* (suppl), W270-W277.

VITA

Anna Starus was born and raised in Ełk, Poland. She moved to the United States at the age of 14. Anna excelled in academics and graduated from McHenry High School with Honors while enjoying learning English and a new culture. Later, she attended Loyola University Chicago where she earned a Bachelor of Science in Chemistry, with emphasis in Biochemistry and a Minor in Biology, Magna cum laude, in 2008. While at Loyola, Anna served as the President of the Chemistry Graduate Student Association. In 2012 Anna was awarded the Arthur J. Schmitt Dissertation Fellowship. She also served as a Public Relations officer at the Polish Student Association. As an undergraduate student at Loyola, Anna had the opportunity to do research in both Inorganic Chemistry and Microbiology where she discovered her passion for research and decided to further continue her education.

In addition to scientific studies Anna enjoys reading, horseback riding, traveling, gardening and spending time with family and friends.